NORTHWESTERN UNIVERSITY

Free-surface flows in dense colloidal suspensions

A DISSERTATION

SUBMITTED TO THE GRADUATE SCHOOL
IN PARTIAL FULFILLMENT OF THE REQUIREMENTS

for the degree

DOCTOR OF PHILOSOPHY

Physics

By

Phalguni S. Shah

EVANSTON, ILLINOIS

December 2022

ABSTRACT

Free-surface flows in dense colloidal suspensions

Phalguni S. Shah

In this dissertation, I summarize my findings of the dynamics of colloidal suspensions over a large range of volume fractions in two systems: drop impact and film rupture. The existence of a deformable surface in both these systems allows me to capture the consequences of non-Newtonian flow using high-speed imaging. The silica spheres and rods used in the experiments were synthesized in our lab, and characterized via SEM. Experiments were performed using known volumes of colloidal suspensions under controlled humidity.

For impacting drops, I show that the spreading behavior for a large range of volume fractions agrees surprisingly well with Newtonian models. In the dense limit, I characterize the transition between Newtonian-like spreading to complete solidification via localized and partial solidification states. I show that this behavior is a direct result of shear jamming, and the drop solidifies faster for higher applied shear rates. I characterize the resulting solid properties and its unjamming dynamics in details, and show that both depend on shear history. Additionally, for suspensions with rod-shaped particles, I observe dramatically different bouncing dynamics from sphere suspensions. I hypothesize that contact-line dynamics are heavily altered by the presence of rods-shaped particles.

Rupturing films behave as Newtonian viscous fluids for a wide range of volume fractions. However, for high volume fractions and thinner films, I report novel instabilities

during spontaneous rupture, that are reproducible under controlled humidity. I hypothesize that instabilities develop when the film thickness competes with particle lengthscale, as discrete effects start taking effect at individual particle level.

My systematic experiments span the transition from Newtonian-like to highly non-Newtonian behavior, bridging the gap between the existing understanding of Newtonian fluid dynamics and colloidal suspension dynamics. In the high volume fraction limit, my work uncovers interesting behaviors that will improve our understanding of particulate suspensions dynamics. This work connects to many pertinent questions in colloidal science, the most notable being the nature of the shear jamming transition and the dynamics of suspensions in a quasi two-dimensional geometry.

ACKNOWLEDGEMENTS

I am thankful to my PhD Advisor, Dr. Michelle Driscoll, for the opportunity to work with her during graduate school. Through the years, Michelle taught me so much about soft matter, experimental design, leadership, and life. Michelle has been wonderfully supportive of all of my aspirations within and beyond science. My growth as a researcher would not have been possible without all of her patience and encouragement. I am grateful for the mentorship of Dr. Srishti Arora, a former postdoc in the Driscoll lab. Srishti taught me everything I know about experiments, from setting up and maintaining a lab, to designing a research project. Srishti struck a magical balance of encouragement and constructive feedback that helped me grow as an experimenter. In addition to being a great teacher and colleague, I am fortunate to have Srishti as a friend.

I am thankful to our collaborators at the University of Minnesota, Dr. Xiang Cheng, Dr. Ting-Pi Sun, Anahita Mobaseri, and the entire Cheng lab. Working with them on drop impact has enriched my perspective of science and research. I am grateful to Dr. Jeff Richards and the Richards lab at Northwestern for the useful discussions, advice, and support. I am thankful to my thesis Committee members, Dr. Monica Olvera de la Cruz, Dr. Petia Vlahovska, and Dr. John Marko, for always being constructive and supportive with their feedback. Finally, I would like to thank my funding source, NSF DMR-2000417, for supporting my work on drop impact.

Working at the Driscoll lab has been a dream, thanks to my wonderful colleagues. It has been a privilege to have had great mentees in the Driscoll lab. Both Lily Boyd and Eleanor Ward taught me more than I could ever teach them, making me a much better teacher and scientist. I would like to thank Joey for his companionship during my early

days in the lab, and Ernest and Brendan for the useful discussions. I am grateful to Shih-Yuan for all his sympathy and encouragement while I was writing my dissertation. Thanks to Brian for the camaraderie and very fruitful collaboration on the drop impact project. Thanks to Kelsey for her authenticity and Ivan for sharing the love for free food. I am especially thankful to Carly for bringing so much art and joy to my life.

I am fortunate to have had wonderful mentors during my time at Northwestern. I am filled with gratitude for Dr. Gayle Ratliff, as she offered me so much useful advice and support in the time of need. Thanks to Professors Shane Larson and Deborah Brown for reminding me of the joys of teaching. I am grateful for the staff and students involved at the Searle Center for Advancing Teaching and Learning at Northwestern, for the much-needed community and a sense of belonging.

Graduate school was made easier by the many friendships I am lucky to have. I am grateful for the distance-defying bonds with Suchitra, Sujeet, and Siddhi. Thanks to Sajid, Felipe, and Sugat for the enriching conversations, Prashant and Praneel for the effortless friendships, Anamika and Sruthi for sharing food and laughter as roommates. I am forever thankful to Priyanka for all the love and support when I needed it the most. I am especially grateful for my Kathak teacher, Deepabali, for bringing me sanity during the pandemic via dance. Last of all, I am thankful for TGS commons and the lake shore trail — my happy places through the last six years.

I am privileged to have had a string of wonderful teachers throughout my life. I am grateful to Vrunda Joshi and Vikram Valimbe for nurturing my curiosity. Thanks to H. G. Deshpande, Salil Bedkihal, and Vishevesh Muzumdar for introducing me to the beauty of physics and mathematics. Thanks to Dr. Aniket Sule for exposing me to new possibilities and offering honest advice. Lastly, I am grateful to Professors Sudhir Jain,

Ameeya Bhagwat, Lionel Levine, and Deepak Dhar for their wisdom and patience during my early attempts at research.

I am grateful to my family for their unwavering support, especially my mother, who worked so hard to offer me every opportunity and exposure to succeed. I am indebted to my cousin Rajesh Vora and the entire Vora family for always being there to help. Special thanks to the Pawar, Shaikh, and Badapure families for being the village that raised me. I could not have made it far without their love and blessings. And lastly, I would like to thank Ben for his infinite patience, support, and companionship.

To my grandmother, for being an example of strength.

To my mother, for giving me the unending thirst to learn.

To my grandfather, for all the unconditional love.

To my father, for never holding me back.

TABLE OF CONTENTS

LIST OF FIGURES

CHAPTER 1
INTRODUCTION

When particles are suspended in a liquid phase, the resulting fluid is referred to as a 'particulate suspension'. The size of these particulate additives can range from a few nm to the order of magnitude of the system size. Particulate suspensions are broadly divided into two classes based on particle size. Brownian suspensions consist of particles that undergo thermal motion in a water-like fluid at room temperature. In other words, thermal effects dominate over particle inertia. The terms 'Brownian suspensions' and 'colloidal suspensions' are often used interchangeably. Non-Brownian suspensions (sometimes referred to as 'granular suspensions') consist of particles too large to undergo significant thermal motion. The particle size that divides these categories is ~ 10 μm. However, this transition is not well-defined, and suspension behavior depends on many factors, such as properties of the suspending fluid and flow velocities in the system. In all of the experiments discussed in this dissertation, we have used silica particles of size ~ 1 μm, therefore the focus of the work described here is on colloidal suspensions.

Many fluids familiar in everyday life are colloidal suspensions: the notable examples are milk (fat globules suspended in water), ink (dye particles suspended in water or oil), and blood (red blood cells suspended in water). The dynamics of colloidal suspensions are thus relevant to many processes, both natural and industrial. The concentration of a suspension is denoted by its volume fraction ϕ, the volume of particulate additives relative to the total suspension volume. In the low-ϕ limit ($\phi < 0.1$), colloidal suspensions act like simple Newtonian fluids (fluids whose viscosity is constant, irrespective of the

applied stress). However, as ϕ is increased, the unusual non-Newtonian properties of colloidal suspensions become more and more apparent. Understanding the flow of these suspensions is not only relevant to control industrial processes such as coating and spraying, but it is necessary for the design of novel materials such as body armors that harden upon impact.

In addition to altering the bulk properties of the fluid, colloidal additives add a length-scale to the system. A suspending medium such as water or oil is often modeled as a continuum in fluid dynamics. However, in the presence of colloidal particles, discrete effects are apparent on the scale of individual particles (~ 1 μm), which may manifest as local fluctuations in fluid behavior and novel instabilities. In my experiments, I observe both such behaviors.

Here, I discuss experimental results of the dynamics of silica colloidal suspensions in water via two systems: drop impact and film rupture. I scan a broad range of colloidal volume fractions: $0.00 \leq \phi \leq 0.50$ for drop impact, and $0.00 \leq \phi \leq 0.47$ for film rupture. Free and deformable surfaces present in both these systems enable us to directly observe the effects of non-Newtonian flow that are otherwise obscured in bulk rheology. I show that in the low- and moderate-ϕ limit, the suspensions dynamics can be modeled using the fluid bulk rheology. However for dense suspensions, localized heterogeneities are apparent in both systems in addition to changes in the bulk behavior. Our characterization of the data reveals connections with work in other adjacent areas such as dynamics of Newtonian fluids in similar system geometries, shear fronts in granular suspensions, and the nature of the shear jamming transition. This work provides insights complementary to bulk rheological data, and takes us a step closer to understanding colloidal suspension behavior under dynamic conditions.

For both systems considered here, I used silica colloidal particles suspended in water. In case of the film rupture system, a small amount of surfactant was present to aid film formation. I studied both colloidal drops and films using high-speed imaging, illuminated using white light. The silica colloidal particles used were synthesized and characterized in our lab. The experimental setups were built in the lab, tailored to our experimental requirements. I discuss the setup design in detail in the respective chapters. Silica particles were characterized via Scanning Electron Microscopy. Experimental data was analyzed using ImageJ and Python. All the plots were made using Python. I direct the reader to the respective chapters for more details on the experimental and analytical methods.

The rest of this dissertation is organized as follows: Chapter 2 outlines relevant concepts from colloidal rheology, and dimensionless parameters used for both Newtonian and colloidal fluids. In chapter 3, I outline findings from Newtonian and complex fluid drop impact that directly relate to my experiments. Chapter 4 discusses our findings on drop impact of colloidal suspensions made of spherical particles. Chapter 5 contains discussions of further considerations for colloidal drop impact: elastic modulus estimation in the absence of rebound, the dynamics of unjamming of the shear jammed drops, and experiments on the effect of particle anisotropy on impact dynamics. Chapter 6 outlines results on the rupture of colloidal soap films, with a comparison to viscous glycerol-water films. In addition to quantifying the rupture velocity, I discuss novel instabilities due to colloidal additives near the end of this chapter. Chapter 7 summarizes the insights developed here, and discusses pertinent open questions. Appendix A outlines the synthesis and characterization of silica spheres and rods, and Appendix B compares our spreading data for impacting colloidal drops with a number of existing Newtonian models.

CHAPTER 2
KEY CONCEPTS AND PARAMETERS

A suspension is 'colloidal' when thermal effects dominate over individual particle inertia at room temperature. As a result, one can observe colloidal particles suspended in a fluid exhibiting Brownian motion under a microscope. Typically, particles in the size range of 100 nm - 10 μm are considered colloidal, although this range may vary depending on system context and hence should only be taken as a rule of thumb. The suspensions used in our experiments are about 1 μm in size. In this regime, the surface energy of the suspending fluid also dominates over individual particle inertia. Therefore, the fluid behavior is largely governed by bulk suspensions properties instead of individual particle dynamics. The exception is when the particle size competes with a relevant system lengthscale, potentially giving rise to instabilities.

In this chapter, I describe relevant properties of colloidal suspensions, dimensionless parameters used in both Newtonian and non-Newtonian fluid systems, and important results for soap film dynamics. For a more thorough description, I refer the reader to the following sources: [1–4].

2.1 Non-Newtonian rheology of colloidal suspensions

In contrast to Newtonian fluids, the viscosity of colloidal suspensions can change as a function of the applied shear [1, 2]. 'Shear thinning' is defined as a decrease in fluid viscosity as applied shear is increased [$\phi = 0.28$ and $\phi = 0.34$ curves in Figure 2.1]. At higher shear rates, 'shear thickening' may be observed, where the fluid viscosity increases

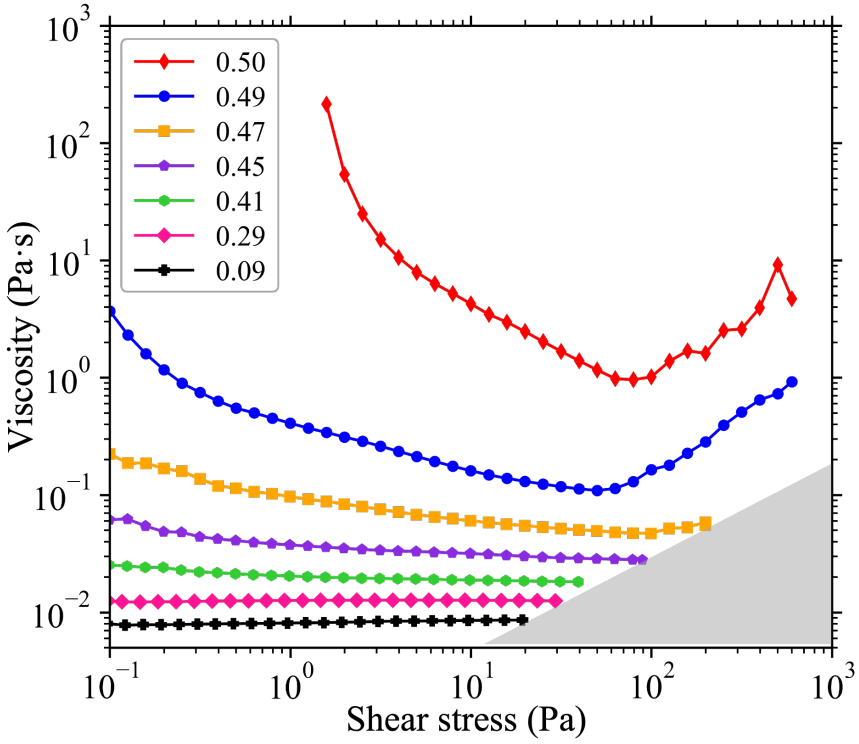

Figure 2.1: **Rheology of colloidal suspensions.** As the colloidal volume fraction, ϕ, is increased, the suspension transitions from Newtonian-like to shear-thinning, and then to shear-thickening behavior.

with shear [$\phi = 0.43$ and above in Figure 2.1]. The same fluid can exhibit both shear thinning and thickening behaviors depending on the applied stress; dense suspensions often exhibit shear thinning at low shear stresses and then begin to shear thicken as the stress is increased. The relationship between shear stress and shear rate can be described by a power law:

$$\tau_{shear} = k\dot{\gamma}^n, \tag{2.1}$$

so that $n = 1$ corresponds to Newtonian behavior, $n < 1$ to shear thinning, and $n > 1$ to shear thickening.

Particulate suspension flow behavior can be conveniently tuned by changing the vol-

ume fraction ϕ of particulate additives suspended in a fluid. At low ϕ they act as Newtonian fluids, but shear thinning and thickening are more apparent as ϕ is increased. Shear thickening is considered a precursor to 'shear jamming' [5], where flow is completely arrested due to external shear. Close to shear jamming, the power-law description [Equation 2.1] is no longer adequate, as the shear stress diverges.

2.2 Effective viscosity of colloidal suspensions

In addition to resulting in non-Newtonian flow behavior, the existence of particulate additives increases the overall viscosity of the bulk suspension. This 'effective viscosity' is a useful first approximation to model a suspension as a viscous Newtonian fluid. At the low-ϕ limit, the effective viscosity of the suspension can be computed using the Einstein relation:

$$\eta_{eff} = \eta_0(1 + 2.5\phi) \tag{2.2}$$

where η_0 is the viscosity of the surrounding fluid [1]. This approximation holds well only in the dilute limit, and does not account for the suspension viscosity diverging at finite ϕ due to jamming ($\phi_m = 0.64$ for hard spheres). The Krieger-Dougherty equation [6] accounts for the jamming volume fraction, and is commonly used to predict effective viscosity over a range of ϕ:

$$\eta_{eff} = \eta_0(1 - \frac{\phi}{\phi_m})^{[\eta]\phi_m} \tag{2.3}$$

where $[\eta]$ is the 'intrinsic viscosity'; $[\eta]$ =2.5 for spherical particles. This relation reduces to Equation 2.2 in the low-ϕ limit, and the viscosity diverges as $\phi \to \phi_m$, where the suspension jams. By computing the effective viscosity in this manner, one can define

modified counterparts to Newtonian dimensionless parameters.

2.3 Key dimensionless parameters

Below, some key dimensional parameters relevant to the work discussed here are defined, in forms they take for drop impact systems. Some of these parameters are defined for Newtonian fluids, and can be adapted for non-Newtonian fluids. Some others pertain specifically to non-Newtonian systems. For the dimensionless numbers defined here:

ρ is the density of the fluid,

η is the dynamic viscosity of the fluid,

d_0 is the drop diameter,

u_0 is the impact velocity,

and σ is the fluid surface tension.

- **Weber number** (We) is the ratio of inertial and surface stresses, $We = \frac{\rho u_0^2 d_0}{\sigma}$. Large We signifies that surface stresses are negligible compared to inertia, whereas surface stresses dominate at small We.

  For particulate suspensions, if the particles are large enough so that particle inertia dominates over bulk fluid behavior, the particle-based Weber number $We_p = \frac{\rho_p u_0^2 d_p}{\sigma}$ (where d_p is the particle diameter) is useful.

- **Reynolds number** (Re) is the ratio of inertial and viscous stresses. For drop impact systems, $Re = \frac{\rho u_0 d_0}{\eta}$. Viscosity dominates at small values of Re, while large Re implies that viscous stresses are negligible compared to inertia.

  In the case of non-Newtonian fluids, the **effective Reynolds number** is defined as $Re_{eff} = \frac{\rho u_0 d_0}{\eta_{eff}}$, η_{eff} being the effective fluid viscosity.

- **Stokes number** compares the viscous and inertial forces on a spherical particle suspended in a fluid, $St = \frac{\rho_p u_0 d_0}{\eta}$. The Stokes number provides the Reynolds number experienced by a single spherical particle in a fluid.

- The **Ohnesorge number** (Oh) compares the effect of viscous stresses with the combined effect of surface stresses and inertia, $Oh = \frac{\sqrt{We}}{Re}$. The Ohnesorge number is suitable for systems where inertial, viscous, and surface stresses may all be relevant — a common scenario for drop impact at a few meters per second.

- The **Capillary number** (Ca) is the ratio of viscous stresses to surface tension, $Ca = \frac{\eta u_0}{\sigma}$. Ca is large for viscosity-dominated conditions, and small when surface tension dominates.

- **Péclet number**, $Pe = \frac{3\pi\eta\dot{\gamma}d_0^3}{4k_BT}$, compares the rate of advection by the flow to the rate of diffusion by Brownian motion in a suspension. For high values of Pe, the flow dominates over thermal motion; this defines the high shear regime.

- **Froude number**: compares fluid inertia to gravitational effects, $Fr = \frac{u_0}{\sqrt{gd_0}}$. For typical drop impact experiments, the Froude number is large, and the effects of gravity can be ignored in drop impact systems.

2.4 Film rupture: important results

2.4.1 Culick's law

When a soap film of constant thickness h ruptures, a hole forms in the film and grows at a speed v. For a constant-thickness soap film, Culick [7] derived this rupture speed by momentum conservation, and showed that it is constant:

$$v = \sqrt{\frac{2\sigma}{\rho h}}, \tag{2.4}$$

where σ is the fluid surface tension, ρ is the fluid density and h is the film thickness. This 'Culick velocity' has been experimentally verified several times. As this velocity is equal to the speed of an elastic wave in two dimensions, we expect the outside of the film not to receive the information of the rupture event until the rupture reaches it. Therefore, we expect the outward-moving rim to collect more and more fluid as it rolls outward, while the rest of the film outside the rim stays intact.

Note that simple energy conservation — where the surface energy from both sides of the film, $E_{surface} = 2\pi r^2 \sigma$ is equated with the fluid inertia, $\frac{m(r)v^2}{2}$ — gives $v = \sqrt{\frac{4\sigma}{\rho h}}$, and overestimates the rupture velocity by a factor of $\sqrt{2}$. The momentum conservation derivation by Culick assumes an inviscid fluid, and we would not expect it to hold for high-viscosity fluids. However, more recent work [8] has shown that this relation holds asymptotically for viscous fluids, and viscosity only introduces a larger and larger transient in the initial stage of rupture. In practice, this transient is quite brief: for example, for a fluid with 100 cP viscosity (100 times that of water) and 70 mN/m surface tension (comparable to water), the transient is roughly 10 μs.

2.4.2 Application of LLD theory: Frankel's law

When a fiber is slowly (so that inertial effects are negligible) pulled out of a bath of fluid, a thin film clings to it due to viscous drag. The steady-state thickness of the film clinging to the fiber is estimated by equating the pressure due to viscous effects with the capillary pressure across the meniscus that forms between the pool and the film clinging to the fiber [4]:

$$\frac{\eta u_0}{h^2} \sim \frac{\sigma}{lb}, \tag{2.5}$$

where η is the dynamic viscosity, u_0 is the velocity of pulling, h is the film thickness, σ is the fluid surface tension, b is the diameter of the fiber, and l is the characteristic length over which pulling affects the film shape. This length can be estimated by using the smooth boundary condition between the static and dynamic menisci, $l \sim \sqrt{bh}$. This allows us to derive the relation between the film thickness h and the capillary number, $Ca = \frac{\eta u_0}{\sigma}$:

$$h \sim bCa^{2/3}. \tag{2.6}$$

As mentioned before, this law holds when viscosity dominates over inertia. More quantitatively, this law is expected to hold for $Ca^{1/3} \ll 1$, or $Ca \ll 10^{-3}$. However, experimental data has reported deviations for values as low as $Ca \sim 10^{-4}$ [9].

Here, I have summarized key concepts and dimensionless numbers used in the rest of the dissertation. I have also outlined key results from the literature that are directly connected to my work. In the following chapters, I will discuss when colloidal suspensions follow and deviate from these behaviors.

CHAPTER 3
DROP IMPACT: RELEVANT RESULTS FROM THE LITERATURE

In this chapter, I outline results from the literature relevant to the drop impact experiments outlined in this dissertation. In section 3.1, I discuss results from Newtonian fluid impact that directly relate to our system, and in section 3.2 I summarize studies on impacting drops of particulate suspensions. I note that this is not a comprehensive overview, and I only highlight results that directly relate to my work.

3.1 Relevant advances in Newtonian drop impact

Despite the complexities of the drop impact process, a comprehensive understanding of impacting Newtonian drops has been developed. Though there are key differences between the flow properties of Newtonian and complex fluids, they share system details and experimental methods. Moreover, in certain regimes, the physics of impacting complex fluids can be understood using Newtonian models. Therefore, Newtonian studies provide the foundation for their complex fluid counterparts. In this section, we summarize relevant results of Newtonian drop impact. We emphasize that this section is not intended to be a comprehensive review of Newtonian drop impact. Instead, we aim to highlight aspects of Newtonian impact that are most relevant to the impact dynamics of complex fluids. For a more complete discussion of Newtonian drop impact, we refer the interested reader to the following reviews on the subject: [10, 11].

When a fluid drop impacts a surface, the drop radially expands on the timescale of a few milliseconds. Fluid inertia is converted into surface energy, while being opposed by

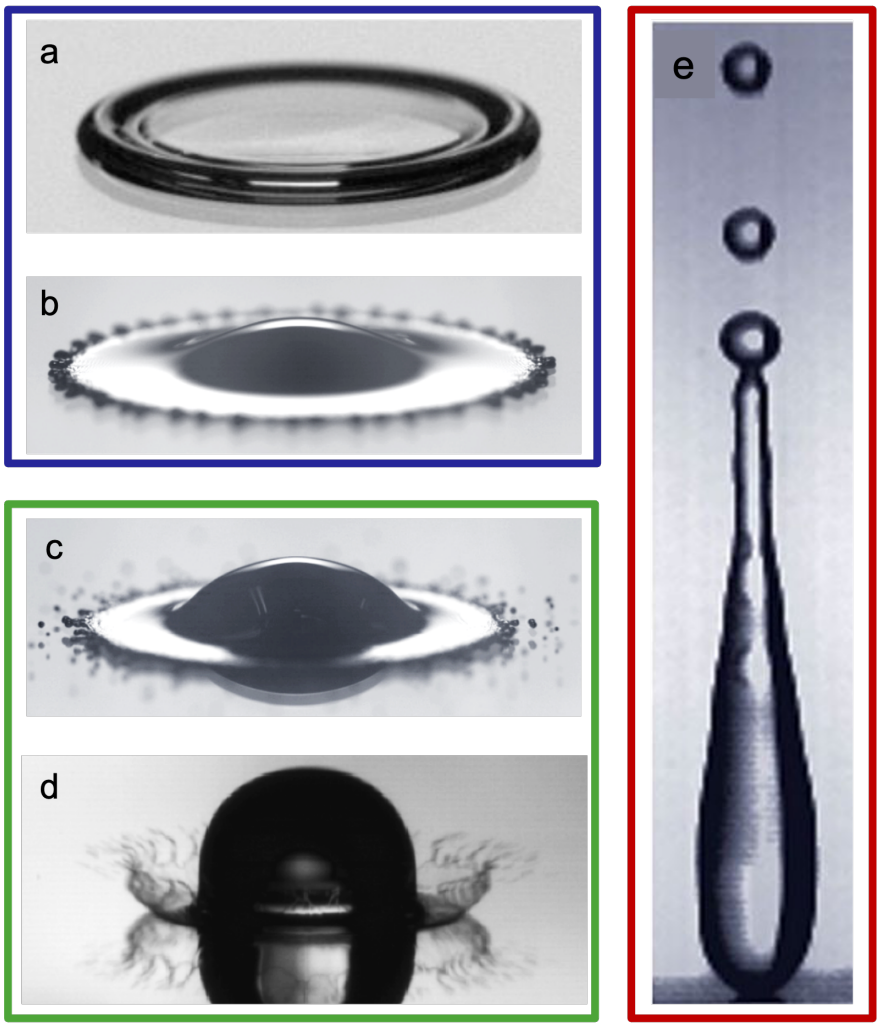

Figure 3.1: **Various outcomes after a Newtonian drop impacts a solid substrate.** **a** A drop of water spreading after impact on a smooth hydrophilic substrate. **b** A drop of mercury developing instabilities in its rim during spreading, **c** A drop of mercury undergoing prompt splash, and **d** A drop of silicone oil undergoing corona splash. Panels b-d adapted from Josserand and Thorodssen [12]. **e** A drop of water rebounding after impact on a hydrophobic substrate. Adapted from Quere [13].

viscous stresses, fluid-solid surface interactions, and ambient gas effects. As a result, the fluid spreads radially onto the substrate [Figure 3.1a]. In some impact regimes, the rim of the spreading drop may become unstable [Figure 3.1b], which may lead to ejection of

secondary droplets, termed as 'splashing'[Figure 3.1c and d]. After the spreading phase, the fluid may recede. On hydrophobic surfaces, drops impacting at large impact velocities may also bounce back [Figure 3.1e]. A significant body of work has been done to understand spreading [14, 15], receding [16], bouncing [13, 17], and the transition from spreading to splashing [10, 11, 18]. Below, we summarize key findings from those Newtonian drop impact studies that directly connect to the existing body of work for impacting complex fluid drops.

Immediately after impact, the fluid drop undergoes inertial spreading. The maximum spreading diameter after impact is governed by the balance between drop inertia, surface tension, and viscous dissipation. Energy conservation arguments in the low-viscosity, high-inertia regime (large Re, We) predict the maximum drop spread to scale as $We^{\frac{1}{2}}$. Scheller et al. [19] reported a $ReWe^{1/2}$ empirical scaling for spreading viscous fluids:

$$\beta = 0.61(ReWe^{1/2})^{0.166}. \tag{3.1}$$

However, in the high-viscosity, low-inertia regime (small Re), the maximum spread has been observed to follow the scaling of $Re^{\frac{1}{5}}$ [12]. It has thus been proposed that a broad crossover regime must exist between these two extremes. More recently, scaling laws based on models that consider the balance between inertial, viscous, and capillary effects have been reported. Laan et al.[14] considered the relation

$$\beta = Re^{1/5} f(WeRe^{-2/5}) \tag{3.2}$$

and used the first-order Padé approximation to fit experimental data:

$$\frac{\beta}{Re^{1/5}} = \frac{(WeRe^{-2/5})^{1/2}}{A + (WeRe^{-2/5})^{1/2}} \tag{3.3}$$

This equation interpolates between the viscous regime (linear in $WeRe^{-2/5}$) and the inertial regime (constant with respect to in $WeRe^{-2/5}$), and consists of a fitting parameter. As discussed in the review by Josserand and Thorodssen [12], the Scheller et al. scaling can be rewritten, so that it has the same functional form as Equation C.3:

$$\beta = (ReWe^{1/2})^{1/6} = Re^{1/5}(WeRe^{-2/5})^{1/12}. \tag{3.4}$$

Here $f(WeRe^{-2/5})$ takes the form of a single power law with an exponent of 1/12, instead of interpolating between two regimes via a Padé approximant. Thus, despite being an empirical fit, the Scheller et al. model is consistent with the functional dependence of Equation C.3 reported more recently. Josserand and Thoroddsen [12] have compared a number of scaling models for drop spreading in detail, and showed that all of these models describe experimental data well, thus it is hard to differentiate between them.

Lee et al. [20] have recently reported a data scaling with a substrate wettability correction, where they calculate the spreading at zero impact velocity, $\beta_{v\to 0}$ using another Padé approximant with four fitting parameters. Corrected this way, they plot $(\sqrt{\beta^2 - \beta_{v\to 0}^2})/Re^{1/5}$ against We, instead of the parameter $WeRe^{-2/5}$, and show a good collapse for several fluids. Correcting for surface wettability in this way is crucial when comparing the impact of fluids with widely varying surface tensions, as it might affect the wetting properties significantly. We do not correct for substrate wettability in our analysis, as all of our data involves water as a suspending fluid, and the surface tension of the suspensions does not

vary with ϕ.

After the spreading phase, the impacted drop may retract. Bartolo et al. [16] observed that when impacted on hydrophobic surfaces at high We, the drop receding velocity was independent of impact velocity. This suggests that while inertia governs the spreading phase, it has a negligible effect on the dynamics of the receding phase. The authors additionally observed that, consistent with simple hydrodynamic arguments, the receding rate depends on viscosity via the Ohnesorge number Oh. Subsequent numerical and experimental work has accounted for substrate wettability via the retracting dynamic contact angle [21, 22]. Experiments on small targets are effective for decoupling substrate interaction from fluid properties. Small target experiments have studied the spreading [23], thickness evolution [24], and disintegration [25] of expanding fluid sheets.

In addition to spreading and receding, liquid drops impacting on hydrophobic surfaces may bounce off the impact surface. For high Re and We impacts, drops bounce almost elastically, and have been successfully modeled as a simple spring-mass systems [26]. Recently, this model was extended to account for drop viscosity using a damped spring-mass equation [27]; this model also predicted an increase in the contact time with the substrate. Controlling bouncing and contact time is important in the development of water-repellent surfaces, and the use of microstructures has been proposed for such applications [17]. For a more detailed discussion of drop impact on hydrophobic surfaces, we refer the reader to this recent review: [28].

At the end of the spreading phase, a drop may splash. The transition to splashing was originally proposed to be governed by the parameter $K = We(Re)^{\frac{1}{2}}$ [29, 30]. This characterization of splashing was limited, as it incorporated only the fluid and impact properties. More recent studies have demonstrated that the quantitative value of the

splashing threshold additionally depends both on the details of the substrate [31] and surprisingly, the surrounding gas [32]. The dynamic contact angle during impact is set by fluid-substrate interactions, and differs during the spreading and receding phases [33]. The role of the contact angle in splashing is an active area of investigation [34, 35]. Additionally, it remains a challenge to measure this microscopic quantity angle experimentally. Quetzeri-Santiago et al. [35] proposed that the advancing dynamic contact angle (as opposed to the static contact angle) is relevant for predicting the splashing threshold, potentially extending our understanding of splashing to hydrophobic surfaces. The observation by Xu et al. [32] that lowering the ambient pressure could completely suppress splashing has inspired numerous works [18, 35–39]. At early stages of contact, an air layer has been observed under the spreading fluid [40–44], and this has been linked to the pressure-dependence of the splashing threshold. Recent work has focused on incorporating the effects of gas viscosity, density, and mean free path on splashing [18, 36, 39]. The work so far has neglected gas compressibility; incorporating this effect in future studies would be valuable, albeit challenging.

Although most drop impact studies have focused on normal impact and hard substrates, real-life impacts often happen at an angle, or on compliant surfaces. The best example of this is the spraying of pesticides onto leaves, a process where both of these modifications come into play. Studies on splashing onto oblique and translating surfaces [14, 45–47] have observed asymmetric splash. However, models for maximum spreading diameter are applicable to inclined systems, when the normal component of impact velocity and short axis of spreading [14] are used. Drop impact work on compliant substrates [48, 49] has reported suppressed splashing, and linked it to the increased energy dissipation on a softer impact substrate [49]. Further studies on these lines would be relevant to a

variety of applications, as tuning the substrate compliance is a potentially facile way to control splashing in many processes.

Despite the properties of complex fluids being significantly different from Newtonian fluids, many parallels can be drawn due to identical system details such as the free-surface geometry and experimental techniques used. Broadly defined behaviors such as spreading, receding, splashing, and bouncing have counterparts for impacting complex fluid drops, although the quantitative trends and governing parameters vary. Throughout the following sections, we connect disparate observations of impacting complex fluid drops to the existing foundation of Newtonian studies. We highlight phenomena that need further exploration in order to build a more unified picture of the physics of non-Newtonian drop impact.

3.2 Past work on the impact of particulate suspensions

Particulate suspension drops show a rich variety of behaviors when impacted onto a substrate [Figure 3.2]. Here, I discuss relevant results from the impact of particulate suspensions. Traditionally, particulate suspensions are divided into two broad classes based on particle size: Brownian and non-Brownian suspensions. The particle size that divides these categories is ~ 10 μm. However, the transition between these two regimes is not well-defined, and suspension behavior can depend on many other factors such as the properties of the suspending fluid, relative density of particles in the fluid, and flow velocities in the system. Moreover, drop impact processes happen at high Péclet numbers, and the contribution of thermal diffusion to impact dynamics is negligible. However, particle inertia still plays an important role in the dynamics of impact, when compared to bulk fluid properties. For large particle additives, particle inertia can dominate over

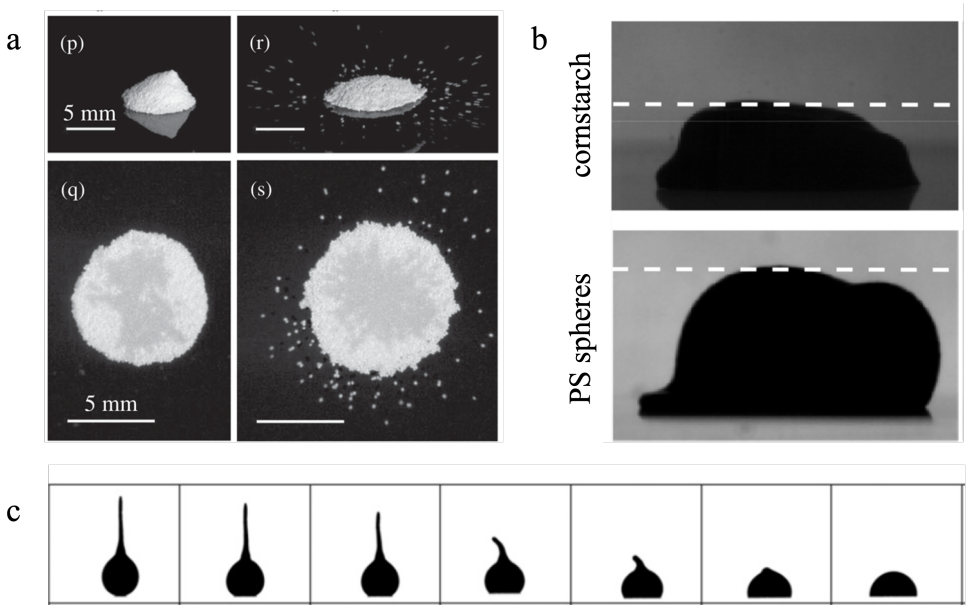

Figure 3.2: **Various outcomes after a complex fluid drop impacts a solid substrate. a** A non-Brownian suspension drop splashed by ejecting individual particles upon impact. Adapted from Peters et al. [50]. **b** Both Polystyrene and cornstarch suspension drops do not spread after impact. Adapted from Boyer et al. [51]. **c** A dense colloidal drop solidifies when impacted on a substrate. Adapted from Bertola et al. [52]

the bulk fluid rheology, and the impact dynamics are best evaluated using particle-based parameters. Thus, for the purposes of this dissertation, I classify drop impact studies into two regimes: where impact dynamics are governed by the bulk fluid rheology, and where particle inertia governs certain impact outcomes. We emphasize that our discussion here is not classified strictly on the lines on particle size, but observed fluid behavior in the context of all the system parameters. Section 3.2.1 discusses studies where impact behavior is connected to the fluid rheology, whereas Section 3.2.2 discusses studies where the inertia of individual particles may govern impact outcomes.

3.2.1 Bulk rheology-dominated regime

A drop impacting on a solid substrate experiences large shear rates that vary spatially throughout the drop as well as over time. This spatiotemporal variation is especially relevant to the problem of impacting particulate suspensions, as their rheological properties change dramatically as a function of shear rate, $\dot{\gamma}$, in addition to the particle volume fraction, ϕ. Below, we highlight impact outcomes of particulate suspensions in the regime that is governed by bulk rheology, and draw connections to insights from rheology data.

Particulate suspensions exhibit both shear thinning and shear thickening behaviors in certain ranges of ϕ and applied shear [1, 2]. In the dilute limit ($\phi \lesssim 0.1$), the suspension behaves practically like a Newtonian fluid, and particulate additives only increase the effective suspension viscosity. As ϕ is further increased, the suspension exhibits shear thinning, and then shear thickens at even higher ϕ. The same fluid can exhibit both shear thinning and thickening behaviors depending on the applied stress; dense suspensions often exhibit shear thinning at low shear stresses and then begin to shear thicken as the shear stress is increased.

Particulate suspensions are shear thinning over a wide range of ϕ. Although we expect shear thinning to have a significant effect on post-impact spreading, the drop diameter d during spreading has been shown to grow in a manner identical to the spreading of Newtonian drops [53]. Multiple studies over a range of particle sizes [53–63] have reported that the spreading of suspension drops can be effectively quantified using spreading models for Newtonian fluids [14, 64]. To model the data in this way, the effective viscosity of the suspension was used. Theoretically, the bulk effective viscosity is an extension of the Einstein viscosity beyond the linear term [6]. In practice, however, the experimental value inferred from the rheological data is often used. As effective viscosity grows with

ϕ, the maximum spreading after impact, d_{max}, decreases. Even for particles as large as 145 µm, the spreading of particulate suspension drops has been directly compared to the spreading of Newtonian drops with a similar viscosity [57]. Thus, the bulk effective viscosity is a useful approximation to quantify drop spread for particulate suspensions well beyond the Brownian limit.

Although substrate wettability has a relatively small effect on post-impact spreading (especially in the high-We limit), the receding phase depends strongly on substrate properties as well as the viscosity of the suspending liquid. Several works have shown that the dynamics of the receding phase determine the final distribution of particles deposited on the substrate. Nicolas et al. [59] found that long after impact, the particle distribution on the substrate varied drastically with the fluid Re. While particles were concentrated in an annular region for impacts at high Re, they were uniformly distributed for low-Re impacts. Grishaev et al. [63] have additionally reported that while the particles formed monolayers on hydrophilic surfaces, three-dimensional crown-like structures formed after impact on hydrophobic substrates. Thus, substrate wettability has a direct effect on the post-impact particle distribution, highly relevant in coating and printing applications.

As with Newtonian [23–25] impacts discussed before, small target-based experiments minimize substrate effects in the post-impact behavior of particulate drops. Experiments on small targets by Raux et al. [61] showed that d_{max} and t_{max} after impact were independent of particle size (varied from 40 μm to 140 μm). However, the receding phase was slowed down by the presence of larger particles. Larger particles have also been observed to make the film unstable during retraction, leading to rupture and decrease of film lifetime. Thus, particulate additives have a destabilizing effect on the fluid film formed after

impact on small targets, in stark contrast with the stabilizing effect of polymeric additives on the film [65].

In addition to spreading, controlling the splashing of particulate fluids is key in many processes. The impact dynamics of blood, a well-known shear thinning fluid, are of special interest due to its relevance in forensic analyses. De Goede et al. [37] observed that substrate wettability had little effect on the splashing threshold of blood. Once again, this is consistent with observations of Newtonian splashing on substrates of varying wettability [18]. For suspensions comprised of larger particles where inertia plays a significant role, the splashing onset is fundamentally different and is studied via particle-based parameters, as discussed in section 3.2.2.

Particulate suspensions exhibit shear thickening at high ϕ and large applied shear. Shear thickening fluids typically show an increasing viscosity with increasing shear, often transitioning to shear jamming (solid-like behavior) at the highest stresses. Drop impact studies in the shear thickening regime result in exotic behaviors due to the large and instantaneous shear rates ($\mathcal{O}(10^3)s^{-1}$ and greater). Despite having great potential to expand our knowledge of the high stress response of these materials, drop impact studies of shear thickening fluids have been few and far between, likely due to the experimental challenges inherent to working with dense suspensions.

On impact, dense suspension drops have been observed to undergo solidification [52] [Figure 3.2 c]. Boyer et al. [60] observed that shear thickening drops (cornstarch and polystyrene suspensions, $d \sim 5$ to $20\mu m$, volume fraction $\phi > 0.33$) showed a maximum deformation that was independent of the impact velocity, and the drops stayed immobile long after impact [Fig. 3.2b]. In my recent work [56], I observed partial solidification states in impacting dense suspension drops, where drops solidify from the bottom but

the top part remains liquid. I discuss my findings in detail in chapter 4. While shear jamming observed on hydrophilic substrates was transient and the drops 'unjammed' into the fluid state over a few seconds [56], concentrated colloidal drops ($\phi \sim 0.6$) impacted over hydrophobic PTFE surfaces are reported to stay jammed for days [66]. The interaction between the drop and the surface thus seems to play a key role in the timescale of unjamming.

Shear fronts traveling upward along the drop surface at speeds faster than u_0 were observed in my experiments [56]. Observations of large frequency changes due to polystyrene drops impacting on microresonators [67] have also been attributed to shear-induced structures inside the drop. In a different but related system, shear fronts occur when larger reservoirs of complex fluids are impacted with an impeller [68–72]. Microscopic observations of propagating shear have unveiled insights of front propagation in these systems. Similar microscopic characterisation of shear fronts in impacting drops, although challenging, would play a great role in developing the broader physics of the shear jamming transition.

In future works on suspension drop impact, extensive use of techniques to measure local stresses in an impacting drop is key. Studies of Newtonian fluids have established the velocity and pressure fields within an impacting drop for a large range of viscosities [73, 74]. Although these works are not directly applicable to highly non-Newtonian fluids, they should serve as a foundation to extend our understanding of flows inside an impacting suspensions drop. Numerical work on the spatial variation of shear stresses during all phases of suspension drop impact could provide a necessary phenomenological basis for understanding the flow of these liquids at high stresses.

Current studies of shear thickening fluids have clearly identified novel behaviors, such

as partial/complete solidification upon impact. To use drop impact as platform to study stress-induced jamming, this work should be expanded, with special attention paid to suspensions in both the CST and DST limits. Overall shear stresses in impacting drops can be estimated and measured, but localized information is quite challenging to obtain experimentally. To understand the physics of localized shear jamming, systematic measurements of shear stresses in the impacted drop are crucial. Promising avenues for obtaining these measurements include localized measurements of boundary stresses (akin to traction force microscopy measurements [75–77]). Shear fronts in particulate systems under confinement have been characterised [68–72], numerical studies exploring how similar fronts propagate in free-surface systems would be informative in the future.

Another avenue ripe for exploration is the role of particle shape. It is well-known from bulk rheological measurements that the critical volume fraction for jamming varies with particle shape. In particular, elongated (large aspect ratio) particles can exhibit jamming behavior at dramatically lower volume fractions than their spherical counterparts [78, 79]. However, the role of particle shape on shear jamming in drop impact systems has thus far been unexplored. I discuss my preliminary results on the effect of particle anisotropy on impact dynamics in section 5.3. These studies have the potential to probe the role of shape asymmetry in the high-stress behavior of suspensions, as well as relevance to industrial processes, where the component particles in slurries and suspensions are often far from spherical.

In summary, the impact of low- and moderate-ϕ drops can be understood using the bulk effective viscosity of the suspension for a wide range of particle sizes. However, for high-ϕ drops containing larger particles, individual particle inertia plays a significant role in the impact dynamics and the liquid merely acts as an agent that binds the

particles into a drop. Particle-based parameters have shown success in characterizing the spreading dynamics in this regime. Furthermore, these particle-based parameters are also effective for predicting the splashing threshold for granular suspensions, as described in the next section.

3.2.2 Particle inertia-dominated regime

Close to the critical volume fraction ϕ_m for jamming, impacting dense suspension drops have been observed to deviate from their bulk behavior, and a clear deviation from the effective viscosity framework is reported [57]. Lubbers et al. [80] studied the high-inertia impact of dense suspensions ($d = 250$ μm, $\phi > 0.60$); upon impact these drops created a particle monolayer, which was found to grow at a different rate than the spread of a Newtonian liquid drop on a surface. This high-ϕ, inertia-dominated phenomenon was explained in terms of a particle-based Weber number We_p and liquid Stokes number St ($We_p \gg 1$, $St \gg 1$ in this study). The authors proposed a particle-based chain model of spreading; this emphasizes the quite different physics of impacting drops with larger particulate additives. In this parameter regime, the post impact behavior is best characterized in terms of particle inertia as opposed to the bulk fluid flow.

Similar to Newtonian drops, particulate suspensions can splash under certain impact conditions. However, the nature of this splashing is fundamentally different than that of Newtonian fluids, especially for large particle additives. Peters et al. [81] studied the splashing threshold of dense non-Brownian suspensions of particle sizes greater than 80 μm, in the range $0.59 < \phi < 0.65$. 'Splashing' in this case comprised of individual particles being ejected from the edge of the drop. They found that this splashing threshold was best characterized in terms of the particle-based Weber number $We_p = \frac{\rho_p r_p u_0^2}{\sigma}$, rather than the

typical fluid We. This suggests that splashing occurs when an individual particle overcomes the surface energy of the surrounding liquid, and that larger and denser particles are more likely to escape at lower drop velocities. As opposed to Newtonian splashing, they observed that the onset of splashing for these suspensions (at $We_p \geq 14$) was independent of the substrate wettability and roughness. This We_p dependence has been verified in subsequent studies [62, 82]. Consequently, Schaarsberg et al. [82] experimentally investigated the effect of suspending liquid viscosity on dense ($\phi = 0.59$) suspension splashing, showing that the phase space defined by We_p and St, the Stokes number, is cleanly divided into splashing and non-splashing regimes. Thus, the understanding has emerged that particle inertia, along with viscous interactions between particles and the suspending liquid, control the splashing threshold of dense non-Brownian suspensions, as opposed to the bulk rheological properties that govern the spreading dynamics.

Marston et al. [53] tracked individual particles ejected after splashing (grain size ~ 350 μm) and found that the maximum particle velocity was typically twice that of the drop velocity, a much smaller ratio as compared to droplets ejected during Newtonian splashing. Their image analysis suggests that the drop compressed after impact, and particles were ejected when this compression pushed ϕ closer to the jamming threshold. For a more comprehensive understanding of this correlation between splashing and the jamming volume fraction ϕ_m, the elastic energy of the jammed network needs to be taken into account, as long-range correlations among the particle structure are likely to be significant near ϕ_m.

Understanding the splashing of particulate suspensions is relevant to numerous industrial and natural processes, where suspensions involved are rarely monodisperse. For bimodal suspensions (suspensions comprised of two particle sizes), Peters et al. [81]

found that smaller particles were more likely to be ejected than larger particles. This is seemingly contradictory to the We_p-based predictions discussed above. However, due to momentum conservation, particle-particle collisions during impact cause smaller particles to gain higher velocities, and thus they get ejected earlier. This argument can be potentially extended to polydisperse suspensions, where we would expect smaller particles to eject with more ease during splashing.

Thus, the splashing of dense non-Brownian suspensions is governed by individual particle inertia, while the splashing of Brownian fluids is governed by bulk flow, similar to Newtonian fluids. Recently, Grishaev et al. [83] studied the splashing of suspensions made up of 10 μm spheres, and found that the splashing threshold did not agree with either the bulk fluid models for Newtonian fluids [59] or particle-based models [62, 81]. The droplets ejected after splashing were an order of magnitude larger than the suspended particles, as opposed to individual particles ejecting for suspensions whose splashing was governed by particle-based parameters [62, 81]. This indicates that there is a broad crossover regime between the two extremes of splashing — that governed by bulk flow and that by individual particle inertia. Detecting individual particles with a high-speed camera is more challenging for smaller particles. More experimental studies that integrate microscopy with high-speed imaging might be fruitful in this respect. A large amount of systematic data ranging over particle Weber numbers is necessary to develop scaling laws over the whole range of particle sizes.

Particle shape not only affects the critical volume fraction ϕ_m [78, 79], but the realignment of particles due to shear can also affect bulk flow properties of the suspension. Additionally, in the dense suspension limit where the bulk viscosity framework is inadequate, experiments with index-matched fluids with tracer particles would be worthwhile

to visualize the flow within the drop during impact. This would allow one to obtain highly spatially resolved data for ϕ, and enable an exploration of how drops behave upon impact.

CHAPTER 4
IMPACT DYNAMICS OF SPHERICAL SILICA COLLOIDS

Note: The contents of this chapter are largely identical to my publication in Communications Physics: https://doi.org/10.1038/s42005-022-00998-w

4.1 Introduction

Complex fluids, such as particulate suspensions[3, 84] and polymer solutions[85], exhibit a variety of exotic flow behaviors, for instance shear thickening and solidification via jamming. These behaviors are particularly relevant to development of smart materials, such as body armours[86] and soft robots[87]. Rheometry is traditionally used to characterise complex fluids. However, this technique typically provides measurements averaged over the bulk of the fluid and obscures the information on local variations in flow. The free-surface geometry in drop impact systems offers a unique lens to probe these flow properties, as it provides data on manifestations of non-Newtonian flow with high spatial and temporal resolution. Here, we use high-speed imaging to study the drop impact of colloidal suspensions over a large range of volume fractions and impact velocities, thus sampling impact behavior from liquid-like spreading to solid-like jamming. Combined with input from rheological data, our measurements offer a more holistic picture of complex fluid flow, especially under dynamic conditions.

An extensive understanding has been developed for the dynamics of a Newtonian fluid drop impacting a dry solid substrate[12, 14, 20, 73, 74, 88]. However, the vastly different flow properties of complex fluids substantially modify impact dynamics. Past

studies have explored the spreading and splashing of a variety of polymeric fluids[89, 90] and particulate suspensions[50–52, 57, 91, 92]; however each has largely focused on a relatively narrow slice of the vast parameter space. The role of particulate additives in controlling the splashing transition has been explored[50, 91], as well as the spreading and jamming of dense suspension drops[51, 52, 57, 92]. In particular, experiments on impacting shear thickening fluids have reported solid-like states after impact[51, 52, 57]. Colloidal suspensions offer a convenient control parameter — volume fraction — to scan suspension behaviors ranging from Newtonian-like to shear thickening. Here, we report a systematic study of colloidal suspension impact spanning a range of volume fractions ($0.09 \leq \phi \leq 0.50$) and impact velocities ($0.7\ m/s \leq u_0 \leq 4.0\ m/s$). Our exploration of this wide parameter space allows us to capture not only spreading and bulk solidification, but also the transition between these drastically different flow regimes.

For our experiments, we synthesize charge-stabilized silica spheres (diameter $2a$ = 830 ± 20 nm, Fig. 4.1a) using the Stöber process[93, 94] and suspend them in water. The sedimentation time is the time a sphere takes to sediment freely over its radius a[95], calculated as:

$$t_s = \frac{9\eta}{2\Delta\rho g a}, \tag{4.1}$$

where η is the dynamic viscosity of the suspending fluid (water in this case), $\Delta\rho$ is the density difference ($\rho_{silica} - \rho_{water}$ = 1 g/cm^3), g = 9.8 m/s^2, and a = 415 nm, the radius of the particle. Calculated in this manner, t_s = 1.1 s. Therefore, the characteristic time for a particle to sediment over the lengthscale of the drop (d_0 = 3 mm) is t_s^{drop} = 4000 seconds, or over an hour. Thus, the time for our silica sphere to sediment over the size of the droplet is much longer than the time of the experiment. This calculation for dilute suspensions has been shown to be modified by a factor smaller than 1, up to ϕ = 0.30[96].

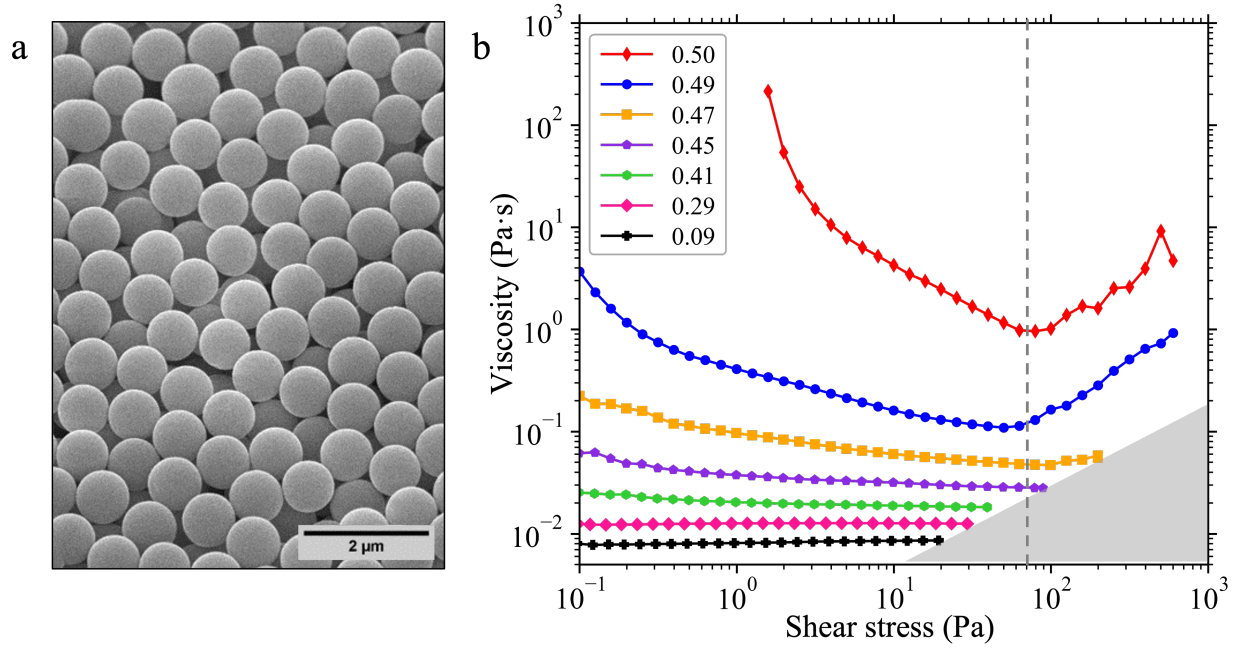

Figure 4.1: **Rheology of the colloidal suspensions.** **a** SEM image of the colloidal silica spheres used in our drop impact experiments; the sphere diameter is 830 ± 20 nm. **b** Bulk rheological flow curves: the colloidal suspension exhibits viscous flow, shear thinning, and shear thickening as ϕ is increased. The grey triangle in the bottom right indicates the rate limit of the rheometer.

Therefore, for our system, this calculation serves as an upper-bound estimate. To further decrease sedimentation effects, all samples are re-suspended immediately before every trial using a vortex mixer. Spherical drops of diameter $d_0 = 3.0 \pm 0.1$ mm are formed by drawing a known volume of fluid (15 μL) into a micropipette. We set the impact velocity by changing the height from which the drops are released, and record the drops impacting on a dry, hydrophilic glass substrate using a high-speed camera. We note that the contact angle of gently deposited suspensions on the glass substrate is practically constant with increasing ϕ, around 4^o (for more details, see Supplementary Information). All experiments are performed in a humidity chamber, which additionally mitigates air

currents (see Methods for details). Data is analysed via ImageJ, and plotted using python. Error bars reported are one standard deviation over at least 5 trials (one standard deviation corresponds to a 68% confidence interval).

Shear thickening — an increase in viscosity with increasing shear — is one of the most counterintuitive phenomena exhibited by dense suspensions[3, 84]. The Péclet number, $Pe = \frac{\text{shear rate}}{\text{rate of diffusion}}$, is a dimensionless number used to quantify high shear rates, and we expect the onset of shear thickening at $Pe \gg 1$. The transition to shear thickening occurs when a suspension with relatively high ϕ is subjected to a shear higher than a critical value[2, 84, 98, 99]. We note that for our experimental parameters, $Pe > 10^2$, and thus we expect shear thickening after impact in the high-ϕ limit. Many rheological studies have focused on elucidating the mechanism of shear thickening, and both lubrication hydrodynamics and particle interactions have been shown to play a role. Shear thickening has been proposed as precursor to shear jamming, and the nature of this transition is an active field of study. For a more detailed discussion, we refer the reader to the following reviews[2, 3, 98, 99].

To connect impact behaviors with rheological properties, a mapping between impact velocity and rheological parameters is necessary. Precisely quantifying shear rates in drop impact systems is challenging due to the nonuniformity of shear in both space and time. However, a simple dimensional argument can be used to estimate the shear rate at impact. At the instant of impact, the bottom point of the drop comes to rest, while the apex continues to fall at the impact velocity u_0, as the shear caused by impact has not had time to propagate across the drop. Dividing this difference in speeds, u_0, by the drop size d_0 thus provides an estimate of the maximum shear rate at the moment of impact: $\dot{\gamma}_{impact} = u_0/d_0$. With the drop size of 3 mm, we could access shear rates in the range 233

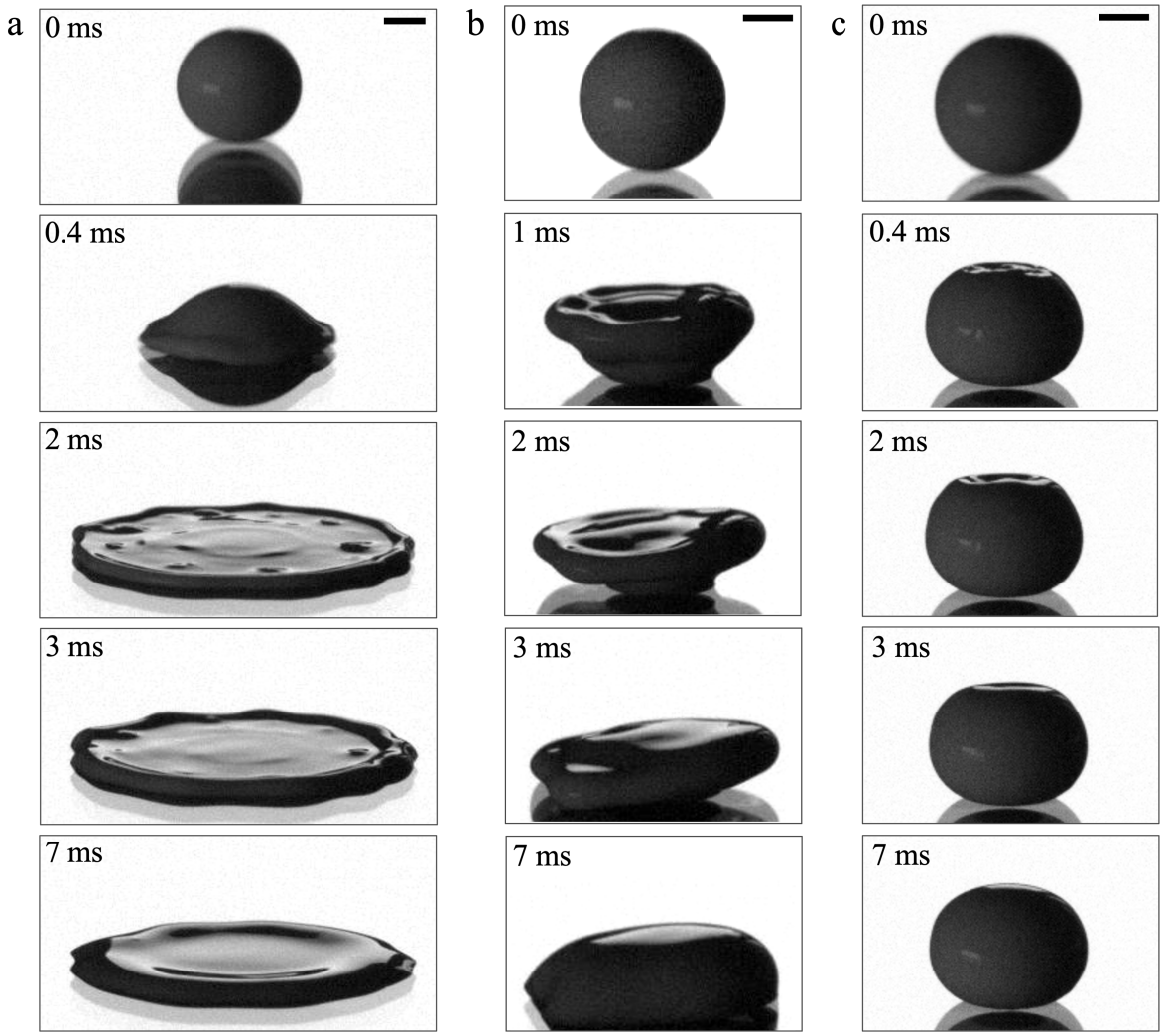

Figure 4.2: **Exotic impact behaviors of colloidal suspension drops.** **a** Timeseries of a $\phi = 0.47$ colloidal drop expanding after impacting at $u_0 = 3.0$ m/s [SI video 1 [97]]. The spreading drop shows transient pockets of localized solidification, indicating the onset of shear thickening. **b** Timeseries of a $\phi = 0.49$ colloidal drop impacting at $u_0 = 2.0$ m/s [see also SI video 2]. The bottom half of the drop solidifies, while the still-fluid top portion flows over it. **c** Timeseries of a $\phi = 0.49$ drop impacting at $u_0 = 3.0$ m/s [SI video 3 [97]]. While most of the drop is solidified, the top portion of the drop is in the liquid phase. All scale bars are 1 mm.

$s^{-1} \leq \dot{\gamma}_{impact} \leq 1333\ s^{-1}$. Thus, we are able to span a large spectrum of flow behaviors in these suspensions, and observe how non-Newtonian flow gives rise to a rich variety of impact phenomena. The results we present here take us closer to an understanding of the shear jamming transition and the properties of shear jammed solids.

4.2 Results

Bulk rheometry measurements [Fig. 4.1b] demonstrate the variety of flow behaviors exhibited by our suspensions. At low ϕ (black and pink lines), the fluid viscosity is constant, akin to a Newtonian fluid. Shear thinning (decreasing viscosity) becomes pronounced as ϕ is increased (green and purple curves), and shear thickening (indicated by increasing viscosity) appears for $\phi \geq 0.47$ at high shear stresses (shear stress above 100 Pa, orange, blue, and red curves). We observe fascinating consequences of this non-Newtonian rheology in our impact experiments. At $\phi = 0.47$, where weak shear thickening appears at high stresses in bulk rheology, we observe patches of localised solidification during spreading — panel 3 of Fig. 4.2a shows small solid-like bumps that protrude from the spreading drop, but vanish in panels 4 and 5 [SI video 1[97]]. At higher ϕ, we observe partial solidification of the drop — Panel 2 in Fig. 4.2b shows that the bottom part of the drop acts as a solid, while the top part remains fluid and flows over the solidified region throughout panels 3-5 [SI video 2[97]]. Finally, at $\phi = 0.49$ and high impact velocities, most of drop solidifies as shown in Fig. 4.2c [SI video 3[97]]. Here, we show that this variety of solidification behaviors is a direct consequence of shear jamming[100], evidenced by their occurrence much below the static jamming threshold[101].

We encapsulate this broad range of impact outcomes in a $\phi - u_0$ state diagram [Fig. 4.3]. Green circles, indicating simple spreading [SI video 4[97]], dominate the low ϕ

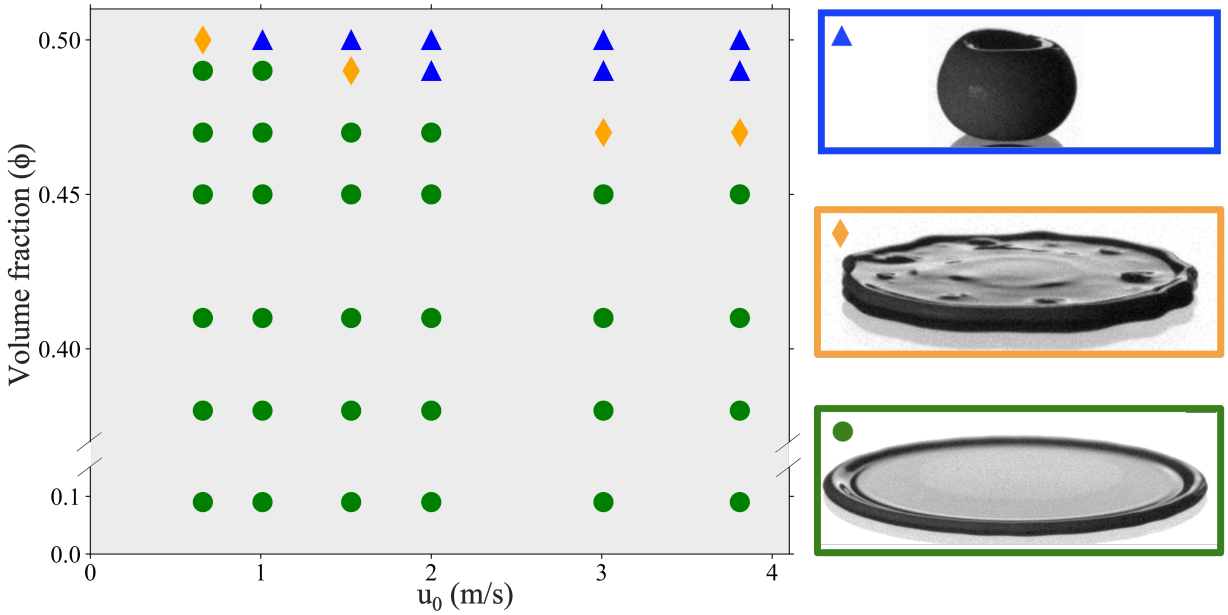

Figure 4.3: **State diagram of colloidal drop impact.** $\phi - u_0$ state diagram summarizing impact regimes; representative snapshots corresponding to these regimes are shown on the right. Green circles denote simple spreading behavior, which dominates the low ϕ, low u_0 region. Orange diamonds indicate that transient pockets of localised solidification were observed during spreading. Blue triangles correspond to the partial/full solidification regime, where the bottom portion of the drop jams after impact, but a shrinking region at the top remains fluid.

and low u_0 region. With increasing ϕ or u_0, the localised solidification regime appears (orange diamonds), followed by the bulk solidification regime (blue triangles), where a larger and larger portion of the drop solidifies upon impact. The transition between these regimes is a function of both ϕ and u_0, as all regimes can be accessed by varying either of the parameters while keeping the other constant. Additionally, we find that the drop behavior is very sensitive to small changes in ϕ, consistent with the transition to shear thickening in rheological measurements [Fig. 4.1b].

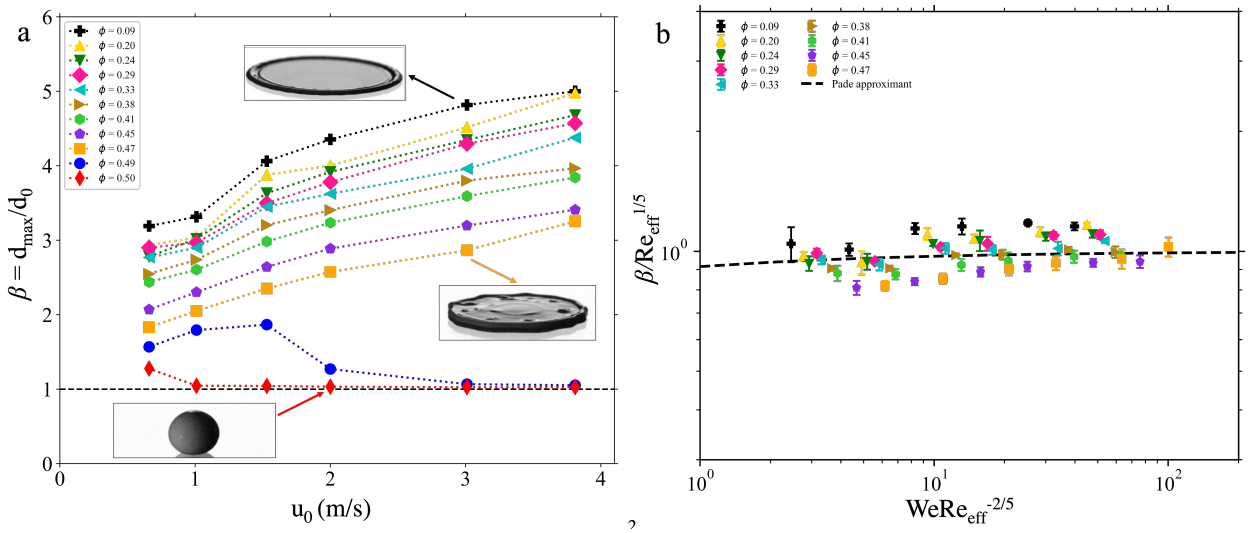

Figure 4.4: **Quantifying maximum drop spreading.** **a** Normalised maximum diameter, $\beta = d_{max}/d_0$, as a function of u_0 for various volume fractions ϕ. For $\phi \geq 0.49$ and high impact velocities, β drops to 1, indicating the drop does not spread. Insets show representative snapshots of simple spreading (upper), localised solidification (middle), and bulk solidification (lower). Dotted lines are guides to the eye, and the dashed black line indicates $\beta = 1$. **b** $\beta/Re_{eff}^{1/5}$ for $\phi \leq 0.47$, plotted against the dimensionless parameter $WeRe_{eff}^{-2/5}$. The dashed black line is the first-order Padé approximant as reported by Laan et al.[14] [Equation 4.3] for Newtonian fluids, fit to our data. Considering the strongly shear thinning nature of our suspensions, the data shows good agreement with the Newtonian model.

To quantify this range of impact outcomes, we compute the normalized maximum diameter of the impacted drops, $\beta = d_{max}/d_0$, and plot this metric against u_0 [Fig. 4.4a]. For $\phi \leq 0.47$, β increases with increasing impact velocity. However, β drops to 1 at $\phi \geq 0.49$ and high impact velocities. This is because the drop no longer spreads after impact (lower inset). This result is consistent with recent studies that observed similar solidification in suspension impact at high ϕ[51, 52]. Our drops remain solid for a few milliseconds; however, they spread like a liquid over the timescale of a second [SI video 5[97]]. Thus, the solid-like state we observe is transient in nature, further evidence that this solidification

is a direct result of shear jamming. A recent result suggests that the substrate wettability affects this timescale of unjamming[52], but this problem remains largely unexplored.

At $\phi \leq 0.47$, the drops spread in a manner qualitatively similar to Newtonian fluids [SI video 4[97]]. Previous experiments[14] with Newtonian fluids have shown that $\beta/Re_{eff}^{1/5}$ scales as the dimensionless parameter $WeRe_{eff}^{-2/5}$, where We is the impact Weber number, $\rho u_0^2 d_0/\sigma$, and Re is the Reynolds number, $Re = \rho u_0 d_0/\eta$. Here, σ is the surface tension of the suspending fluid (for this case water, $\sigma = 72$ mN/m), ρ is the fluid density, calculated as:

$$\rho = \rho_{silica}\phi + \rho_{water}(1-\phi) \tag{4.2}$$

with $\rho_{silica} = 2000$ kg/m^3 and $\rho_{water} = 1000$ kg/m^3, and η is the suspension viscosity. For impacting colloidal drops, the calculation for the Weber number remains identical to Newtonian fluids. Estimating the Reynolds number, however, is less straightforward due to the non-constant fluid viscosity of complex fluids. During the spreading phase, the maximum shear rate can be estimated as $\dot{\gamma}_{spr} \sim u_0/l$, where l is the minimal thickness of the expanding fluid layer. Past work has established that $l \sim 100$ µm for the range of fluid parameters relevant to this work[12]. Estimated this way, the $\dot{\gamma}_{spr}$ values we obtain are of the order 10^4 s^{-1}. Measurements of fluid viscosity at such high shear rates cannot be made via conventional rheometry. Therefore, we use the fluid viscosity at the highest accessible shear rate from our rheology data (see Supplementary Information for more details). For our experimental conditions, the range of dimensionless numbers was $20 < We < 1000$ and $50 < Re_{eff} < 1600$. In Fig. 4.4b, we plot $\beta/Re_{eff}^{1/5}$ against $WeRe_{eff}^{-2/5}$ in the spreading regime. The dashed black line is the first-order Padé approximant fit to our data:

$$\frac{\beta}{Re_{eff}^{1/5}} = \frac{(WeRe_{eff}^{-2/5})^{1/2}}{A + (WeRe_{eff}^{-2/5})^{1/2}}. \tag{4.3}$$

This equation was reported by Laan et al. [14] to interpolate between the inertial and viscous regimes. The parameters $Re^{1/5}$ and $WeRe^{-2/5}$ are based on scaling arguments that consider the balance of inertial, viscous, and capillary effects[12, 14]. For our data, the fit returns $A = 0.09 \pm 0.01$, much smaller than $A = 1.24 \pm 0.01$ reported for Newtonian fluids[14]. Nevertheless, given that the fluids considered in this study are highly shear thinning at higher ϕ, the agreement we report here with Newtonian models is surprising. Our data also shows good agreement with an empirical fit reported by Scheller et al.[19]. Recent work has additionally reported a scaling correcting for surface wettabilty[20]; see Supplementary Information for a further discussion of these models.

In the localised solidification regime [orange diamonds in Fig. 4.3, SI video 1[97]] the bulk of the drop still spreads like a Newtonian fluid [Fig. 4.4b], but shear thickening is apparent via solidified patches that appear and then disappear. These patches appear during the spreading phase, around 1 millisecond after impact. However, indicators of jamming are present earlier, in the form of nonuniformity in the spreading rim of the drop [see for example, panel 2 in Fig. 4.2a]. In most cases, these patches outlive the spreading phase and disappear during the receding phase, over tens of milliseconds. Our observation of this regime coincides with the onset of weak shear thickening in the bulk rheology data [orange curve in Fig. 4.1b]. Moreover, the transient nature of these patches is strong evidence that regions of high viscosity are embedded in a lower-viscosity fluid phase.We note that we can only observe these patches on the drop surface in high-speed imaging data, and there is a large variance in the spatial and temporal distribution of these patches. This limits our ability to extract quantitative information about localised

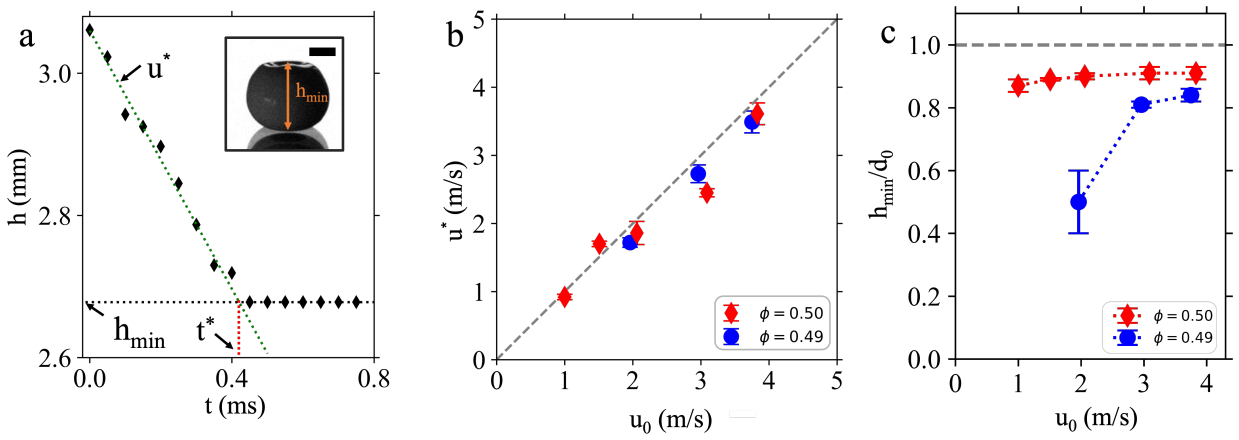

Figure 4.5: **Characterisation of the partial solidification regime.** **a** Height of the drop apex from the impact substrate, plotted against time, for $\phi = 0.50$, $u_0 = 3\ m/s$. h decreases at the speed u^* until time t^*, then plateaus at the value h_{min}. Inset: post-impact snapshot of a drop at the minimum height h_{min}. **b** h decreases at a speed identical to the impact velocity, indicating that over the timescale t^*, the top portion of the drop is unaffected by the impact event. Dashed line corresponds to $u^* = u_0$. **c** h_{min}/d_0 vs. impact velocity u_0. h_{min}/d_0 increases with increasing impact velocity, and then plateaus at a value less than 1, indicating finite compression of the drop along impact axis. Dashed line indicates $h_{min}/d_0 = 1$.

jamming. For higher ϕ, where shear thickening is pronounced, the drop exhibits drastically different behavior, and does not spread at all.

For $\phi \geq 0.49$, a large fraction of the drop solidifies upon impact. To quantify the dynamics of this partially solidified state, we measure the height of the drop apex as a function of time [Fig. 4.5a]. Consistent with another study of impacting shear thickening drops[51], we observe two regimes in the h vs. t curve — a free-fall regime and a plateau regime. Immediately after impact, h decreases at a rate identical to the impact velocity (free-fall regime) [Fig. 4.5b], and then plateaus at a constant value, h_{min} (plateau regime). This is strong evidence that any shear from the impact event has not yet propagated to the top portion of the drop, and hence the top portion must still remain a liquid. Studies

of impacting Newtonian drops have also observed a similar 'free-fall' regime where the drop apex moves at the impact velocity[74, 102, 103]. It is worth noting that in contrast to Newtonian fluids, where a broad transition regime was observed between the free-fall and the plateau regimes, we observe a sudden transition from the free-fall to plateau regime [Fig. 4.5a], a direct indication of a shear jammed drop.

We quantify the spatial extent of solidification by plotting the normalized minimum height, h_{min}/d_0 against u_0 [Fig. 4.5c]. The increase in h_{min}/d_0 with u_0 indicates that a larger and larger volume of the drop is solidified as the impact velocity is increased. Interestingly, at high impact velocities, h_{min}/d_0 plateaus to a value smaller than 1, indicating that the solidified drop also undergoes deformation along the impact direction, along with slight bulging in the plane transverse to impact [Fig. 4.2c]. Furthermore, the high temporal resolution (100,000 fps) of our imaging enables us to capture the details of this solidification as it occurs.

Immediately after impact, we observe a disturbance travelling upward along the drop surface over hundreds of microseconds [orange and green arrows in Fig. 4.6a]. To better visualise this front, we subtract successive frames of the image sequence, so that only the parts that change between frames are highlighted [right panel of Fig. 4.6a, SI video 6[97]]. The location of the front is given by the lower end of the bright edge [Fig. 4.6b]. As this front travels upward, the portion of the drop above the front still maintains its pre-impact curvature [red circles in Fig. 4.6a], indicating that it is unaffected by the impact event until the front reaches it (consistent with $u^* = u_0$, Fig. 4.5b). The angular location of this front plotted against time reveals that the front travels at a constant speed, u_{front} [slope of the line in Fig. 4.6c]. u_{front} increases with increasing u_0, and its value is several times larger than u_0 [Fig. 4.6d]. As evident from the rheology, the suspension thickens

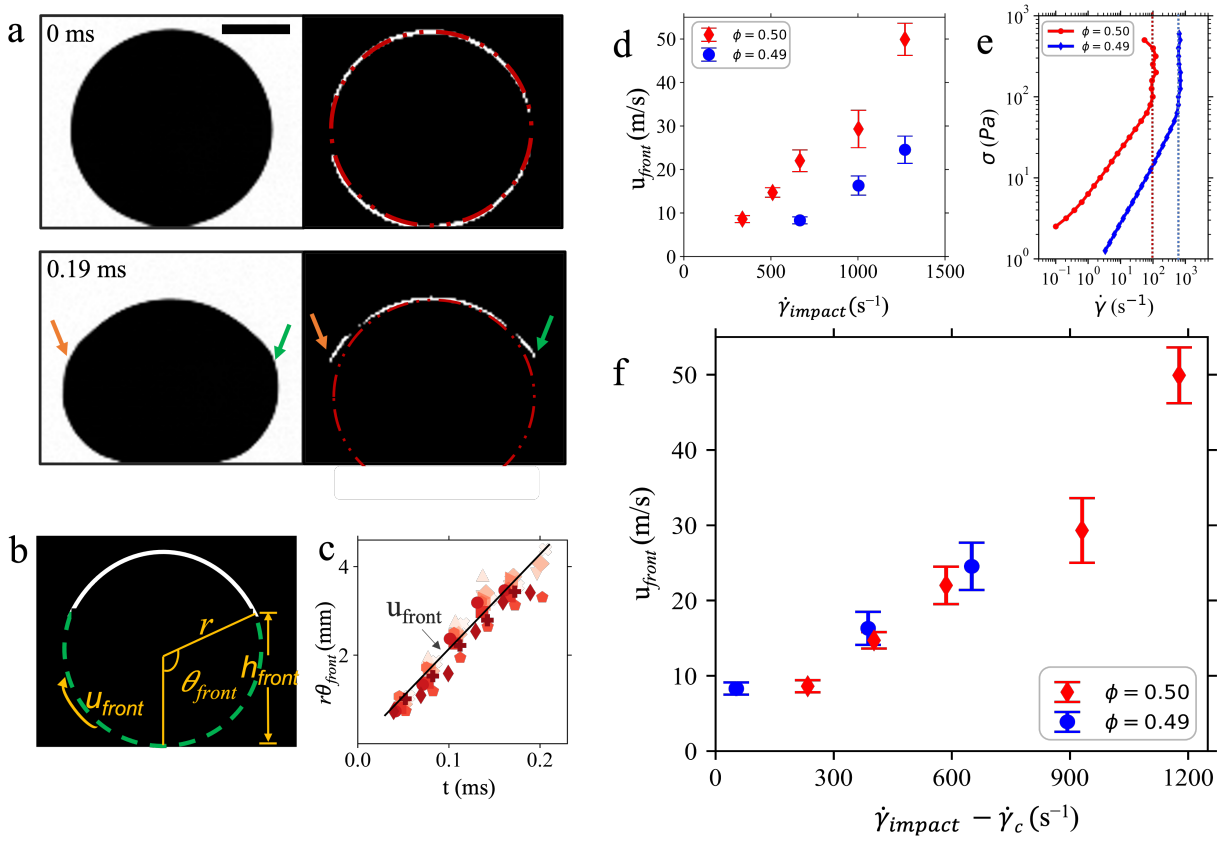

Figure 4.6: **Dynamics of the solidification front.** **a** Timeseries of a $\phi = 0.50$ drop impacting at $u_0 = 2.0$ m/s [SI video 6 [97]]. Right panels are images obtained by subtracting consecutive frames, so that the edge of the solidification front is highlighted (shown by arrows).The red circle indicates the drop profile before impact. Even at 0.19 ms, the portion of the drop above the front maintains its pre-impact curvature. Scale bar is 1 mm. **b** Schematic of a subtracted image of the moving solidification front, outlining relevant parameters. The height, h_{front}, of the edge of the white outline gives the location of the front, which is then converted to $r\theta_{front}$ using the spherical geometry. **c** Example datasets of $r\theta_{front}$ vs. t for $\phi = 0.49$ and $u_0 = 3$ m/s. $r\theta$ vs. t is a straight line, the slope being the front speed along the surface, u_{front}. **d** u_{front} plotted against $\dot{\gamma}_{impact}$. **e** High- ϕ bulk rheological data from Fig.4.1b re-plotted as shear stress vs. shear rate. Dotted lines indicate the onset shear rates $\dot{\gamma}_c$ for shear thickening. **f** The u_{front} data for $\phi = 0.49$ and $\phi = 0.50$, when plotted against $\dot{\gamma}_{impact} - \dot{\gamma}_c$, collapses on a single curve.

when the applied shear surpasses a critical value. Indicated by the dotted lines in Fig. 4.6e, the critical shear rate where thickening is observed, $\dot{\gamma}_c$, is much lower for $\phi = 0.50$ than for $\phi = 0.49$. We plot u_{front} against the excess shear rate over this critical value, $\dot{\gamma}_{impact} - \dot{\gamma}_c$, and the data indeed collapses on a single curve for both ϕ [Fig. 4.6f] . This suggests that the speed of this disturbance is set by this excess shear rate; the physical relevance of this excess shear rate is discussed in the following section.

As the impact velocity is increased, a larger and larger volume of the drop solidifies upon impact. At $\phi = 0.50$ and $u_0 = 4$ m/s, we observe that the drop bounces off the substrate, with the coefficient of restitution $\epsilon = 0.1$ [SI video 7[97]]. This rebound behavior is especially striking given the hydrophilic nature of the substrate. By coupling this coefficient of restitution with the drop's deformation along the impact axis, we can semi-empirically estimate the elastic modulus of the solidified drop. The drop impacts the substrate with an initial velocity u_0, remains in contact with the substrate for time $\Delta t = 200$ µs , and then rebounds with the final velocity ϵu_0. While in contact with the substrate, we measure that the drop is deformed in the direction of impact by the amount $\Delta x = 0.24$ mm. We calculate the force experienced by the drop upon impact using momentum conservation:

$$F = \frac{m\Delta u}{\Delta t} = \frac{m(1+\epsilon)u_0}{\Delta t}, \tag{4.4}$$

To convert the force to a stress, we divide by the contact area for a Hertzian contact[104], $\pi a^2 = \pi d_0 \Delta x/2$:

$$\sigma = \frac{F}{\pi d_0 \Delta x/2} = \frac{2m(1+\epsilon)u_0}{\pi d_0 \Delta x \Delta t}. \tag{4.5}$$

The strain experienced by the drop is $\gamma = \Delta x/d_0$. Thus, the elastic modulus of the re-

bounding drop can be computed as

$$E = \frac{\sigma}{\gamma} = \frac{2m(1+\epsilon)u_0}{\pi(\Delta x)^2 \Delta t}. \tag{4.6}$$

using $m = 2.25 \times 10^{-5}$ kg, we find $E = 5$ MPa. A more thorough estimate using Hertz's equations[104] for two colliding elastic bodies leads to a similar estimate of E. Calculating the elastic modulus in this way for other impact conditions is challenging, as measuring the contact time in the absence of rebound is nontrivial.

4.3 Discussion

In sum, our analysis presents the following picture of the drop dynamics. Upon impact, the drop experiences a large instantaneous shear at the impact point. At high enough volume fractions and impact velocities, this stress manifests itself as pockets of localised solidification embedded in the spreading liquid phase. At even higher volume fractions or shear, a larger and larger fraction of the drop solidifies after impact, but some volume at the top remains liquid. Therefore, the shear front must be dissipating as it moves upward, and the stress falls below the critical stress for shear thickening before the entirety of the drop is solidified. Moreover, at the highest impact velocity, the drop rebounds, and the coefficient of restitution allows us to estimate the elastic modulus of the shear jammed solid, $E = 5$ MPa. Thus, our drop impact experiments provide a unique window to observe shear jamming *as it occurs*, and give rise to a number of questions about the nature of both the shear jamming transition and the resulting jammed solid.

The occurrence of localised solidification coincides with the appearance of weak shear thickening in our bulk rheology data. The fact that these solidified patches vanish over

tens of milliseconds is strong evidence that they are regions of high viscosity embedded in a lower-viscosity fluid phase. Recent rheological studies using boundary stress measurements (BSM) have reported finite regions of enhanced stress in silica suspensions[76, 77, 105]. In these works, Rathee et al.[76, 77, 105] argued that the transition from shear thickening to shear jamming is governed by the growing size of such localised shear jammed regions. Our observations of transient localized solidification are thus striking visual evidence of such a mechanism. Further spatially resolved stress measurements performed on impacting drops[88] could provide more information on the nature of localised solidification in free-surface systems.

In the bulk solidification regime, the coexistence of liquid and solid regions is a result of shear traveling upward from the impact point, and simultaneously dissipating due to the high suspension viscosity. Although recent studies of Newtonian fluids for a large range of viscosities[73, 74] have established the velocity and pressure fields within an impacting drop, they are not directly applicable in case of colloidal systems due to their highly non-Newtonian nature. Numerical work investigating transient shear might be a useful next step to uncover the mechanism of dissipating shear fronts. Though challenging, measurements of the flow inside the drop via methods such as particle tracing, would provide key information about the flow field in an impacting colloidal drop.

The nature of the upward-travelling front raises a number of interesting questions. Before the front reaches the top, the speed of the drop apex u^* is identical to u_0 [Fig. 4.5b], and the curvature of the top portion is the same as it was before impact. This confirms that the information of the impact event reaches the top portion only with the front, thus establishing that it is a solidification front. Why the speed of this front is constant along the drop surface is an intriguing question. One would expect a shear

front to travel through the bulk of the drop, upward from the region in contact with the substrate. Given the visual nature of our measurements on an opaque drop, we can naturally observe this front only on the surface. The most likely explanation, therefore, is that the front we measure is this bulk shear front after it interacts with the drop boundary.

Our experiments are especially well-positioned to capture such a front due to the free-surface conditions here that are absent in other studies of shear fronts. Past work has established that shear fronts in dense suspensions are not a result of densification[69], and their velocity is set by the external driving speed[68–72]. We are able to characterise the dependence of the front speed on applied shear rate due to the unique capability of the drop impact system to apply large and instantaneous shear. At a first glance, Figure 4.6e suggests that reaching a shear rate beyond the critical value is impossible, making an excess rate beyond the critical value unphysical. However, we argue here that this is meaningful for drop impact systems. In a rheometer, resistance to shear in a thickened fluid causes the shear rate to not increase even though applied shear stress increases [Fig. 4.6e]. However, at the instant of impact, the shear rate estimated by $\dot{\gamma} = u_0/d_0$ is a physically relevant quantity. The rationale is as follows: at the moment of impact (before the front has travelled across the drop over ~100 microseconds, Fig. 4.6a,b), the impact point comes to an abrupt halt while the drop apex still moves at the impact velocity [Fig. 4.5b]. Therefore, the velocity difference of u_0 exists across the drop size d_0, leading to $\dot{\gamma} = u_0/d_0$. The front propagation gives us a timescale over which effects of shear jamming are apparent over the whole drop, and we believe that the inability to access high shear rates in a rheometer is a direct consequence of the longer timescale (typically a few seconds) over which shear is applied in rheometry measurements. We emphasize this ability to apply instantaneous high shear is the greatest strength of studying suspension

behavior via drop impact.

The dependence of the front speed on $\dot{\gamma}_{impact} - \dot{\gamma}_c$ in our experiments [Fig. 4.6f] suggests that the suspension properties near the shear jamming transition are governed by the distance from the onset of shear thickening. This is consistent with measurements in static jamming, where material properties depend on the distance from the critical point[106]. The functional form of this dependence potentially contains insights into the nature of the shear jamming transition. Numerical work exploring the impact of suspension drops, although incredibly challenging due to the strong role of hydrodynamics in colloidal systems, might provide crucial information in this respect. Unfolding the physics of these fronts will not only extend constitutive models for complex fluid rheology to much higher stress regimes, but will also help us understand more about the nature of the shear jamming transition.

Due to the transient nature of the shear jammed state, characterising the jammed solid created after impact is challenging. Using the coefficient of restitution of the rebounding drop, we were able to estimate the elastic modulus of the solid phase, $E = 5$ MPa. As rebound only occurred at one impact velocity, how the elastic properties of shear jammed drops are controlled by the impact conditions remains obscure. The use of superhydrophobic substrates promotes rebound, even in Newtonian liquid drops[13]. Further colloidal drop impact experiments on superhydrophobic surfaces could extend the parameter space where drops rebound, and thus provide the information essential to understand what controls the properties of this elastic state. Numerous other properties of the shear jammed solid are of interest: When and how would such a solid fracture? How broad is its linear elastic regime? How do these properties compare to those of static jammed solids?

In conclusion, we conduct highly time-resolved drop impact experiments and systematically probe suspension flow ranging from Newtonian-like to shear jamming. We show that the impact behavior in the spreading regime can be quantitatively understood via an effective viscosity framework, and that the solidification behaviors at high ϕ and u_0 are direct consequences of shear jamming. The free-surface geometry in our system provides direct visual information on how the shear jamming transition occurs, both in parameter space and in time. Shear jamming occurs via a solidification front, the speed of which is set by how far into the shear thickening regime the applied shear rate is. Furthermore, we see this transition occur via a localised solidification regime that cannot be observed via bulk measurements. We believe that drop impact is a powerful experimental tool to investigate macroscopic properties of complex fluids, and provides information that compliments the data from bulk rheometry.

4.4 Methods

Colloidal sample preparation

We fabricated silica spheres in our lab using the Stöber[93, 94] synthesis method. The particle size was determined by the number of feeds: we performed 14 feeds after the initiation of the reaction, resulting in particles with a diameter of 830 ± 20 nm. The reaction mixture was centrifuged and re-suspended in ethanol 3 times; the suspension was then gravity separated to improve monodispersity. The particles were then imaged on the Hitachi S4800 Scanning Electron Microscope [Fig. 4.1a]. The particle size was characterized by measuring the diameter of a representative sample of 100 particles in ImageJ, and the polydispersity reported is the standard deviation in particle size.

A concentrated stock suspension of the silica spheres was prepared in water (with no

surfactant), and the weight fraction was measured by drying 100 μL of the stock suspension. The density of silica (2 g/cm^3) was used to convert weight fractions into volume fractions. Dilutions were then performed to prepare samples of desired volume fractions. The uncertainty in volume fractions reported is 0.5% (0.005) or less, determined by repeated measurements. When not in use, all the sample tubes were sealed using Parafilm and stored in a refrigerator to minimize evaporation and contamination.

Experimental setup

We used Fisherbrand plain glass slides as the hydrophilic impact substrate. The slides were cleaned using a 2.5M solution of NaOH in ethanol and water to remove organic impurities. A micropipette was used to form colloidal drops. The micropipette was mounted on a vertically moving pipette holder to vary impact velocities. We used 15 μL of fluid to obtain drops of 3.0 ± 0.1 mm diameter. The setup was enclosed in a humidity chamber with the relative humidity maintained between 70–80% using a saturated solution of NaCl in water, and the humidity was monitored in real time during experiments. Before every trial of the impact experiments, a vortex mixer was used to re-disperse the sample, ensuring that it was consistently well-mixed.

The impacting drops were backlit using a white LED light, and filmed using two high-speed cameras. The first camera, a Phantom V2512, captured the side-view of the impacting drop at 100,000 frames per second. The second camera, a Phantom V640L, filmed at 20,000 fps. It was tilted at an angle of 15° to gather information on how the impact affected the top surface of the drop. The experiment was repeated at least 5 times for each impact condition to ensure reproducibility.

Rheological studies

Stress-controlled rheological measurements were performed on the colloidal samples

over $0.09 \leq \phi \leq 0.50$. The measurements were done on a TA Instruments Discovery HR-2 rheometer at room temperature ($\sim 21°C$) using the cone-plate geometry with 40 mm diameter and a 1° cone angle. The truncation gap was 25 μm. We covered the edges of the samples with a microscope immersion oil to minimize evaporation. The samples were pre-sheared to remove effects of shear history.

Data analysis

All high-speed videos were background-divided and analysed using ImageJ. The plots were made using python, and all errors reported are one standard deviation calculated over at least 5 trials (corresponding to a 68% confidence interval). The maximum drop spread d_{max} was determined by locating the frame in the impact timeseries where the extent of the spreading drop was the greatest. The height of the tallest point on the drop relative to the substrate, h, was measured for each frame in the image sequence. The minimum height h_{min} was defined as the drop height at the crossover point between the decreasing and the plateau regimes in the h vs. t plot. The time of first observation of h_{min}, measured since the impact event, was defined as t^*. The slope of the linearly decreasing regime in the h vs. t plot was defined as u^*. To calculate the coefficient of restitution, the speed of the drop before impact u_0, and the speed after rebound, u_f were computed using several frames of the image sequence. The coefficient of restitution was then computed as $\epsilon = u_f/u_0$.

To calculate the speed of the upward-moving front, the side-view impact videos recorded at 100,000 fps were used. For every frame of the image sequence, the pixel-wise difference between consecutive frames was taken in ImageJ, so that only the elements that changed between consecutive frames (corresponding to the location of the moving front) were highlighted [SI video 7 [97]]. This enabled us to locate the jamming front with a

time uncertainty of 10 μs. The images were then adjusted for brightness and contrast to enhance the moving front. The vertical height h_{front} of the disturbance from the impact substrate was measured for each frame of the image sequence, until the front was no longer visible. For every high-speed video, the left and right half of the drop were separately analyzed to obtain two datasets for $h_{front}(t)$. In order to convert h_{front} to the position along the drop surface, $r\theta_{front}(t)$, we approximated the drop profile as a circle of radius $r = 1.5\ mm$ (disregarding the slight deviation from spherical shape during front propagation), and used the relation $h_{front}(t) = r(1 - \cos\theta_{front}(t))$, such that $\theta_{front}(0) = 0$ at the impact point, to obtain the angle $\theta_{front}(t)$. A line was then fit to the $r\theta_{front}$ vs. time plots, and the slope, averaged over the two halves of the drop and several movies for each impact condition [Fig. 4.6c], was reported as u_{front} with error bars indicating the standard deviation.

CHAPTER 5

DROP IMPACT: FURTHER CHARACTERIZATION OF THE SHEAR JAMMED STATE AND EFFECT OF PARTICLE ANISOTROPY

In the last chapter, our results on the shear jamming dynamics of an impacting drop made of spherical silica suspensions were discussed. Here, I discuss further considerations on the drop impact dynamics of suspensions, that includes a preliminary characterization of the shear jammed solid, the re-fluidization dynamics after the shear jamming event, and the effect of particle shape on both quantitative and qualitative aspects of impact. In section 5.1, I describe and compare two ways of estimating the elastic modulus of an impacted drop in the absence of rebound, which gives us information about how properties of the solidified drop depend on the impact conditions. In section 5.2, the longer-timescale dynamics of the impacted drops are described, where I observed that the re-fluidization dynamics of drops depends on the impact history. Finally, in section 5.3, I outline the effect of particle anisotropy on impact dynamics, where I show that drops of rod-shaped particle suspensions not only shear jam at much lower ϕ and impact velocities, the post-impact drop behavior is qualitatively different from that observed for sphere suspensions. These preliminary observations outline experimental avenues for the near future, which will help us understand the nature of shear jamming upon impact in more detail.

5.1 Elastic modulus estimation in the absence of rebound

Estimating the elastic modulus of the shear jammed solid after impact provides us with a window into the properties of the shear jammed solid. However, as discussed in the previous chapter, we are able to observe rebound, and hence directly measure the contact time and the coefficient of restitution of the drop, at only one impact condition. Equation 4.6 was used to estimate the elastic modulus for the rebounding drop.

In the absence of rebound, however, despite the observation of bulk shear jamming, such an estimation of E is nontrivial. As the drop never leaves the substrate, we do not have a reliable measure of the contact time relevant to estimate the elastic modulus. However, even approximate information we can extract from our data would take us closer to understanding the properties of shear jammed solids. Here, we attempt to obtain a crude estimate of the contact time *in the absence of drop rebound*, so as to estimate E over multiple impact conditions.

For impact conditions where the drop does not rebound, we can estimate contact time by assuming a simple harmonic behavior. With this assumption, the drop is maximally compressed in the vertical direction at time t^* after impact and it would take the same amount of time to (hypothetically) de-compress and bounce back from the substrate. Thus the 'simplified contact time' is $t_{contact} = 2t^*$ [Figure 5.1]. The equation to thus compute E_{linear} reads:

$$E_{linear} = \frac{2mu_0}{\pi d_0 (\Delta x)^2 \times 2t^*} \tag{5.1}$$

This equation is similar to Equation 4.6, with $\epsilon = 0$ and substituting $\Delta t = 2t^*$. Identical to Equation 4.6, Δx is the minimum height of the drop apex from the substrate. The errors

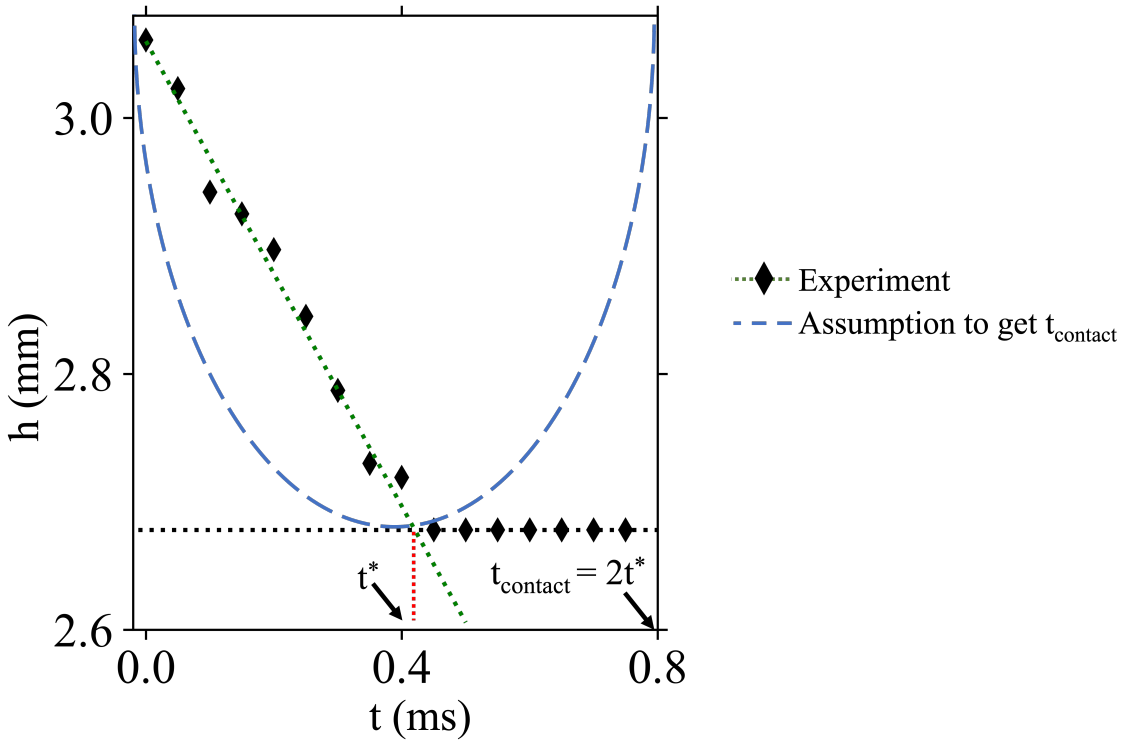

Figure 5.1: **Sketch of the symmetry assumption for calculating E_{linear}, overlaid on experimental data of Fig. 4.5a.** The blue dashed line indicates the motion of an ideal spring-mass system bouncing off of a substrate. Assuming the drop to follow this motion leads to the simplified contact time,$t_{contact} = 2t^*$.

in E_{linear} are computed as

$$\frac{\Delta(E_{linear})}{E_{linear}} = \frac{\delta(u_0)}{u_0} + 2\frac{\delta(\Delta x)}{\Delta x} + \frac{\delta(t^*)}{t^*} \tag{5.2}$$

where $\delta(u_0)$ is the standard deviation in u_0, from repeated experimental measurements, and likewise for other variables. As shown in Figure 5.2, E_{linear} thus computed for two ϕ values, plotted against $(\dot{\gamma}_{impact} - \dot{\gamma}_c)$ collapses well onto a power law (dashed black line) with the exponent of 2.1.

A number of assumptions go into this estimate of E_{linear}. In order to calculate a proxy

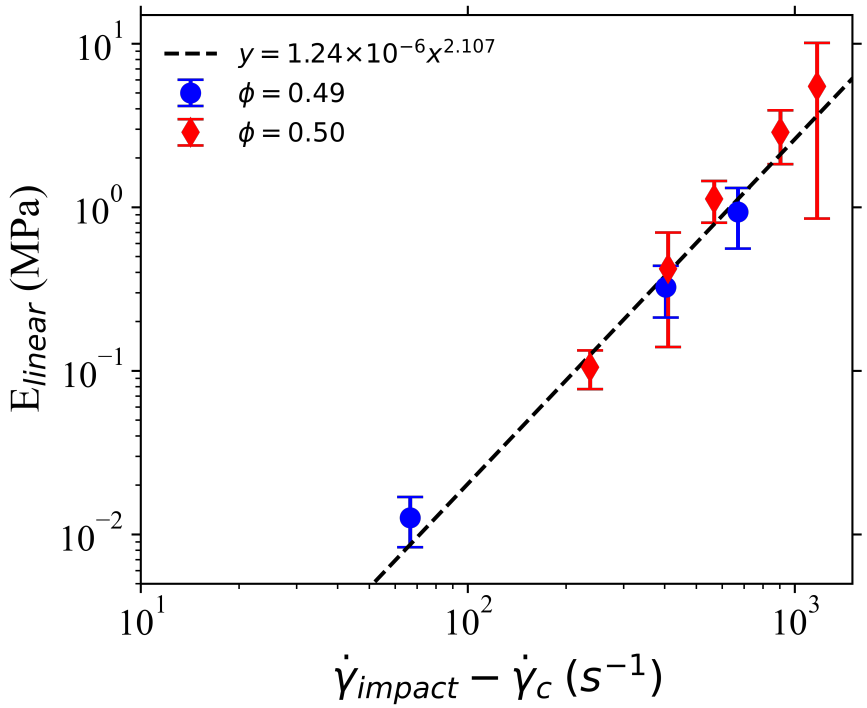

Figure 5.2: **Elastic modulus estimated using simplified contact time $t^{\star}_{contact}$, plotted against $\dot{\gamma}_{impact} - \dot{\gamma}_c$.** The dashed black line indicates the power-law fit. The data collapses well, and the power-law exponent of 2.1 suggests that E_{linear} scales quadratically as the rescaled shear rate.

for Δt, we model the drop as an ideal spring-mass system, so that the time it spends being compressed and de-compressed are identical [Figure 5.1]. This is clearly far from our experimental observation of the plateau in drop height after initial compression [Figure 4.5a]. Thus, in addition to the linearity assumption, we are effectively neglecting any interactions with the substrate. We note that dissipation within the drop is accounted for, as $\epsilon = 0$ for a non-rebounding drop. We assume that the drop behaves as an elastic solid bouncing from a substrate in the absence of gravity. This is clearly not true; the drop is a fluid before experiencing any shear caused by impact. The actual post-impact state of the drop is far more complex, since for most impact conditions the top portion of

the drop still remains a fluid even after impact. However, we believe that this model is an informative first step to glean any information about material properties, given how little is known about the effect of applied shear on the properties of shear jammed solids. Despite all the simplifying assumptions, we are surprised to see such a good collapse with respect to $(\dot{\gamma}_{impact} - \dot{\gamma}_c)$. Below, we argue that a quadratic dependence of the elastic modulus on $(\dot{\gamma}_{impact} - \dot{\gamma}_c)$ (exponent 2.1 from the fit) is physically sensible.

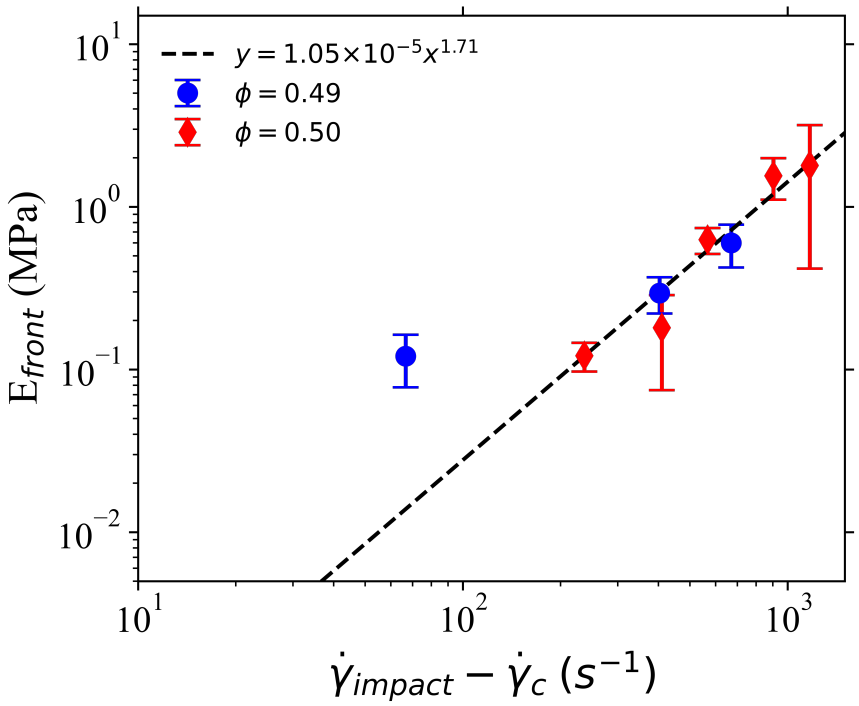

Figure 5.3: **Elastic modulus estimated by assuming u_{front} to be the bulk sound speed, plotted against $\dot{\gamma}_{impact} - \dot{\gamma}_c$.** The dashed black line indicates the power-law fit. The data collapses well, and the power-law exponent of 1.7 is close to the quadratic behavior of E_{linear}.

We can estimate the elastic modulus of this solid in another way. By assuming u_{front} as the speed of sound in the shear jammed material, we can use the equation $u_{front} = \sqrt{\frac{E_{front}}{\rho}}$, where E_{front} is the elastic modulus estimate, and ρ is the density of the suspension. Thus

the elastic modulus is calculated as

$$E_{front} = u_{front}^2 \rho, \tag{5.3}$$

With errors given by

$$\frac{\delta(E_{front})}{E_{front}} = \frac{2\delta(u_{front})}{u_{front}} + \frac{\delta(\rho)}{\rho}. \tag{5.4}$$

Although u_{front} as the sound speed in the bulk of the drop is a naive assumption, what we know about bulk and surface sound speeds from the literature [104] indicates that this is a good order of magnitude estimate. Figure 5.3 shows E_{front} thus computed as a function of $(\dot{\gamma}_{impact} - \dot{\gamma}_c)$. Except for one data point at $\phi = 0.49$, the data again shows a good collapse, the power-law exponent being 1.7. We expect a quadratic power-law exponent in this case, as E_{front} scales quadratically as u_{front} and u_{front} scales linearly with $\dot{\gamma}_{impact} - \dot{\gamma}_c$ [Figure 4.6f]. The deviation from the expected value of 2 can be attributed to the outlier at $\phi = 0.49$ and $u_0 = 2$ m/s.

Figure 5.4 shows the comparison of the two elastic modulus estimates, E_{linear} and E_{front}. The two values show good agreement. The scaling of the elastic moduli with $(\dot{\gamma}_{impact} - \dot{\gamma}_c)$ is further evidence that the properties of a shear jammed material depend on the magnitude of applied shear beyond the critical value.

Nevertheless, the calculation of E for a rebounding drop is much more reliable than that of E_{linear} in the absence of rebound. Impact experiments on hydrophobic surfaces, as they might promote rebound at lower shear conditions, are a logical next step to improve the elastic modulus estimate. To obtain more precise information about these elastic properties, further numerical and experimental measurements of the sound speed inside

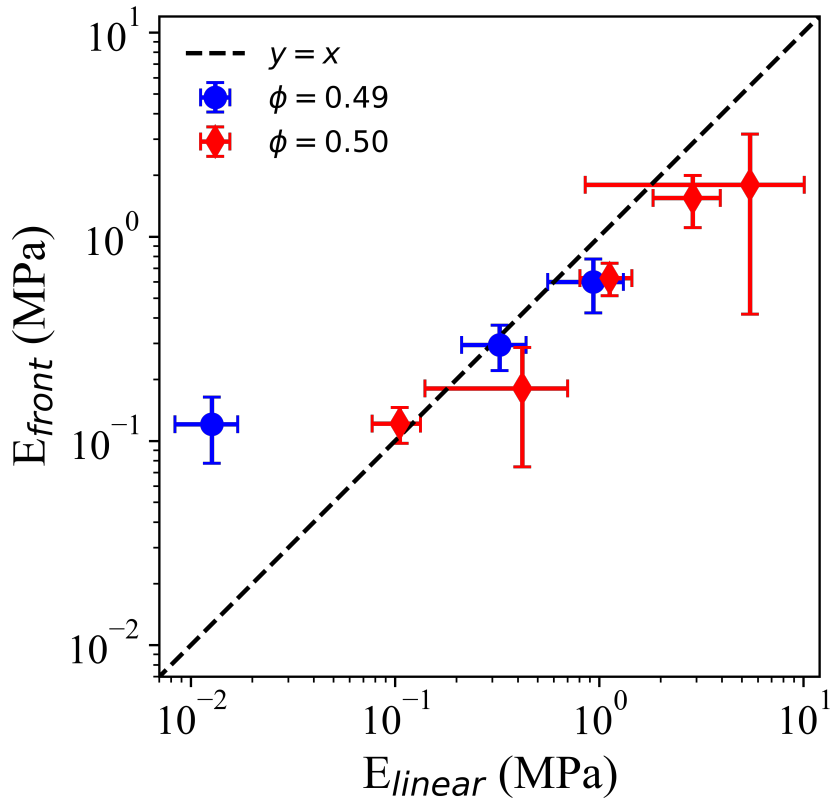

Figure 5.4: **Comparison of the two estimates of elastic modulus, E_{linear} and E_{front}.** Dashed black line denotes $y = x$. Despite the very crude nature of both estimates, they agree reasonably well.

shear jammed systems would be informative.

In addition to affecting the properties of the transient shear jammed state of the drop, the memory of high shear might also manifest into how this material 'unjams' over longer timescales. We discuss the unjamming dynamics of impacted drops in the next section.

5.2 Unjamming of solidified suspension drops

For the impact conditions where a concentrated suspension drop shear jams, the resulting solidification lasts for tens of milliseconds. Over longer timescales, the shear jammed

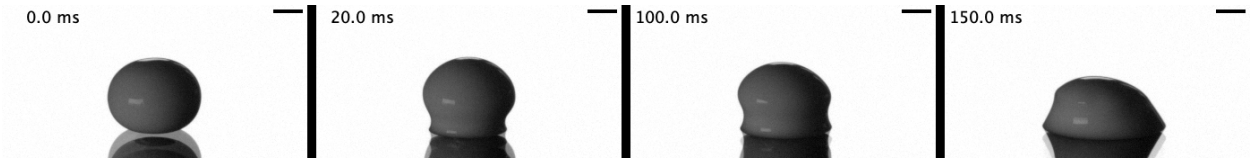

Figure 5.5: A $\phi = 0.49$ drop, impacted at 4 m/s, unjams over hundreds of milliseconds. The spreading process continues over several seconds (not shown in the timeseries above). Scale bars are 1 mm.

drops re-fluidize. This 'unjamming' corroborates that the solidification was indeed due to shear jamming, and that the drops were not dried out due to evaporation. As discussed in section 5.1, the properties of the shear jammed drop depend on the instantaneous shear experienced by the drop. In order to explore the effect of shear memory on the unjamming dynamics, I recorded the unjamming drops at a frame rate of 200 fps. Other experimental details were identical to those reported in chapter 4.

Figure 5.5 shows a timeseries of a ϕ =0.49 drop impacted at $u_0 = 4$ m/s. On the timescale of hundreds of milliseconds, the drop starts spreading from its bottom part where it is in contact with the substrate. The spreading proceeds slowly, and continues for seconds[Figure 5.6]. I record the spreading dynamics until t=50 seconds after impact, as spreading slows down significantly beyond that time. Figure 5.6 shows the spreading diameter of $\phi = 0.49$ drops. The $u_0 = 0.7$ m/s data point serves as a control experiment for viscous spreading, as shear jamming does not occur at this low velocity. I compare the spreading dynamics during unjamming at higher impact velocities to this control data, in order to explore the effects of shear memory on unjamming. As seen in Figure 5.6, the final spreading diameter of drops is smaller for larger impact velocities. Thus, unjamming follows the opposite trend of inertial spreading, where larger impact velocities lead to more spreading. Thus, this reversed trend might be a consequence of shear memory in the drop.

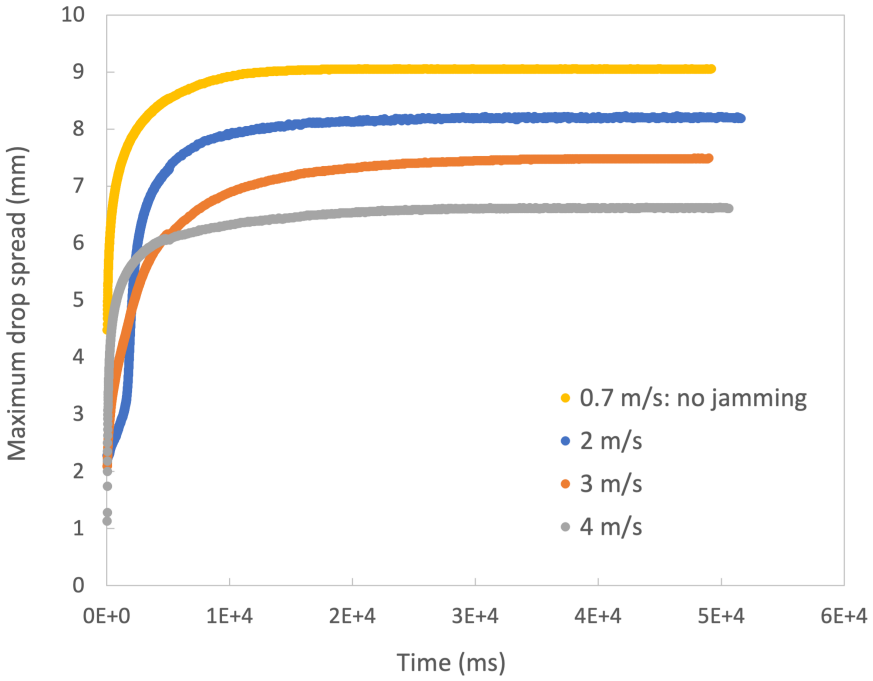

Figure 5.6: Spreading of shear jammed drops at ϕ =0.49 due to unjamming. The drops impacting at $u_0 = 0.7$ m/s do not undergo shear jamming, and this data serves as a control experiment. During unjamming, drops impacted at higher velocities spread to a smaller extent. Therefore, shear jammed drops show a trend opposite to that of fluid drops, where drops spread more at higher impact velocities.

Figure 5.7 shows the normalized spreading size of the unjammed drops, for both ϕ = 0.49 and $\phi = 0.50$. I note that I recorded the spreading dynamics for 50 seconds, therefore it is possible that the spreading diameter grew beyond the values reported in Figure 5.7. However, the spreading slowed down significantly within 50 seconds, and I do not expect large changes in spreading diameter beyond this time. For both volume fractions, the normalized spread decreased with increasing impact velocity. All of these values were smaller than the controlled experiment at $u_0 = 0.7$ m/s, where the drop is expected to undergo viscous spreading. Therefore, the unjamming behavior cannot be attributed to Newtonian effective viscosity effects alone. As higher impact velocities lead to higher

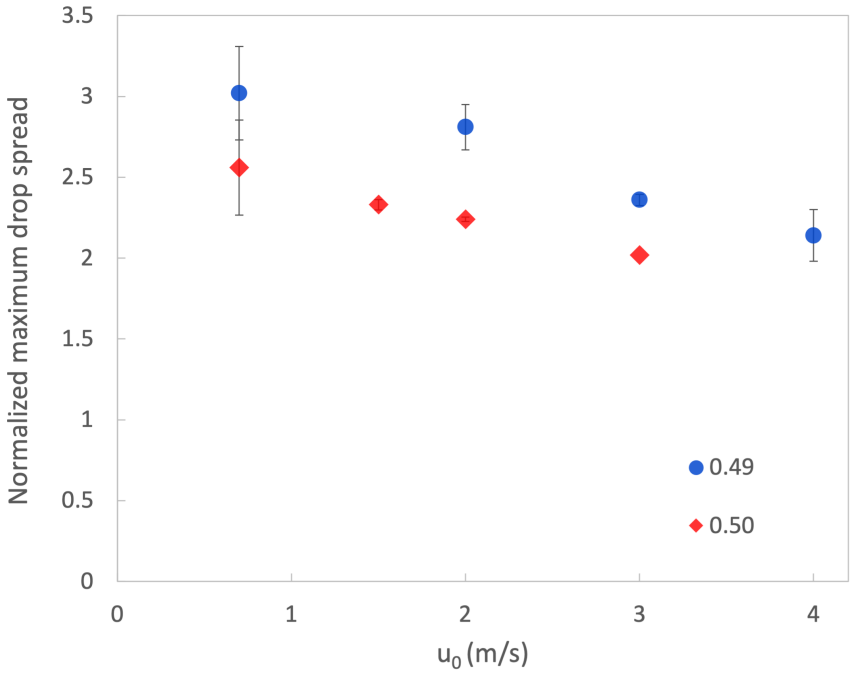

Figure 5.7: Maximum spread of shear jammed drops at ϕ =0.49 and ϕ =0.50 due to unjamming. The drops impacting at 0.7 m/s are control experiments, as shear jamming does not occur at this impact velocity. For both ϕ =0.49 and ϕ =0.50, the normalized maximum spreading diameter decreases with increasing impact velocity. This trend is exactly opposite of inertial spreading of fluid drops in the absence of shear jamming.

instantaneous shear rates experienced by the drop, it is possible that drops impacted at higher velocities retain the information of this shear, and behave as more and more viscous fluids due to shear thickening. Thus, my observations point to the possibility that shear memory affects the unjamming dynamics due to the highly shear thickening nature of our colloidal suspensions at ϕ =0.49 and ϕ =0.50.

There are many other considerations to how unjamming proceeds. As the timescale for unjamming is long relative to the solidification timescale, the effects of particle sedimentation might be significant. Whether large gradients of particle density are present within an unjamming drop needs to be explored further. Particle tracking in an index-

matched drop might be useful in this regard. Impact experiments of dense suspension drops on hydrophobic substrates have reported the drops to have stayed jammed for several days [52]. It would be interesting to explore whether this was an effect of drying or whether the substrate alters unjamming dynamics in a non-trivial way. Measurements of the final contact angle of the unjammed drop would be informative to understand how capillary effects connect to the re-fluidization process after shear jamming.

5.3 Effect of particle anisotropy: impact of suspensions of rod-shaped colloids

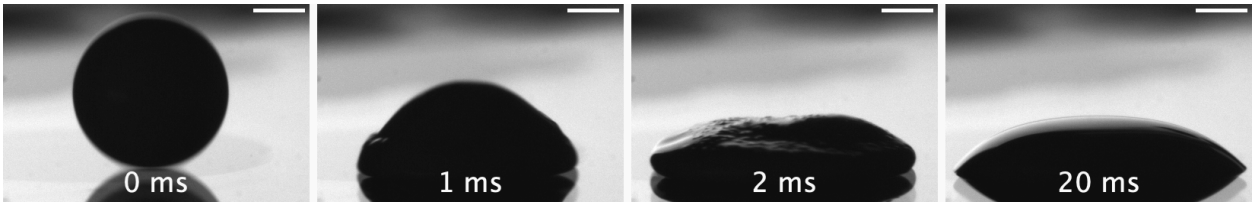

Figure 5.8: Timeseries of an AR 11, ϕ =0.35 rod suspension drop impacting on a glass substrate at u_0 =1.5 m/s (see also SI video 1 [107]). Scale bars are 1 mm. At 1 ms, the drop shows an irregular mushroom-like shape, suggesting shear jamming. At 2 ms, patches of localized jamming are visible on the drop surface, which look qualitatively different from ones observed in sphere suspensions. The localized jamming patches disappear quickly, and are not visible at 20 ms.

In addition to the suspension volume fraction and impact conditions, particle shape is a pertinent parameter to the post-impact behavior of colloidal suspension drops. Rheological data for suspensions with rod-shaped particles shows that shear thickening occurs at a lower value of ϕ, and over a broader range of ϕ [101]. The lower ϕ value for thickening can be expected, as the larger surface area of rod-shaped particles facilitates forming contacts with neighbouring particles, causing resistance to motion at lower concentrations. To study how these rheological properties alter impact behavior, I performed impact experiments on rod-shaped suspensions made of silica rods with the aspect ratio

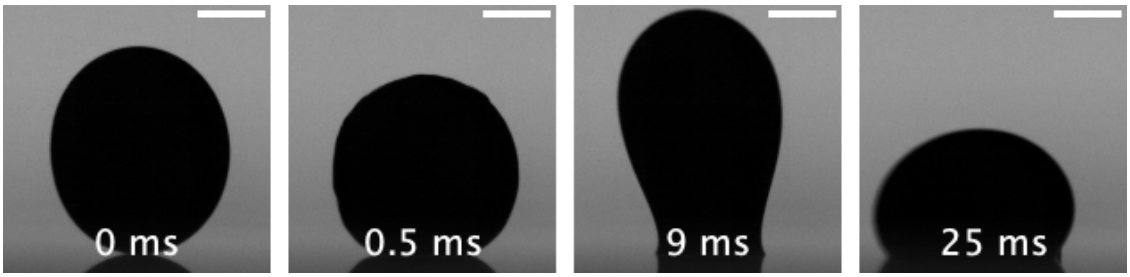

Figure 5.9: Timeseries of an AR 11, ϕ =0.45 rod suspension drop impacting on a glass substrate at u_0 =1.5 m/s (see also SI video 2 [107]). The drop height reduces, then it increases as the drop tries to rebound but cannot detach from the substrate, and decreases again as the drop falls down under gravity.

(AR: the ratio of the length and diameter of the rods) of 11. I synthesized the rod-shaped particles in the lab [See Appendix A] using the procedure by Kuijk et al. [108]. Unlike sphere synthesis, the yield of the rod synthesis is very low ($\sim$ 400 µL for a 1L synthesis batch), and 12 synthesis runs had to be performed to obtain enough high-quality rods for the impact experiments.

Figure 5.8 shows a timeseries of a ϕ =0.35 drop of AR 11 rod suspensions impacted at u_0 = 1.5 m/s (see also SI video 1 [107]). At 1 ms, I observe a thick rim near the drop bottom, while the top part remains in a spherical cap shape. At 2 ms, I observe protrusions on the drop surface that vanish in the next panel at 20 ms. This behavior is similar to the behavior observed for ϕ = 0.47 drops of sphere suspensions [panel 2 in Figure 4.2a], indicating that this is localized solidification. The patches of localized jamming observed here have qualitative differences when compared to those in sphere suspensions [panel 3 in Figure 4.2a], which is to be expected because of particle anisotropy. It is surprising that localized solidification is present at a much lower ϕ of 0.35 (as opposed to ϕ =0.47 for sphere suspensions) in anisotropic suspension impact. Additionally, the impact velocity at which localized jamming is apparent in rod suspensions, 1.5 m/s, is also smaller than

that of 3 m/s for sphere suspensions.

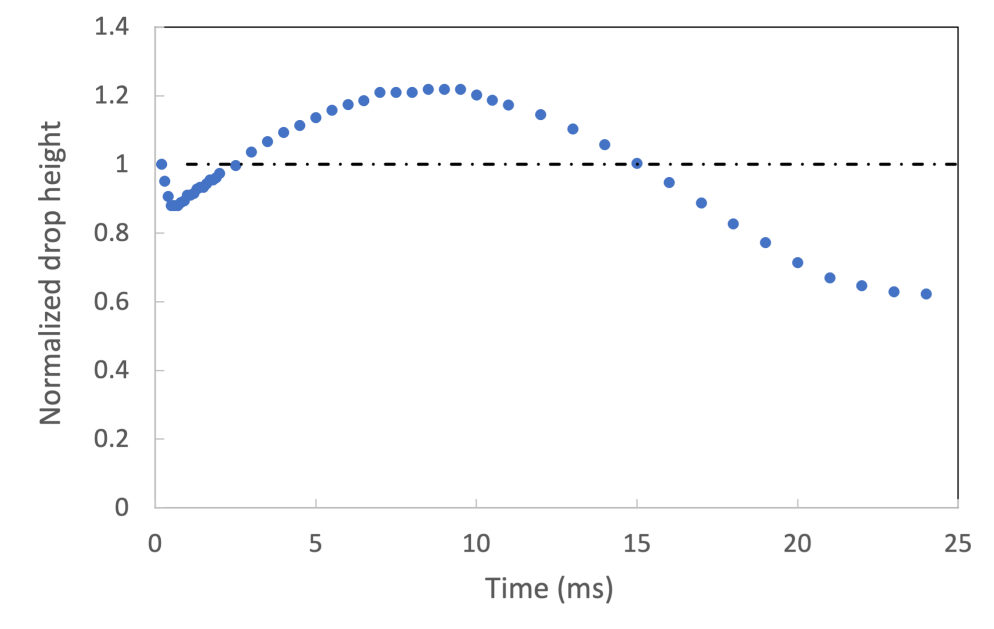

Figure 5.10: Height of the drop apex vs. time for an impacted rod suspension drop, with AR 11 rods, ϕ =0.45, u_0 = 1.5 m/s. Scale bars are 1 mm. The height variation is drastically different from that observed for sphere suspension drops, Figure 4.5a. Throughout this time, the drop bottom remains attached to the substrate, in contrast to a rebounding drop observed for sphere suspensions at ϕ =0.50 and u_0 = 4 m/s. This behavior suggests that the interaction of the drop with a substrate is altered in the presence of elongated particles.

Figure 5.9 shows a timeseries of a ϕ =0.45 drop of AR 11 rod suspensions impacted at u_0 = 1.5 m/s (see also SI video 2 [107]). The drop does not spread, instead it first decreases in height and then tries to lift off of the substrate. However, the bottom of the drop remains adhered to the substrate, leading to an imperfect rebound. Additionally, unlike sphere suspensions, the rod suspension drop does not show a depression on the top. In Figure 5.10, the normalized height of the drop apex is plotted against time. The normalized height briefly drops below 1, then rises to 1.2, before falling again. This behavior is very different from that shown by sphere suspensions in the absence of rebound,

where the drop height linearly decreases and plateaus [Figure 4.5a]. It is more practical to compare this behavior to complete drop rebound observed for sphere suspensions, except that for rod suspensions, the drop bottom is unable to detach from the substrate. I additionally note that performing experiments on $\phi > 0.45$ was not possible, as the suspension thickened beyond the point of forming spherical drops. This occurred at $\phi > 0.50$ for sphere suspensions. Therefore, the ϕ value at which strong shear thickening occurs is lower for anisotropic suspensions, consistent with rheology data [101].

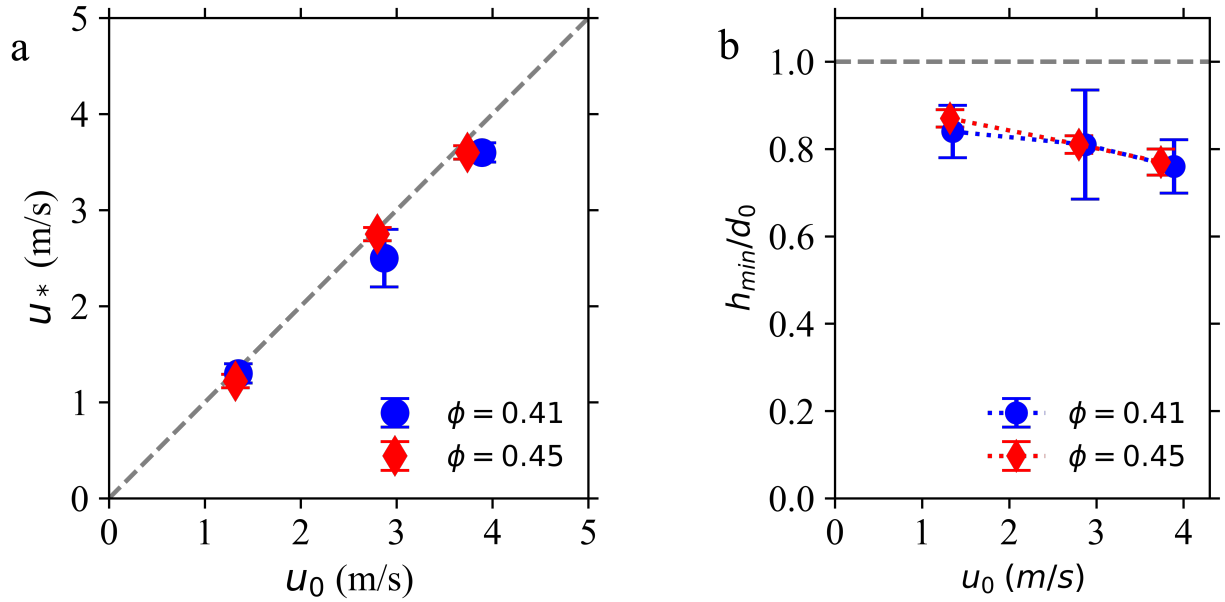

Figure 5.11: **a** The velocity of the drop apex immediately after impact, $u\star$, plotted against the impact velocity, u_0, for two volume fractions of AR 11 rod suspension drops. Similar to figure 4.5b, $u\star = u_0$ within error, indicating that the information of impact has not propagated to the drop apex. **b** h_{min}/d_0 vs. impact velocity for both ϕ. Unlike figure 4.5c, h_{min}/d_0 decreases with impact velocity, capturing the qualitative different behaviour of the shear jammed drop of rod suspensions.

In order to compare the impact dynamics of rod suspension drops to their counterparts with spherical particles, I plot the speed of the drop apex just after impact ($u\star$)

against the impact speed (u_0) [Figure 5.11a]. Similar to spheres, $u\star$ is equal to u_0 within error, for both $\phi = 0.41$ and $\phi = 0.45$. On the other hand, as shown in figure 5.11b, the normalized drop deformation increases with increasing u_0. This trend is not consistent with that for sphere suspensions [Figure 4.5]. This result combined with the qualitatively different drop behavior, indicates that rod suspensions form a completely different kind of solidified material as a response to shear.

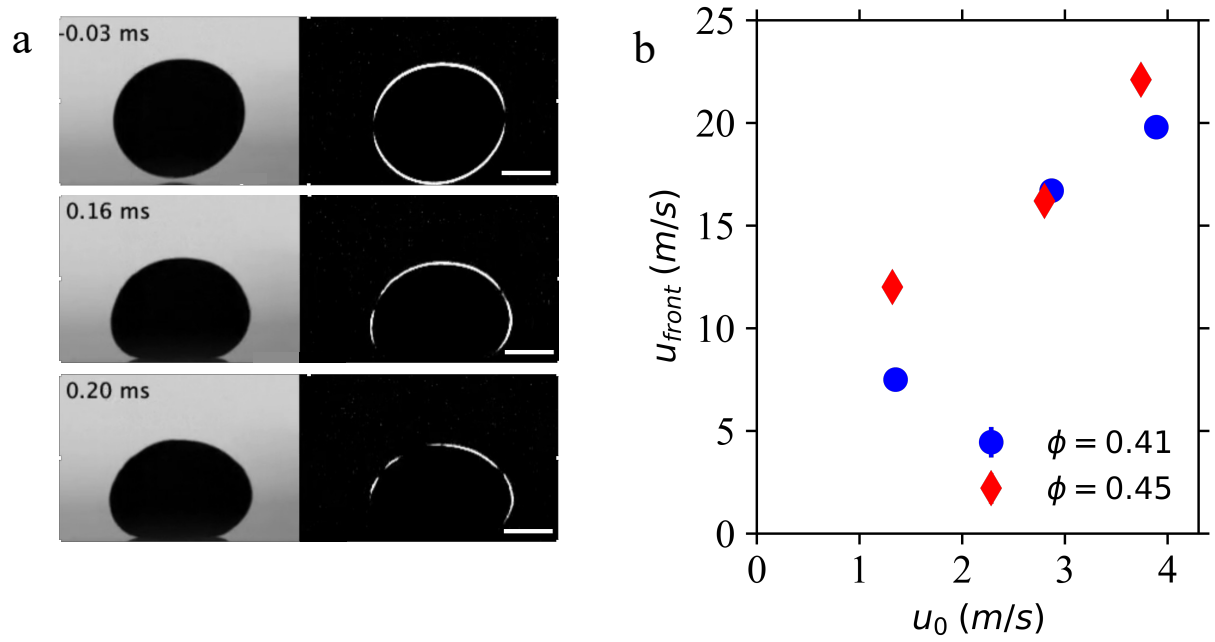

Figure 5.12: **a** Timeseries of an AR 11 rod suspension drop after impact, along with the differenced images. Similar to figure 4.6a, we observe a front travelling upward on the drop surface. **b** The front speed along the surface, u_{front}, plotted against u_0. u_{front} increases with u_0 for both ϕ values.

As demonstrated by figure 5.11a, the information of impact takes finite time to reach the drop apex. Corroborating this, we observe as shown in figure 5.12a, a solidification front travelling along the drop for impacting rod suspension drops too. By measuring the time taken by these fronts to reach the drop apex, I calculated the approximate front

speed along the surface, u_{front}. Similar to sphere suspensions, u_{front} is several times larger than u_0 and increases with increasing u_0. These similarities suggest that the solidification dynamics after impact of rod suspension drops are very similar to those observed for spheres. However, the drop behavior *after* solidification being drastically different (figure 5.10 as opposed to figure 4.5a) suggests that the resulting material after solidification varies dramatically in its properties, when particle aspect ratio is different.

Moreover, as shown in figure 5.12b, u_{front} values lie practically on the same curve for both ϕ values. This result, and a similar collapse in figure 5.11b, indicates that for AR 11 rod suspensions, the solidification dynamics do not change drastically over this relatively large range of ϕ (0.05, as opposed to 0.01 for similar data in sphere suspensions). This could be a potential indicator that the critical shear rate for these suspensions changes very little between $\phi = 0.41$ and $\phi = 0.45$.

My experimental results on impacting rod suspension drops suggest that the dynamics of solidification during the short timescale after impact (¡ 1 ms) are largely unaffected by particle aspect ratio. However, the response of the suspension to this solidification, and in turn the resulting solid, seem to dramatically differ in not only quantitative, but qualitative ways. While for spheres, we observed a progressively larger fraction of the drop solidifying from the bottom and exhibiting a liquid-like region near the apex, we observe no such depression for impacted rod suspension drops. Instead, we observe the drops undergo an imperfect rebound, where the top of the drop moves upward but the bottom of the drop remains tethered to the substrate. Two broad mechanisms can be hypothesized from my observations: either the bulk of the drop forms a qualitatively different, much squishier solid that can deform easily while staying tethered to the substrate, or the presence of elongated particles alters the contact-line dynamics between the

drop and the substrate, causing a strong attachment to the substrate that causes imperfect rebound. Measurements about the dynamics *inside* the drop would be key to understand these dynamics. In addition, the effect of an altered contact line could be studied using substrates of varying wetting properties.

In summary, the preliminary analysis of the rod suspension impact suggests that impacting drops exhibit interesting behaviors, ranging from localized solidification to bulk shear jamming with partial rebound, over a larger range of ϕ and u_0. This is not only consistent with the bulk rheometry where shear thickening is reported for a wider ϕ range for high-AR particle suspensions, the imperfect rebound where the drop bottom stays attached to the substrate points to non-trivial interaction of the fluid with the substrate in the presence of particle anisotropy. The presence of small amounts of polymeric additives have been reported to suppress rebound in impacting Newtonian drops [89, 109–113], and contact-line dynamics are suggested to be the primary mechanism of bounce suppression [114]. Whether the mechanism of bounce suppression for anisotropic colloidal suspensions has similarities to that of polymeric drops is an interesting future question to explore, allowing us to control fluid adhesion to the substrate in a range of industrially relevant systems.

Revealing the microscopic mechanism of shear jamming in impacting drops is highly non-trivial, even in the case of sphere suspensions. Particle anisotropy adds further complexity in the form of particle orientation. Rod-shaped colloidal particles are often used for modelling liquid crystals [108], and it is likely that they align in response to shear. It would be very interesting to consider the correlation of this orientation with the direction of the impact axis. Additionally, the rebound suppression indicates that particles alter contact line dynamics. Rods might also respond to shear differently along the drop

surfaces, in addition to affecting contact and bulk properties. Thus, impact experiments with rod suspensions can provide useful information on how anisotropic particles respond to directional stresses. Observing the impacted drop under polarized light might be helpful in future experiments on these lines.

CHAPTER 6
RUPTURE OF COLLOIDAL SOAP FILMS

6.1 Introduction

Foams, bubbles and films are ubiquitous in processes that involve liquid-gas interfaces, ranging from volcanic eruptions, ink-jet printing, and water-borne disease transmission [115]. In addition to their applicability in a wide range of fields, films are a convenient system to study the dynamics of fluids in a two-dimensional geometry. Newtonian bubbles have been studied in detail for several decades [7, 116–118]. For low-viscosity Newtonian soap films of constant thickness, Culick [7] derived the rupture speed of an inviscid film as $u_c = \sqrt{\frac{2\sigma}{\rho h}}$, also commonly known as the Culick velocity [see section 2.4.1 for more details]. The Culick velocity is useful to predict the rupture of a wide variety of Newtonian films.

A majority of processes involve bursting films containing surfactants, and/or made of non-Newtonian fluids. Surfactant-laden and non-Newtonian films are reported to behave in manners strikingly different from Newtonian films [115, 119–124]. Bacterial secretions act as biosurfactants and increase the lifetime of bacteria-laden films [115]. Films with surfactant concentrations beyond the crtitical micellar concentration(CMC) rupture slower than the Culick velocity, and develop ridges and mesas [119, 120], or crack-like instabilities [121] due to rigidity imparted to films by surfactants. Films and bubbles of smectic materials behave differently during rupture [122], and develop reversible instabilities under stress [125]. Viscoelastic films develop flowering instabilities at the rupture

rim [123]. In the ultrathin (Newton Black) limit, even Newtonian soap films exhibit viscoelastic properties that have been attributed to competing lengthscales of film thickness and surfactant molecules [126]. Films laden with hydrophobic particles larger than the film thickness have been reported to rupture intermittently due to the presence of particles [124]. Thus, both micelles and particulate additives alter film dynamics significantly, the effect being more dramatic in the presence of competing lengthscales. Here, we study the rupture of colloidal soap films where the film thickness (~ 5 μm) is a few times larger than the colloidal size (~ 700 nm). Although manually ruptured films seem to behave as Newtonian viscous films and rupture at a constant speed, thinner and spontaneously rupturing films develop exotic instabilities and rupture in a qualitatively different fashion.

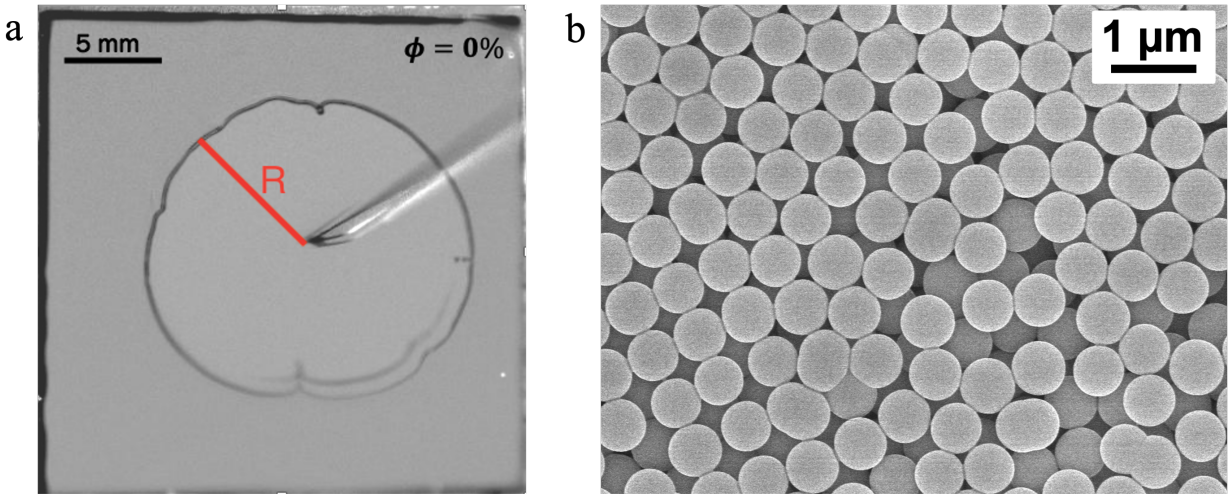

Figure 6.1: **a** Snapshot of a $\phi = 0$ film during rupture. After being ruptured with a needle, a circular hole forms and its radius, R, grows until the boundary interferes. **b** SEM image of the colloidal silica spheres. The spheres were suspended in the mixture of SDS and water to make volume fractions $0 \leq \phi \leq 0.47$, and the fluids were used to form horizontal films and record their rupture.

Experiments on film rupture commonly involve spherical bubbles formed from a

reservoir [115] or vertical films [116, 117]. However, the reservoir setup is not convenient for colloidal films, as evaporation effects are more pronounced for dense colloidal suspensions. A horizontal film geometry is useful to explore rupture dynamics of colloidal films systematically. Therefore, in our experiments, we form flat horizontal films by introducing a constant volume of fluid onto a custom film stretcher inspired by past experiments with bacterial films [127].

Here, we study the rupture of silica colloidal soap films of a range of volume fractions: $0 \leq \phi \leq 0.47$. Despite the highly non-Newtonian nature of the fluid at high ϕ [Figure 2.1], we observe colloidal films to rupture at a constant velocity. Plotted in terms of the effective viscosity of the colloidal fluid, the colloidal rupture data agrees well with the rupture of Newtonian films of similar viscosity. We show that the fluid viscosity directly affects the film thickness profile. Our results demonstrate that the effective Newtonian viscosity is a useful parameter to study colloidal film rupture, and that viscosity has a significant role in the thickness profile of constant-volume films. Additionally, we report our observation of exotic instabilities in spontaneously rupturing dense colloidal films. Instabilities occur both in the presence and absence of evaporation, but they are consistently reproducible in a humidity-controlled environment. We hypothesize that these structures are formed when the film thickness is comparable to the colloidal size. Thus, film rupture has great potential as a model system to study colloidal dynamics in two dimensions.

6.2 Experimental Methods

Colloidal synthesis

The silica colloidal spheres were synthesized following the Stöber process [93, 94].

For our spheres, we mixed tetraethyl orthosilicate with ethanol and water at room temperature and in presence of ammonia as a catalyst. We used the number of daily 'feeds' as the means to control particle diameter, such that larger the number of feeds, larger the average diameter of the silica spheres synthesized. The colloids were then washed with ethanol, separated to decrease polydispersity, and re-suspended in water. The average silica sphere diameter used for experiments reported in this chapter was 660 ± 20 nm [Fig. 6.3a]. Suspensions of volume fractions $0.00 \leq \phi \leq 0.47$ were prepared in water containing 4 mM (a concentration well below the critical micellar concentration of 8 mM) Sodium Dodecyl Sulfate (SDS), a surfactant. Thus, we do not expect SDS to affect the system in any way other than decreasing the overall surface tension. To compare colloidal rupture data to Newtonian fluid films, we perform rupture experiments on water-glycerol mixtures in the presence of 4 mM SDS, with glycerol concentrations ranging from 0% to 90% by weight. We scan over two magnitudes of fluid viscosity, while other parameters such as density and surface tension do not vary significantly with glycerol concentration ($\rho_{glycerol}/\rho_{water} = 1.25$, $\gamma_{glycerol}/\gamma_{water} = 0.92$).

Film stretcher + humidity chamber

To form horizontal films of reproducible thickness, we built a custom film stretcher inspired from Sokolov et al [128]. The stretcher is made of acrylic pieces cut using a laser cutter. On the stretcher base sit two U-shaped components, so that Component 2 fits inside Component 1 [Fig. 6.2a]. Each component has taut metal wires forming an 'X' shape. The wires criss-cross to form a small square hole. Component 1 is stationary, while Component 2 is attached to a motor and can be moved horizontally at a constant speed. A known volume of fluid can be introduced on the small square hole formed by the wires. When component 2 is pulled by a motor, the square hole expands, allowing us to form a

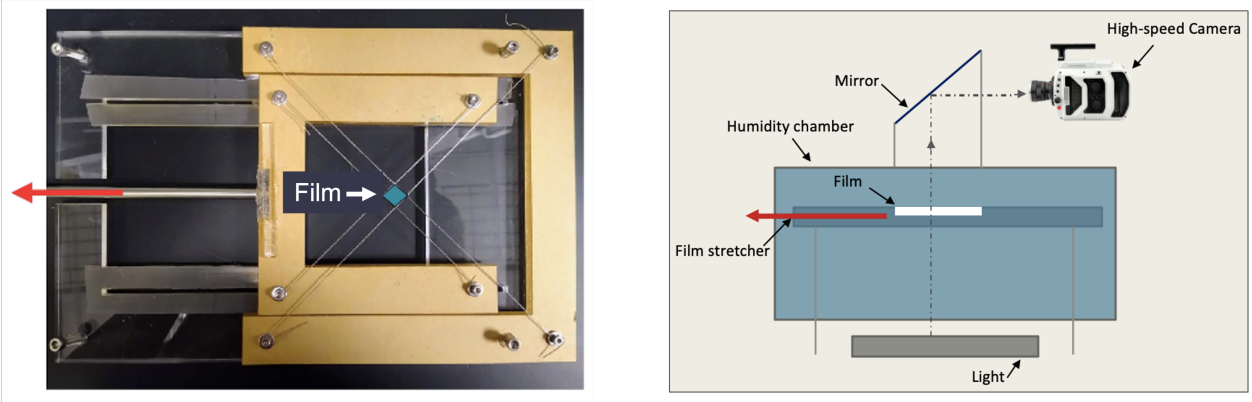

Figure 6.2: **a** Top view of the film stretcher designed to make films of desired size and reproducible thickness. A known volume of fluid is introduced between the crosswires, and then the stretcher is drawn using a motor to expand the crosswires and form a film of desired size (marked by blue). We used the fluid volumes of $10\mu l$ and $15\mu l$ in our experiments. **b** Side view of the experimental setup. The film stretcher is enclosed in a chamber that maintains relative humidity > 75% during experiments. The horizontal film is lit from below and its rupture is filmed using a high-speed camera.

horizontal square film of desired size. For all experiments reported here, Component 2 was pulled at the speed of of 0.8 mm/s. To minimize the effects of air currents, impurities, and evaporation, the film stretcher was mounted inside a custom humidity chamber and the relative humidity was maintained between 75% and 85% using a reservoir of NaCl + water solution inside the chamber [Fig. 6.2b]. The film size was 25 mm × 25 mm, and films were formed using two fluid volumes: 10 µL and 15 µL. The horizontal film was illuminated from below using a white panel light and the transmitted light data was recorded at 83,000 fps using a Phantom v2512 high-speed camera. The rupture was initiated near the center of the film using a needle. For the viscous film rupture data, we made solutions with known concentrations of glycerol and water by mass, and used a constant SDS concentration of 4 mM in all the mixtures. These Newtonian films were also formed using fluid volumes of 10 µL and 15 µL.

Interference imaging and dye absorbance measurements

In order to compare film thickness profiles for films of different fluid viscosities, I collected interference data. A green filter of wavelength 530 ± 10 nm was introduced in the path of the light from the film to the camera, and films of two different viscosities were imaged before rupture was initiated.

We also collected dye absorbance data in order to estimate the relative thickness of fluid films as a function of viscosity. I dissolved 10 g/L of Erioglaucine Disodium Salt (also known as Brilliant Blue) in the mixtures that contained varying amounts of glycerol and water, in the presence of 4 mM SDS. We imaged these dyed films under transmitted white light, using the same high-speed camera as the one used to collect the rupture velocity data.

Data analysis

Image processing and analysis were performed using ImageJ, and data was plotted using python. To measure the rupture velocity, the frame of rupture initiation was identified, and the distance from the initiation point to the rupture rim was measured for every 10th frame.

The dye absorbance images were background-normalized with the last frame of the image sequence, where the film was absent due to completion of rupture. A rectangular region, 10 pixels in height and the length of the film in width, was selected near the film center, and the line profile, averaged over the 10 pixels, was plotted. This procedure was repeated for different viscosity films.

6.3 Rupture velocity: colloidal vs. viscous Newtonian films

Rupture velocity

Figure 6.1a shows a snapshot of a soap-water film mid-rupture. When the rupture is induced in the center of the film, a circular hole forms in the film and grows radially in size. We measure the radius of this hole, R, with respect to time, t, for suspension films of increasing ϕ. In Figure 6.3a, we report this data, truncated at the point in time when the effect of film boundary destroys the circular symmetry of the rupture (when the rupture is about 80% the size of the film). Surprisingly, even at very high ϕ where the bulk colloidal suspension is known to be highly non-Newtonian, the R vs. t data follows a linear trend indicating a constant rupture velocity over time. The lines in Figure 6.3a indicate linear fits to the R vs. t data, and their slopes are the rupture velocity values. Though it remains constant throughout rupture, the rupture velocity systematically decreases with increasing ϕ for both fluid volumes [Fig. 6.3b].

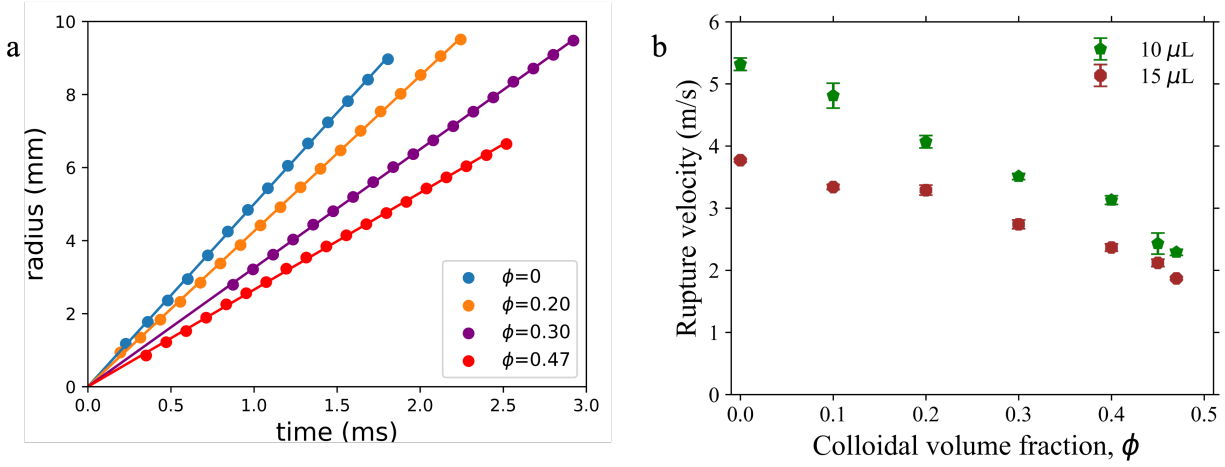

Figure 6.3: **a** Rupture radius vs. time for 15μl films made of fluids with increasing colloidal volume fraction ϕ. The rupture velocity (slope of the linear fit lines) is surprisingly constant even at ϕ where the fluid is highly non-Newtonian. **b** The film rupture velocity, plotted against ϕ for two fluid volumes, decreases with increasing ϕ.

Role of effective fluid viscosity

The observation of a constant rupture velocity, even at high ϕ, suggests that the film

rupture dynamics of the suspension may still be modeled as that of a Newtonian fluid. The well-known picture of Newtonian film rupture is that the rim at the rupture boundary collects more and more fluid as it rolls outward. In other words, the information of rupture travels at the same speed as the expanding circular rim, and does not affect the film outside the rupture. Thus, no shear is experienced by the undisturbed film. Therefore, the minimal effect of suspension shear rheology on the rupture, even at high values of ϕ, is consistent with this mechanism.

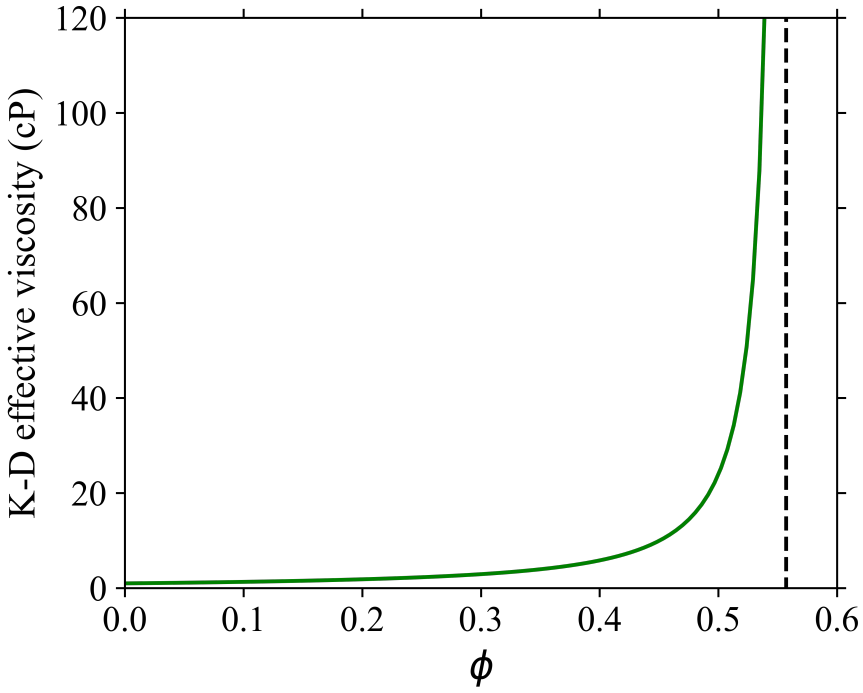

Figure 6.4: Effective viscosity of colloidal suspensions of increasing volume fractions, calculated using the Krieger-Dougherty (KD) effective viscosity model. The dashed black line indicates the value $\phi_m = 0.557$ for silica.

In addition to the non-Newtonian properties, the introduction of colloidal particles increases the effective viscosity of the fluid [1, 6]. Therefore, we computed the Krieger-Dougherty low-shear effective viscosity [Equation 2.3]. As the rupture proceeds by the

expanding rim collecting fluid, and as there is no shear flow involved, we believe the K-D low-shear viscosity [Equation 2.3] is an appropriate choice for our system. We used the literature value of value $\phi_m = 0.55$ for silica particles [101].

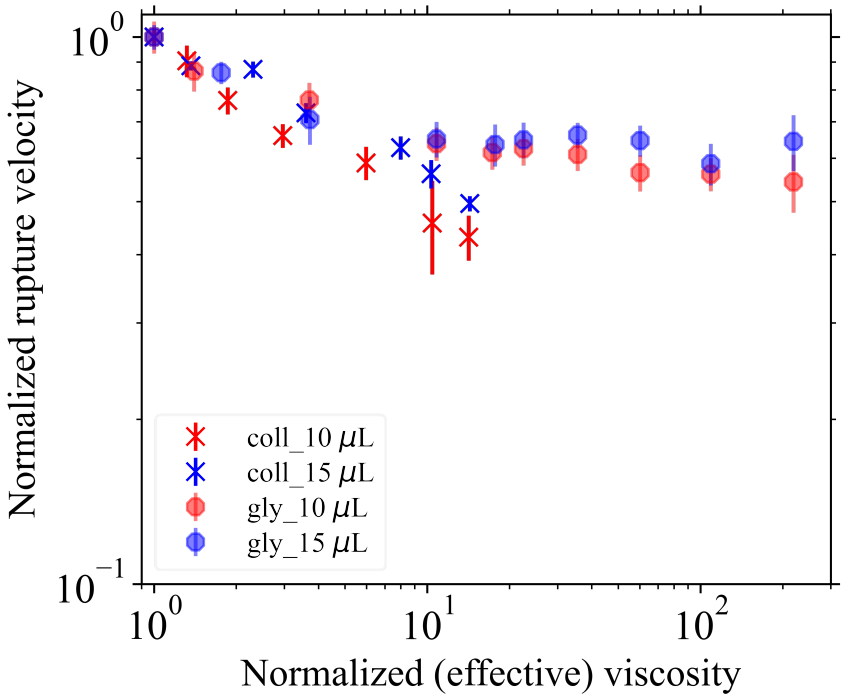

Figure 6.5: Rupture velocity of colloidal films plotted against the KD effective viscosity, along with Rupture velocity of Newtonian (glycerol-water) films plotted against fluid viscosity, for two fluid volumes. Both colloidal and Newtonian rupture seem to follow a similar decreasing trend on a log-log plot, indicating that effective viscosity is a useful framework to interpret rupture of colloidal films.

Figure 6.4a shows the viscosity as a function of ϕ computed in this manner. We plotted the film rupture velocity, normalized with respect to $\phi = 0$ (soap-water film), against this effective viscosity, and compared the colloidal rupture measurements with the rupture of viscous glycerol-water films using the same experimental setup [Figure 6.5]. Both datasets show a similar decreasing trend in normalized rupture velocity. This suggests

that effective viscosity computed in this manner is a useful framework to interpret rupture dynamics of colloidal films, over a large range of volume fractions.

Film thickness estimation

Savva et al. [8] theoretically studied the effect of fluid viscosity on rupture dynamics, and concluded that even viscous films rupture at the Culick velocity, after a brief transient of a timescale that depends on viscosity. For the experimental conditions in this study, this transient is smaller than the temporal resolution of our high-speed camera (~ 10 µs). Therefore, according to Savva et al., we should still observe rupture dynamics to follow Culick's law, and the rupture velocity of constant-thickness films should be independent of fluid viscosity. Our observations of decreasing rupture velocity [Figure 6.3b] with increasing viscosity are clearly in contradiction with this. Therefore, we attempt to estimate the film thickness as a function of fluid viscosity for Newtonian films.

The size of the square films formed in our experiments was $L_{film} = 25$ mm. Using the two fluid volumes from our experiments and assuming a perfectly flat film, simple volume conservation allows us to estimate the film thicknesses as:

$$h_{10} = \frac{10\mu\mathrm{L}}{{L_{film}}^2} = \frac{10 \times 10^{-9}\mathrm{m}^3}{(25)^2 \times 10^{-6}\mathrm{m}^2} = 16\mu\mathrm{m}, \tag{6.1}$$

and

$$h_{15} = \frac{15\mu\mathrm{L}}{{L_{film}}^2} = \frac{10 \times 10^{-9}\mathrm{m}^3}{(25)^2 \times 10^{-6}\mathrm{m}^2} = 24\mu\mathrm{m}. \tag{6.2}$$

We note that these values are upper bounds on the true film thicknesses, as it is impossible to form films of a higher average thickness due to volume conservation. A more accurate estimate of the true thickness away from film boundary can be made, at least for

low-viscosity Newtonian films, using our rupture velocity data and Culick's law:

$$h_{10,c} = \frac{2\sigma}{\rho {v_c}^2} = 3.2\mu m, \tag{6.3}$$

and

$$h_{15,c} = \frac{2\sigma}{\rho {v_c}^2} = 6.2\mu m \tag{6.4}$$

where σ is the surface tension of 4 mM SDS in water (45 mN/m), ρ is the density of water (1000 kg/m^3), and v_c is the rupture velocity from our experimental data. The thickness thus estimated is much smaller than the volume conservation estimate, supporting our hypothesis of a non-trivial film thickness profile.

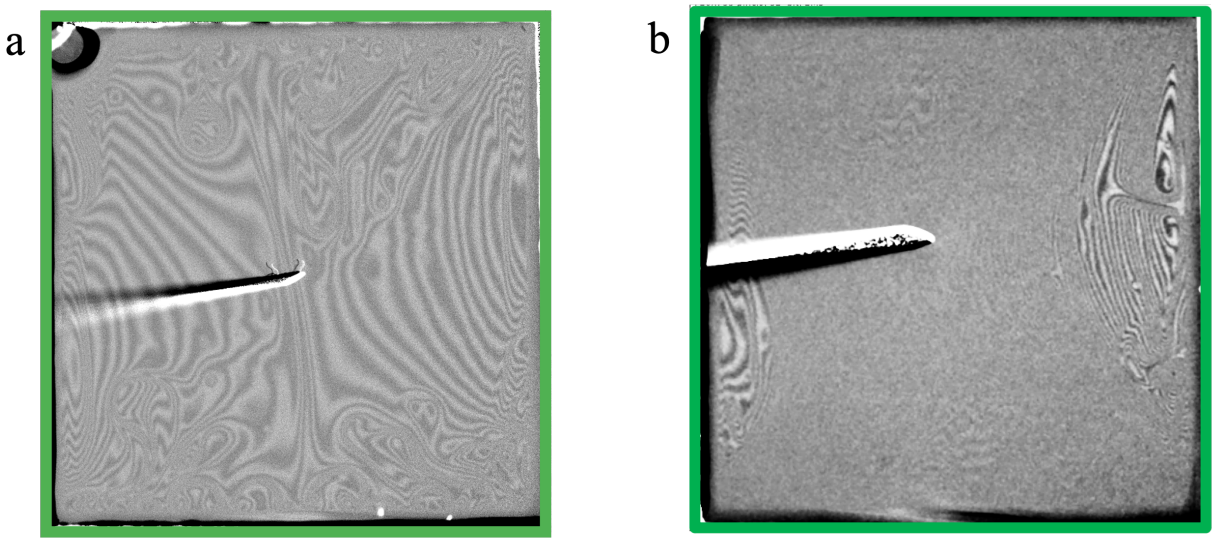

Figure 6.6: **a** Interference fringes observed under green filter for a low-viscosity film (2 cP), and **b** a higher-viscosity film (35 cP). The change in the interference pattern indicates that the thickness profile changes with fluid viscosity.

Figure 6.6 shows images of films made from the same fluid volume (15 µL), but with

fluids of different viscosities under a narrow-width bandpass filter ($\lambda = 530 \pm 10$ nm). The fluid viscosity of the film imaged in Figure 6.6a is $\eta = 2$ cP, and that showed in Figure 6.6b is $\eta = 35$ cP. While the 2 cP film shows distinctive interference fringes, fringes are largely absent for the 35 cP film, except near the film boundary. This suggests that the two films, despite being made of the same volume of fluid, have different thickness profiles. The absence of fringes in Figure 6.6b indicates that the film thickness away from the boundary is larger than the coherence length for the bandpass filter used. The coherence length can be calculated as:

$$l_{coh} = C\frac{\lambda^2}{n\Delta\lambda}, \tag{6.5}$$

where n is the refractive index of the medium, and $C = 0.44$ [129]; For $\lambda = 530$ nm and $\Delta\lambda = 10$ nm, we obtain $l_{coh} = 9.3$ µm. Thus, we infer that the higher-viscosity (35 cP) film is thicker than the low-viscosity (2 cP) film, near the film center. As thicker films rupture at lower speeds according to Culick's law, this is also consistent with the lower rupture speed we observed for viscous films.

In Figure 6.6b, we observe an interference pattern near the film edge, although fringes are absent near the middle. This additionally indicates that the film is thinner near the boundary. To characterize this film thickness profile in more detail, we collect dye absorbance data for films of varying viscosity.

Figure 6.7a and b show images of fluid films of viscosities 1 cP and 100 cP respectively, containing 10 g/L Brilliant Blue dye and imaged under white light. For dyed fluids, the absorbance gives the fraction of light absorbed by the sample, and is calculated as:

$$\text{Absorbance} = 1 - \text{normalized intensity of transmitted light.}$$

Figure 6.7c shows a plot of absorbance for both films, across a line drawn through the center of the film. In order to minimize noise, the profile averaged over a 10-pixel wide box around the line is plotted. As a thicker sample absorbs more light, the absorbance is proportional to the film thickness. Thus, the absorbance profile qualitatively captures the features of the film thickness profile. The more viscous film (orange line) shows a higher absorbance near the film center, further evidence that more viscous films lead to thicker films despite being made from a constant fluid volume.

Two other features of the absorbance profile are particularly informative. First, the absorbance increases rapidly near the film boundary, indicating a drastic increase in film thickness. This can also be observed in the Figure 6.7a and b, in the form of a darker region near the wire frame. The thickness of the wire frame (500 μm) causes this thicker meniscus at the film boundary. The second informative feature is that the absorbance reaches its minimum towards the center of the film from the meniscus, before the film assumes a relatively flat shape. The thinnest part of the film is therefore located next to the meniscus near the boundary, and not near the center of the film. Thus, the absorbance of dyed films verifies that fluid viscosity directly affects the film thickness profile. Quantifying film thickness with dye absorbance data is difficult, as making calibration samples as thin as a few microns is experimentally challenging. Nevertheless, the qualitative features of the absorbance profile allow us construct a qualitative film thickness profile.

Figure 6.8 shows a sketch of the thickness profile inferred from our interferometry and dye absorbance measurements, as seen from the side. This is a schematic, and features are exaggerated for clarity. Films have a large thickness (of the order of the wire frame thickness) near the boundary, which dramatically decreases as we move away from the boundary. The thickness reaches a minimum before rising again, and achieving a

relatively flat profile near the center. The more viscous film (blue region) is thicker in the middle, leading to a slower film rupture [Figure 6.5]. This schematic also demonstrates how the same fluid volume can cause films of different thicknesses away from the boundary. This is because the meniscus near the film edge can be made of different fluid volumes, as evidenced from the crossover point between the blue and red profiles. Thus, the area contained by the two schematic profiles is the same, corresponding to films containing the same fluid volume.

Thus, our characterization of the film thickness profile indicates that when a constant volume of fluid is used to make horizontal flat films, the film thickness profile — and in turn the film thickness away from the boundary — is directly affected by the fluid viscosity. As shown by Savva and Bush [8], Culick's law is still applicable for the rupture of viscous films. Therefore, we convert rupture velocity into film thickness: $h = \frac{2\sigma}{\rho v^2}$. Figure 6.9 shows the thickness thus calculated plotted against the fluid viscosity (for colloidal data, effective fluid viscosity) in mPa, showing an increasing trend in film thickness with viscosity. For higher viscosity glycerol data, the film thickness decreases more slowly. This is likely due to finite-volume effects, as the film thickness approaches the upper bounds calculated using volume conservation [Equations 6.1 and 6.2].

Our system shares similarities with a film clinging to a fiber pulled slowly out of a reservoir of fluid. As discussed in chapter 2.4.2, LLD theory predicts this film thickness to grow as $Ca^{2/3}$ for $Ca \ll 10^{-3}$. For the glycerol-water films considered here, $10^{-3} \leq \eta \leq 2 \times 10^{-1}$ Pa, $\sigma = 45$ mN/m, and $v = 0.8$ mm/s leads to $2 \times 10^{-5} \leq Ca \leq 4 \times 10^{-3}$, within the applicable range of the LLD approximation. Thus, the increasing thickness trend is qualitatively consistent with the Frankel's law prediction. However, it does not quantitatively agree with the $h \sim Ca^{2/3}$ relation [Equation 2.6]. This deviation may be

attributed to the finite volume of fluid we use to form films.

6.4 Instabilities in spontaneously rupturing colloidal films

In contrast to films manually ruptured away from the boundary, when constant-volume colloidal films were allowed to rupture spontaneously, we observed instabilities developing near the rupture boundary and propagating through the intact film during rupture [Figures 6.10, 6.11, see also SI videos 3,4 and 5 [107]]. Spontaneous rupture always happened near the film edge; the instabilities were almost nonexistent when similarly prepared films were manually ruptured away from the boundary. Our qualitative characterization of the film thickness profile [Figures 6.7c] suggests that film is the thinnest near the edge, between the thicker meniscus near the wire frame and the approximately flat film near the center [Figure 6.8]. Thus, spontaneous rupture always happening near the edge is consistent with the film thickness profile.

For the experiments where we observed instabilities, we formed colloidal fluid films of about 12 mm in size with 2 μL of fluid, and recorded the film until it spontaneously ruptured. We observed instabilities in experiments where humidity was not controlled for [Figure 6.10, SI videos 3 and 4 [107]], and also in controlled humidity experiments inside the humidity chamber [Figure 6.11, SI video 5 [107])].

Figure 6.10 shows films with $\phi = 0.35$ colloidal particles, where the suspending fluid is 2mM SDS in 30% glycerol and 70% water, rupturing at ambient and low humidity: RH $\sim$ 30% (see also SI videos 3 and 4 [107]). We note that these experiments were done using an earlier version of the setup where films were made using an expandable camera iris, leading to a quasi-circular film geometry. Scale bars in all panels are 5 mm. In Figure 6.10a, we observe that the rupture edge has protruding jagged structures. Addi-

tionally, the intact film develops wrinkles that crowd together as the rupture proceeds. These wrinkles are parallel to the moving rupture rim. Figure 6.10b, on the other hand, shows instabilities in the transverse direction to the rupture rim. These instabilities appear near the rim and propagate outward ahead of the rupture. We note that both these films were made of the same fluid, and yet they show drastically different patterns during rupture. Additionally, the rupture time of the two films differs by a factor of 3. This lack of reproducibility may potentially be attributed to large fluctuations in the ambient humidity, and evaporation seems to have a significant effect on film dynamics and the progression of instabilities.

In Figure 6.11 (see also SI video 5 [107]), we observe 12 mm films with $\phi = 0.40$ in 4mM SDS and water, a square geometry, rupturing under controlled humidity (RH= 80%). Once again, the rupture begins near the edge, where the film is thinnest. Instabilities are observed even after minimizing evaporation by means of a humidity chamber. We observe instabilities originating from the rupture rim and propagating. A thicker (darker) structure forms in the intact film, and the rest of the film appears to wrinkle like a fabric around this thicker filament. After rupture, we observe the filament to flow like a fluid, indicating that evaporation has not dried out the film. For humidity-controlled experiments, both the qualitative rupture behavior and the rupture time were reproducible over multiple trials.

For both humidity-controlled and uncontrolled experiments, instabilities were predominantly observed for spontaneously rupturing films. This behavior has many interesting features. In the beginning of rupture, the rupture boundary is jagged as opposed to the smooth rupture boundaries in manually ruptured films. While the rupture rim increases in size as it collects more fluid for manually ruptured films, we do not detect

such widening of the rim in the case of films where instabilities are observed. The rupture in this case looks qualitatively different: the manually induced rupture rim rolls outward smoothly, while the spontaneous rupture with instabilities is similar to an elastic sheet de-pinning from the wire frame. The instabilities are reminiscent of folds or wrinkles on a fabric. Even for controlled humidity, the significant variation in the shape of the rupture front and the location of instabilities makes quantifying their dynamics a challenge. The structures observed in experiments conducted in the ambient environment were practically impossible to reproduce, this might be a result of the significant amount of stochasticity contributed to film rupture by fluctuating humidity and ambient impurities.

We observed these instabilities only for a specific set of conditions: they occurred at high values of colloidal ϕ, and for relatively thinner films, i.e. films made of a smaller volume of fluid. Additionally, spontaneously rupturing films developed instabilities that spanned the whole size of the film, while manually ruptured films showed only a hint of these structures forming near the end stage of the rupture. We hypothesize that these structures are a result of colloidal particles self-organizing during rupture, and they develop when the colloidal size competes with the film thickness. The colloidal spheres we use are 660 nm in diameter, and the film thickness is a few microns. We believe this competition between lengthscales is why instabilities were observed for thinner films.

Fluid films spontaneously rupture at this thinnest point, and our films are thinnest near their edges [Figure 6.7c]. This is possibly why instabilities develop predominantly in spontaneously rupturing films. Additionally, for these experiments, we waited for the film to rupture spontaneously after forming it. Over this waiting time, the film could have thinned even more, making the occurrence of these structures even more likely.

For spontaneous rupture under controlled humidity, the rupture time was more or less constant over trials. Although the nontrivial geometry of the rupturing film makes it impossible to measure the rupture speed, we can make an estimate of the rupture speed using the film size (12 mm) and time of rupture (7 ms), $v_{rupture} = 1.71$ m/s. According to Culick's law, this rupture speed corresponds to a 22 μm film. This is above the upper bound of thickness we can obtain using volume conservation, $h = \frac{2\mu L}{144mm^2} = 13\mu L$. Therefore, instabilities significantly slow down rupture below the Culick velocity. In the past, such a slowing down has been attributed to film elasticity. A deeper investigation into the cause of these modified film dynamics would help learn more about colloidal dynamics in a film geometry.

In the future, more systematic work to explore these instabilities would be useful. There are two possible ways to more reliably access the regimes where the colloidal lengthscale competes with the film thickness. The experiments we report here are for colloidal sphere size of 660 nm; the occurrence of instabilities in colloidal suspensions made of larger particles should be explored. Forming these films in a vertical geometry might also be helpful, as drainage due to gravity will encourage the film to thin near the top, and encourage reproducible rupture and instabilities. A circular geometry seems to cause a more regular rupture geometry as opposed to a square film [Figure 6.10 as compared to Figure 6.11]; this might help in collecting more systematic data on these structures. Both these lines of investigation have potential to verify or refute our hypothesis that these instabilities result from the competition between particle size and film thickness lengthscale.

6.5 Discussion

Here, we report the rupture velocity data of flat colloidal films in the range of volume fractions $0 \leq \phi \leq 0.47$, and of glycerol-water films with viscosities 1-200 cP ($2 \times 10^{-5} \leq Ca \leq 4{\times}10^{-3}$). We use a custom film stretcher to make films of two constant fluid volumes, 10 µL and 15 µL. We observe constant rupture velocity even at high colloidal ϕ which, when plotted against the effective viscosity of suspensions, agrees well with that of Newtonian glycerol-water films in the same viscosity range. Therefore, even at high ϕ where highly non-Newtonian behavior is apparent from bulk rheology, effective suspension viscosity captures film rupture dynamics of colloidal suspensions. As the well-accepted picture of Newtonian film rupture is that the rupture rolls outward collecting fluid, high shear must not be present in the film during rupture, despite the short timescale of rupture. Our results demonstrate that rupturing particulate films can be effectively modeled as viscous fluids useful for a variety of industrial processes.

For both colloidal and Newtonian fluids, we observed the rupture velocity of constant-volume films decrease with increasing fluid (effective) viscosity. Our characterization of the film thickness profile via interference imaging and dye absorption shows that higher viscosity films lead to higher thickness near the film center, as viscosity modifies the overall thickness profile. This increase is consistent with the predictions of LLD theory in the visco-capillary regime [4, 116]. Although the LLD approximation theoretically holds for $Ca \leq 10{-}3$, experiments have reported deviation for this law for Capillary numbers as low as 10^{-4} [9]. Additionally, a quantitative comparison of our results with the LLD prediction cannot be made due to differences in experimental geometry and boundary conditions in our system.

Although Culick's derivation neglected viscous effects, Culick's law has been shown to asymptotically hold for high-viscosity fluids. Viscosity is only expected to introduce a transient at the initial stage of rupture, on a timescale $t_{vis} = \frac{\eta H}{2\sigma}$. For our experiments, $0.1\mu s \leq \tau_{vis} \leq 20\mu s$, which cannot be observed at the temporal resolution of our experiments ($\sim 12\mu s$). Thus, the change in the thickness profile is solely responsible for the slower rupture of more viscous films. A surprising feature of the horizontal film thickness profile is that the film reaches a minimum thickness near the thicker meniscus by the wire frame, away from the film center. The reason for this highly non-trivial film shape needs to be studied carefully in the future.

When we allowed flat colloidal films at $\phi \geq 0.40$ to rupture spontaneously, we observed exotic instabilities originating at the rupture rim and propagating through the film surface. Films always rupture spontaneously near the edge, as films have a thickness minimum near the edge that increase the probability of rupture. Both the pattern of instabilities and the rupture time were highly reproducible under controlled and high humidity, while they were much more stochastic when humidity was not controlled for. We hypothesize that these structures are a result of colloidal particles assembling when the colloidal size competes with the film thickness. Other studies have reported instabilities in surfactant films of varying thicknesses above the critical micellar concentration, which have been attributed to the rigidity imparted to the film [121] and to micelles forming mesa-like structures [119, 120]. Some work has also focused on particulate rafts with > 100 µm particles, so that the raft is made of small capillary bridges between these particles [124]. However, there are no other works that have considered colloidal-size particles in films that are less than an order of magnitude thicker than the particle, to the best of our knowledge. Film rupture in this parameter regime is a very convenient

way to study the physics of suspensions in two dimensions, and has the potential to uncover the mechanism of colloidal self-assembly in quasi-2D systems. Instabilities seem to slow down film rupture significantly as compared to the Culick prediction, and rupturing films are reminiscent of wrinkling fabrics. The characterization of this state of the film before it re-fluidizes after rupture would be a fascinating avenue of future exploration.

Our experiments on colloidal film rupture extend understanding of film rupture dynamics to non-Newtonian films. Although colloidal film dynamics are surprisingly Newtonian when films are significantly thicker than particle size, exotic structures are observed in spontaneous rupturing films when the thickness and particle size compete. Further theoretical work aimed towards understanding these discrete effects on the particle scale would greatly enhance our understanding of colloidal self-assembly in two dimensions. We anticipate that our work will guide future applications that necessitate a controlled use of fluid films in a variety of applications.

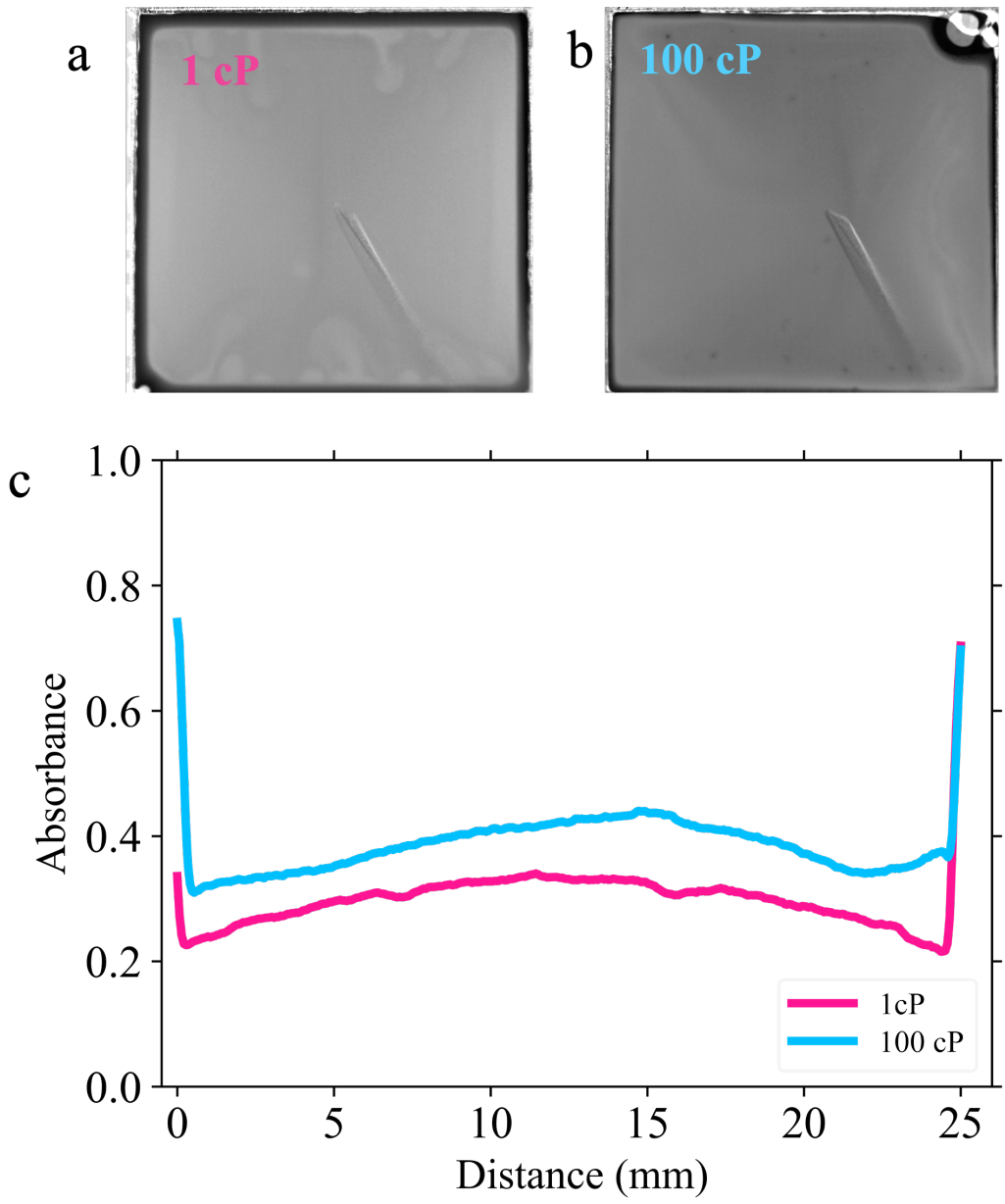

Figure 6.7: 15 µL Newtonian films of viscosities **a** 1 cP and **b** 100 cP, containing Brilliant Blue dye. The films transmit different amounts of light, indicating a different film thickness. **c** Absorbance of both the films plotted along a line going through the center of the film. Higher absorbance indicates higher film thickness, thus the film thickness profile is proportional to the absorbance profile.

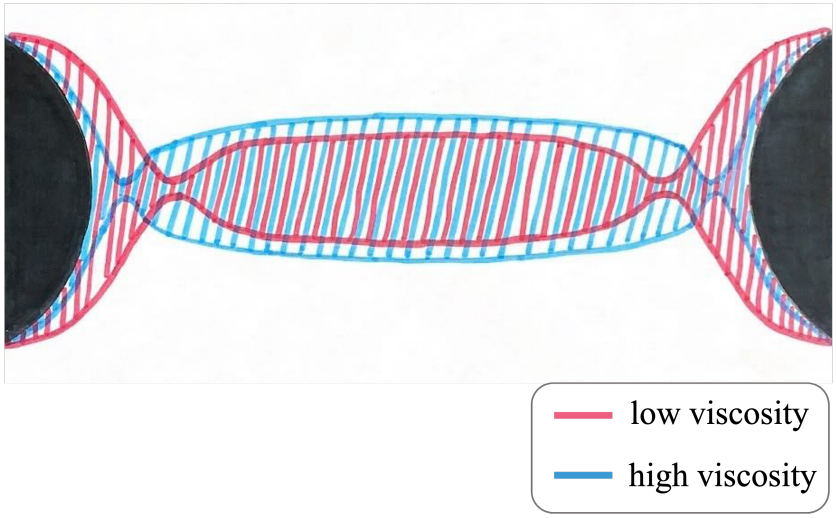

Figure 6.8: Schematic showing the variation in thickness profile with increasing viscosity. The red shaded area indicates a lower-viscosity film, and the blue indicates a higher viscosity film made of the same fluid volume. The length of the meniscus near the film edge is smaller for a more viscous film, and so is the location where film thickness is minimum. Away from the boundary, both films assume a flat, practically constant-thickness shape, with the viscous fluid forming a thicker film.

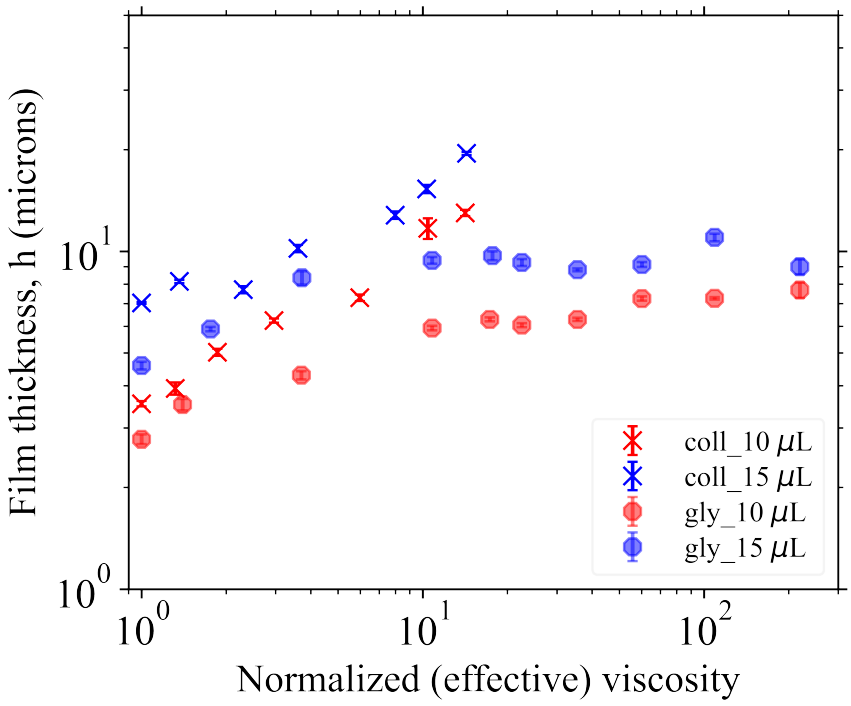

Figure 6.9: Film thickness, calculated using Culick's law, plotted for both Newtonian and colloidal films. For both viscous and colloidal fluids, the film thickness increases with increasing fluid viscosity, consistent with the interferometry and dye absorbance observations.

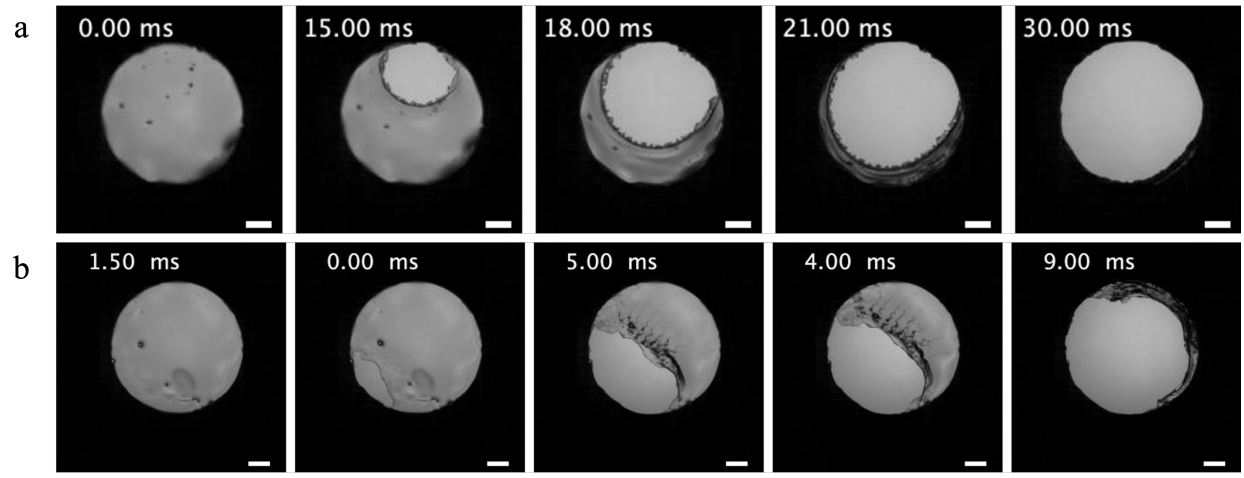

Figure 6.10: Instabilities develop in spontaneously rupturing colloidal films at low humidity (see also SI videos 3 and 4 [107]). The film composition is $\phi = 0.35$ colloidal particles, where the suspending fluid is 2mM SDS in 30% glycerol and 70% water. In uncontrolled humidity, instabilities are not reproducible. Scale bars are 2 mm.

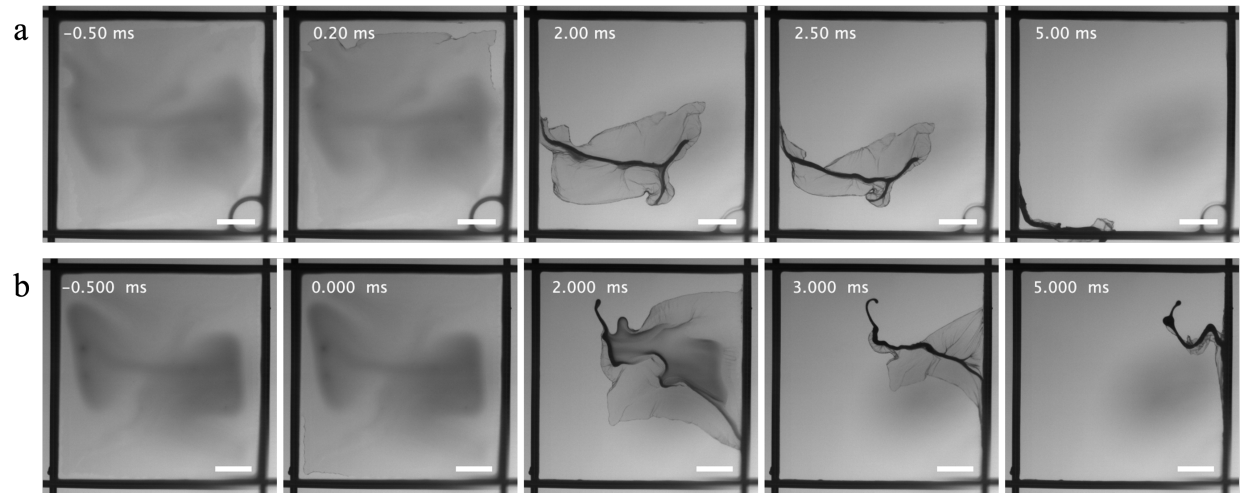

Figure 6.11: Instabilities also develop in spontaneously rupturing colloidal films at high humidity (see also SI video 5 [107]). The film was made of fluid with $\phi = 0.40$ colloids in 4mM SDS and water. In a humidity-controlled environment, instabilities are much more reproducible. Scale bars are 2 mm for all panels.

CHAPTER 7
CONCLUSION

In this dissertation, I summarized my work on the dynamics of colloidal suspensions in two systems: drop impact and film rupture. For both systems, I used micron-sized colloidal particles suspended in water, over a large range of ϕ. While the drop impact system has a low surface area due to the spherical drop geometry, the film rupture system has a very high surface area to volume ratio. A unifying feature of both these systems is the presence of a freely deformable surface, which allows us to observe fluid behavior under dynamic conditions. Both systems exhibited surprisingly Newtonian behavior for ϕ values well into the shear thinning regime. This information is key to applying models developed for Newtonian fluid systems to a range of colloidal suspensions used in industrial processes. At very high values of ϕ, however, both systems showed exotic behaviors: impacting drops partially or fully solidified due to the high shear, while spontaneously rupturing films showed novel instabilities reminiscent of a wrinkling fabric.

After providing background and outlining key concepts in chapters 1 and 2, I summarized relevant results in the drop impact literature in chapter 3. In chapter 4, I outlined my findings about impacting colloidal drops on a hydrophilic substrate. I observe a striking transition from Newtonian-like to complete shear jamming via partially solidified states. I characterize this solidification in detail, and show that shear travels up from the impact point at a speed faster than the impact velocity. This speed depends on how deep into the shear thickening regime the applied shear is. Shear thickening is considered a precursor to shear jamming, but little is understood of the transition between one and the

other. The fact that we can characterize drop solidification via the shear thickening transition suggests that shear thickening and shear jamming are intimately connected. Our drop impact system has the unique ability to apply a high instantaneous shear, enabling us to access such solidification behaviors that cannot be observed in typical rheometry techniques.

The shear jammed drop completely rebounded at one impact condition, enabling us to measure the contact time and estimate the elastic modulus of the material. Even in absence of rebound, an estimate of the elastic modulus can be made by assuming a linear spring-mass system. I discuss this calculation in section 5.1. Modeling the system as a linear spring is a useful first approximation to infer the effect of shear jamming on the droplet. The elastic modulus seems to increase with increasing instantaneous shear rate; this gives important insights into the nature of shear jammed materials. This is very relevant to applications involving shear thickening materials, such as body armours and soft robots. In order to access drop rebound at multiple impact conditions, impact experiments performed on hydrophobic surfaces would be useful in the future.

In section 5.2, I reported the long-term unjamming dynamics of impacting sphere suspension drops. Although shear jamming is reversible, unjamming dynamics seem to depend on the shear history of the suspension drop. While I observed unjamming over a few seconds on hydrophilic substrates, on hydrophobic substrates dense suspensions have been reported to stay jammed for hours [52]. Therefore, substrate wettability likely has an effect on unjamming. Studying the effects of shear history on the bulk of the drop and those of substrate wetting on unjamming in a decoupled way is important. In the future, local measurements inside the drop and experiments on hydrophobic substrates will provide key insights into the role of the substrate on the shear jamming transition.

I also conducted experiments on the impact dynamics of suspensions with rod-shaped particles, reported in section 5.3. I observed droplets made of rod-shaped particle suspensions to shear jam at much lower ϕ and over a wider range of ϕ than suspensions with spherical colloids. This is consistent with rheological measurements on anisotropic particle suspensions [101]. More surprisingly, I observe completely shear jammed suspension droplets trying to rebound after impact, but unlike sphere suspension drops, these droplets are unable to detach from the substrate. Why the droplet adheres to the substrate so strongly as compared to sphere suspensions is an interesting question, especially given that the surface tension of the suspension is practically the same for both sphere and rod suspensions. For impacting polymer droplets, dissipation at the contact line has been reported to prevent bounce. One can qualitatively consider polymeric chains as extremely high aspect-ratio particulate additives. Whether these observations indicate that droplet adhesion to the substrate is a systematic function of additive aspect ratio is a pertinent question. More detailed work building upon this hypothesis could aid in uniting drop impact observations of particulate and polymeric fluids, and form a strong foundation for complex fluid drop impact. Another possibility is the shear alignment of rod-shaped particles over either the surface or the entire bulk of the drop. This needs to be investigated experimentally by observations under polarized light, as it will clue us into any liquid crystal formation as a response to instantaneous shear.

In chapter 6, I showed that the rupture velocity of colloidal films can be modeled as that of viscous fluid films, even well into the non-Newtonian regime. Additionally, for high ϕ and thinner films, I observed novel instabilities. Studying such structures in rupturing films would help us study the self-assembly of particulate additives in a quasi-2D geometry. Microscopic imaging of these instabilities would be highly informative. Ad-

ditionally, exploring particle shape in film rupture could generate insights on particle alignment in two dimensions, and might connect with how anisotropic suspensions behave along interfaces. My preliminary results indicate that the presence of instabilities slows down the rupture significantly. Altered rupture speed has been reported in the presence of both surfactants [121] and particulate additives [124], and this modification has been attributed to either film rigidity or elasticity. The causal connection between the overall film properties and the localized structure formation observed in my experiments needs to be investigated closely.

Due to the wide parameter range explored here, my work bridges the gap between Newtonian and particulate systems, and also captures exotic behaviors in the dense limit. While a dense suspension drop shows novel solidification behaviors as a direct result of shear jamming, instabilities in rupturing films are likely a result of colloidal particles being affected by film hydrodynamics and confinement on the lengthscale of particle size. Film rupture is a potentially very interesting system to study dense suspension flow in a quasi-2D geometry.

For the systems discussed in this dissertation, the presence of a deformable surface gives rise to interesting phenomena that connect fluid behavior under highly dynamic conditions with the bulk fluid properties. Uncovering the mechanisms on the particulate scale that cause these macroscopic behaviors is a worthwhile pursuit for future experiments. Temporally resolved, macroscopic measurements such as the ones I report here should be coupled with spatially resolved, localized observations using techniques such as boundary stress measurements and particle image velocimetry. Although experimentally challenging, such measurements have a great potential to generate physical insights on the microscopic level, that will inform constitutive models for the bulk behavior of

dense colloidal suspensions. I hope this dissertation provides a useful starting point for investigations on these lines, leading to insights into fundamental questions such as the nature of the jamming transition, as well as developing ways to control complex fluid behavior in a variety of applications.

REFERENCES

[1] J. Mewis and N. J. Wagner, *Colloidal suspension rheology*. Cambridge University Press, 2012 (cit. on pp. 19, 21, 34, 90).

[2] M. M. Denn, J. F. Morris, and D. Bonn, "Shear thickening in concentrated suspensions of smooth spheres in newtonian suspending fluids," *Soft Matter*, vol. 14, pp. 170–184, 2 2018 (cit. on pp. 19, 34, 46).

[3] J. J. Stickel and R. L. Powell, "Fluid mechanics and rheology of dense suspensions," *Annual Review of Fluid Mechanics*, vol. 37, no. 1, pp. 129–149, 2005 (cit. on pp. 19, 43, 46).

[4] P.-G. De Gennes, F. Brochard-Wyart, D. Quéré, *et al.*, *Capillarity and wetting phenomena: drops, bubbles, pearls, waves*. Springer, 2004, vol. 315 (cit. on pp. 19, 24, 101).

[5] M. Wyart and M. E. Cates, "Discontinuous shear thickening without inertia in dense non-brownian suspensions," *Phys. Rev. Lett.*, vol. 112, p. 098 302, 9 2014 (cit. on p. 21).

[6] I. M. Krieger and T. J. Dougherty, "A mechanism for non-newtonian flow in suspensions of rigid spheres," *Transactions of the Society of Rheology*, vol. 3, no. 1, pp. 137–152, 1959 (cit. on pp. 21, 34, 90).

[7] F. E. Culick, "Comments on a ruptured soap film," *Journal of applied physics*, vol. 31, no. 6, pp. 1128–1129, 1960 (cit. on pp. 23, 83).

[8] N. SAVVA and J. W. M. BUSH, "Viscous sheet retraction," *Journal of Fluid Mechanics*, vol. 626, 211–240, 2009 (cit. on pp. 24, 92, 96).

[9] L. Champougny, B. Scheid, F. Restagno, J. Vermant, and E. Rio, "Surfactant-induced rigidity of interfaces: A unified approach to free and dip-coated films," *Soft matter*, vol. 11, no. 14, pp. 2758–2770, 2015 (cit. on pp. 25, 101).

[10] A. Yarin, "Drop impact dynamics: Splashing, spreading, receding, bouncing…," *Annual Review of Fluid Mechanics*, vol. 38, no. 1, pp. 159–192, 2006 (cit. on pp. 26, 28).

[11] C. Josserand and S. Thoroddsen, "Drop impact on a solid surface," *Annual Review of Fluid Mechanics*, vol. 48, no. 1, pp. 365–391, 2016 (cit. on pp. 26, 28, 138).

[12] C. Josserand and S. T. Thoroddsen, "Drop impact on a solid surface," *Annual review of fluid mechanics*, vol. 48, pp. 365–391, 2016 (cit. on pp. 27–29, 43, 51, 52, 154).

[13] D. Richard, C. Clanet, and D. Quéré, "Contact time of a bouncing drop," *Nature*, vol. 417, no. 6891, pp. 811–811, 2002 (cit. on pp. 27, 28, 60).

[14] N. Laan, K. G. de Bruin, D. Bartolo, C. Josserand, and D. Bonn, "Maximum diameter of impacting liquid droplets," *Physical Review Applied*, vol. 2, no. 4, p. 044 018, 2014 (cit. on pp. 28, 31, 34, 43, 50–52, 138, 141–143, 153).

[15] J. Lee *et al.*, "Universal rescaling of drop impact on smooth and rough surfaces," *Journal of Fluid Mechanics*, vol. 786, 2016 (cit. on pp. 28, 138, 141, 142, 144, 146–148).

[16] D. Bartolo, C. Josserand, and D. Bonn, "Retraction dynamics of aqueous drops upon impact on non-wetting surfaces," *Journal of Fluid Mechanics*, vol. 545, pp. 329–338, 2005 (cit. on pp. 28, 30).

[17] J. C. Bird, R. Dhiman, H.-M. Kwon, and K. K. Varanasi, "Reducing the contact time of a bouncing drop," *Nature*, vol. 503, no. 7476, pp. 385–388, 2013 (cit. on pp. 28, 30).

[18] G. Riboux and J. M. Gordillo, "Experiments of drops impacting a smooth solid surface: A model of the critical impact speed for drop splashing," *Phys. Rev. Lett.*, vol. 113, p. 024 507, 2 2014 (cit. on pp. 28, 31, 36).

[19] B. L. Scheller and D. W. Bousfield, "Newtonian drop impact with a solid surface," *AIChE Journal*, vol. 41, no. 6, pp. 1357–1367, 1995 (cit. on pp. 28, 52, 138, 140, 145, 153).

[20] J. B. Lee *et al.*, "Universal rescaling of drop impact on smooth and rough surfaces," *Journal of Fluid Mechanics*, vol. 786, R4, 2016 (cit. on pp. 29, 43, 52, 154).

[21] J. Du, Y. Zhang, and Q. Min, "Numerical investigations of the spreading and retraction dynamics of viscous droplets impact on solid surfaces," *Colloids and Surfaces A: Physicochemical and Engineering Aspects*, vol. 609, p. 125 649, 2021 (cit. on p. 30).

[22] F. Wang and T. Fang, "Retraction dynamics of water droplets after impacting upon solid surfaces from hydrophilic to superhydrophobic," *Physical Review Fluids*, vol. 5, no. 3, p. 033 604, 2020 (cit. on p. 30).

[23] S. Arora, J.-M. Fromental, S. Mora, T. Phou, L. Ramos, and C. Ligoure, "Impact of beads and drops on a repellent solid surface: A unified description," *Physical Review Letters*, vol. 120, no. 14, p. 148 003, 2018 (cit. on pp. 30, 35).

[24] C. Vernay, L. Ramos, and C. Ligoure, "Free radially expanding liquid sheet in air: Time- and space-resolved measurement of the thickness field," *Journal of Fluid Mechanics*, vol. 764, 428–444, 2015 (cit. on pp. 30, 35).

[25] A. Rozhkov, B. Prunet-Foch, and M. Vignes-Adler, "Impact of water drops on small targets," *Physics of Fluids*, vol. 14, no. 10, pp. 3485–3501, 2002 (cit. on pp. 30, 35).

[26] D. Richard, C. Clanet, and D. Quéré, "Contact time of a bouncing drop," *Nature*, vol. 417, no. 6891, pp. 811–811, 2002 (cit. on p. 30).

[27] A. Jha, P. Chantelot, C. Clanet, and D. Quéré, "Viscous bouncing," *Soft Matter*, vol. 16, no. 31, pp. 7270–7273, 2020 (cit. on p. 30).

[28] D. Khojasteh, M. Kazerooni, S. Salarian, and R. Kamali, "Droplet impact on superhydrophobic surfaces: A review of recent developments," *Journal of Industrial and Engineering Chemistry*, vol. 42, pp. 1–14, 2016 (cit. on p. 30).

[29] C. D. Stow and M. G. Hadfield, "An experimental investigation of fluid flow resulting from the impact of a water drop with an unyielding dry surface," *Proceedings of the Royal Society of London. A. Mathematical and Physical Sciences*, vol. 373, no. 1755, pp. 419–441, 1981 (cit. on p. 30).

[30] C. Mundo, M. Sommerfeld, and C. Tropea, "Droplet-wall collisions: Experimental studies of the deformation and breakup process," *International Journal of Multiphase Flow*, vol. 21, no. 2, pp. 151 –173, 1995 (cit. on p. 30).

[31] K. Range and F. Feuillebois, "Influence of surface roughness on liquid drop impact," *Journal of Colloid and Interface Science*, vol. 203, no. 1, pp. 16 –30, 1998 (cit. on p. 31).

[32] L. Xu, W. W. Zhang, and S. R. Nagel, "Drop splashing on a dry smooth surface," *Physical review letters*, vol. 94, no. 18, p. 184 505, 2005 (cit. on p. 31).

[33] J. H. Snoeijer and B. Andreotti, "Moving contact lines: Scales, regimes, and dynamical transitions," *Annual review of fluid mechanics*, vol. 45, 2013 (cit. on p. 31).

[34] A. Latka, A. M. Boelens, S. R. Nagel, and J. J. de Pablo, "Drop splashing is independent of substrate wetting," *Physics of Fluids*, vol. 30, no. 2, p. 022 105, 2018 (cit. on p. 31).

[35] M. A. Quetzeri-Santiago, K. Yokoi, A. A. Castrejón-Pita, and J. R. Castrejón-Pita, "Role of the dynamic contact angle on splashing," *Phys. Rev. Lett.*, vol. 122, p. 228 001, 22 2019 (cit. on p. 31).

[36] G. Riboux and J. M. Gordillo, "Boundary-layer effects in droplet splashing," *Phys. Rev. E*, vol. 96, p. 013 105, 1 2017 (cit. on p. 31).

[37] T. C. de Goede, N. Laan, K. G. de Bruin, and D. Bonn, "Effect of wetting on drop splashing of newtonian fluids and blood," *Langmuir*, vol. 34, no. 18, pp. 5163–5168, 2018 (cit. on pp. 31, 36).

[38] A. Latka, A. M. P. Boelens, S. R. Nagel, and J. J. de Pablo, "Drop splashing is independent of substrate wetting," *Physics of Fluids*, vol. 30, no. 2, p. 022 105, 2018 (cit. on p. 31).

[39] Z. Jian, C. Josserand, S. Popinet, P. Ray, and S. Zaleski, "Two mechanisms of droplet splashing on a solid substrate," *Journal of Fluid Mechanics*, vol. 835, pp. 1065–1086, 2018 (cit. on p. 31).

[40] J. M. Kolinski, R. Kaviani, D. Hade, and S. M. Rubinstein, "Surfing the capillary wave: Wetting dynamics beneath an impacting drop," *Phys. Rev. Fluids*, vol. 4, p. 123 605, 12 2019 (cit. on p. 31).

[41] S. T. THORODDSEN, T. G. ETOH, and K. TAKEHARA, "Air entrapment under an impacting drop," *Journal of Fluid Mechanics*, vol. 478, 125–134, 2003 (cit. on p. 31).

[42] M. M. Driscoll and S. R. Nagel, "Ultrafast interference imaging of air in splashing dynamics," *Phys. Rev. Lett.*, vol. 107, p. 154 502, 15 2011 (cit. on p. 31).

[43] Y. Liu, P. Tan, and L. Xu, "Kelvin–helmholtz instability in an ultrathin air film causes drop splashing on smooth surfaces," *Proceedings of the National Academy of Sciences*, vol. 112, no. 11, pp. 3280–3284, 2015 (cit. on p. 31).

[44] R. C. A. van der Veen, T. Tran, D. Lohse, and C. Sun, "Direct measurements of air layer profiles under impacting droplets using high-speed color interferometry," *Phys. Rev. E*, vol. 85, p. 026 315, 2 2012 (cit. on p. 31).

[45] J. C. Bird, S. S. Tsai, and H. A. Stone, "Inclined to splash: Triggering and inhibiting a splash with tangential velocity," *New Journal of Physics*, vol. 11, no. 6, p. 063 017, 2009 (cit. on p. 31).

[46] J. Hao, J. Lu, L. Lee, Z. Wu, G. Hu, and J. Floryan, "Droplet splashing on an inclined surface," *Physical review letters*, vol. 122, no. 5, p. 054 501, 2019 (cit. on p. 31).

[47] P. García-Geijo, G. Riboux, and J. M. Gordillo, "Inclined impact of drops," *Journal of Fluid Mechanics*, vol. 897, 2020 (cit. on p. 31).

[48] R. E. Pepper, L. Courbin, and H. A. Stone, "Splashing on elastic membranes: The importance of early-time dynamics," *Physics of Fluids*, vol. 20, no. 8, p. 082 103, 2008 (cit. on p. 31).

[49] C. J. Howland *et al.*, "It's harder to splash on soft solids," *Phys. Rev. Lett.*, vol. 117, p. 184 502, 18 2016 (cit. on p. 31).

[50] I. R. Peters, Q. Xu, and H. M. Jaeger, "Splashing onset in dense suspension droplets," *Physical review letters*, vol. 111, no. 2, p. 028 301, 2013 (cit. on pp. 33, 44).

[51] F. Boyer, E. Sandoval-Nava, J. H. Snoeijer, J. F. Dijksman, and D. Lohse, "Drop impact of shear thickening liquids," *Physical review fluids*, vol. 1, no. 1, p. 013 901, 2016 (cit. on pp. 33, 44, 50, 53).

[52] V. Bertola and M. D. Haw, "Impact of concentrated colloidal suspension drops on solid surfaces," *Powder Technology*, vol. 270, pp. 412–417, 2015 (cit. on pp. 33, 36, 44, 50, 51, 75, 109).

[53] J. O. Marston, M. M. Mansoor, and S. T. Thoroddsen, "Impact of granular drops," *Phys. Rev. E*, vol. 88, p. 010 201, 1 2013 (cit. on pp. 34, 40).

[54] M. Guémas, A. G. Marín, and D. Lohse, "Drop impact experiments of non-newtonian liquids on micro-structured surfaces," *Soft Matter*, vol. 8, pp. 10 725–10 731, 41 2012 (cit. on p. 34).

[55] G German and V Bertola, "Impact of shear-thinning and yield-stress drops on solid substrates," *Journal of Physics: Condensed Matter*, vol. 21, no. 37, p. 375 111, 2009 (cit. on p. 34).

[56] P. Shah, S. Arora, and M. M. Driscoll, "Coexistence of solid and liquid phases in shear jammed colloidal drops," 2021 (cit. on pp. 34, 36, 37).

[57] L. Jørgensen, Y. Forterre, and H. Lhuissier, *Deformation upon impact of a concentrated suspension drop*, 2020 (cit. on pp. 34, 35, 39, 44).

[58] H. Ok, H. Park, W. W. Carr, J. F. Morris, and J. Zhu, "Particle-laden drop impacting on solid surfaces," *Journal of Dispersion Science and Technology*, vol. 25, no. 4, pp. 449–456, 2005 (cit. on p. 34).

[59] M. NICOLAS, "Spreading of a drop of neutrally buoyant suspension," *Journal of Fluid Mechanics*, vol. 545, 271–280, 2005 (cit. on pp. 34, 35, 41).

[60] F. m. c. Boyer, E. Sandoval-Nava, J. H. Snoeijer, J. F. Dijksman, and D. Lohse, "Drop impact of shear thickening liquids," *Phys. Rev. Fluids*, vol. 1, p. 013 901, 1 2016 (cit. on pp. 34, 36).

[61] P. S. Raux, A. Troger, P. Jop, and A. Sauret, "Spreading and fragmentation of particle-laden liquid sheets," *Phys. Rev. Fluids*, vol. 5, p. 044 004, 4 2020 (cit. on pp. 34, 35).

[62] V. Grishaev, C. S. Iorio, F. Dubois, and A. Amirfazli, "Complex drop impact morphology," *Langmuir*, vol. 31, no. 36, pp. 9833–9844, 2015, PMID: 26274810 (cit. on pp. 34, 40, 41).

[63] ——, "Impact of particle-laden drops: Particle distribution on the substrate," *Journal of Colloid and Interface Science*, vol. 490, pp. 108–118, 2017 (cit. on pp. 34, 35).

[64] B. L. Scheller and D. W. Bousfield, "Newtonian drop impact with a solid surface," *AIChE Journal*, vol. 41, no. 6, pp. 1357–1367, 1995 (cit. on p. 34).

[65] A. Rozhkov, B. Prunet-Foch, and M. Vignes-Adler, "Impact of drops of polymer solutions on small targets," *Physics of Fluids*, vol. 15, no. 7, pp. 2006–2019, 2003 (cit. on p. 36).

[66] V. Bertola and M. D. Haw, "Impact of concentrated colloidal suspension drops on solid surfaces," *Powder Technology*, vol. 270, pp. 412 –417, 2015, 6th International Workshop on Granulation: Granulation across the length scales (cit. on p. 37).

[67] G. Kim, W. Kim, S. Lee, and S. Jeon, "Impact dynamics of a polystyrene suspension droplet on nonwetting surfaces measured using a quartz crystal microresonator and a high-speed camera," *Sensors and Actuators B: Chemical*, vol. 288, pp. 716–720, 2019 (cit. on p. 37).

[68] S. R. Waitukaitis and H. M. Jaeger, "Impact-activated solidification of dense suspensions via dynamic jamming fronts," *Nature*, vol. 487, no. 7406, pp. 205–209, 2012 (cit. on pp. 37, 38, 59).

[69] E. Han, I. R. Peters, and H. M. Jaeger, "High-speed ultrasound imaging in dense suspensions reveals impact-activated solidification due to dynamic shear jamming," *Nature communications*, vol. 7, no. 1, pp. 1–8, 2016 (cit. on pp. 37, 38, 59).

[70] I. R. Peters, S. Majumdar, and H. M. Jaeger, "Direct observation of dynamic shear jamming in dense suspensions," *Nature*, vol. 532, no. 7598, pp. 214–217, 2016 (cit. on pp. 37, 38, 59).

[71] E. Han, M. Wyart, I. R. Peters, and H. M. Jaeger, "Shear fronts in shear-thickening suspensions," *Phys. Rev. Fluids*, vol. 3, p. 073 301, 7 2018 (cit. on pp. 37, 38, 59).

[72] O. Rømcke, I. R. Peters, and R. J. Hearst, "Getting jammed in all directions: Dynamic shear jamming around a cylinder towed through a dense suspension," *Phys. Rev. Fluids*, vol. 6, p. 063 301, 6 2021 (cit. on pp. 37, 38, 59).

[73] J. Philippi, P.-Y. Lagrée, and A. Antkowiak, "Drop impact on a solid surface: Short-time self-similarity," *Journal of Fluid Mechanics*, vol. 795, 96–135, 2016 (cit. on pp. 37, 43, 58).

[74] L. Gordillo, T.-P. Sun, and X. Cheng, "Dynamics of drop impact on solid surfaces: Evolution of impact force and self-similar spreading," *Journal of Fluid Mechanics*, vol. 840, 190–214, 2018 (cit. on pp. 37, 43, 54, 58).

[75] R. W. Style *et al.*, "Traction force microscopy in physics and biology," *Soft matter*, vol. 10, no. 23, pp. 4047–4055, 2014 (cit. on p. 38).

[76] V. Rathee, D. L. Blair, and J. S. Urbach, "Localized transient jamming in discontinuous shear thickening," *Journal of Rheology*, vol. 64, no. 2, pp. 299–308, 2020 (cit. on pp. 38, 58).

[77] V. Rathee, J. M. Miller, D. L. Blair, and J. S. Urbach, "Structure of propagating high stress fronts in a shear thickening suspension," *arXiv preprint arXiv:2203.02482*, 2022 (cit. on pp. 38, 58).

[78] S. Williams and A. Philipse, "Random packings of spheres and spherocylinders simulated by mechanical contraction," *Physical Review E*, vol. 67, no. 5, p. 051 301, 2003 (cit. on pp. 38, 41).

[79] N. M. James, H. Xue, M. Goyal, and H. M. Jaeger, "Controlling shear jamming in dense suspensions via the particle aspect ratio," *Soft matter*, vol. 15, no. 18, pp. 3649–3654, 2019 (cit. on pp. 38, 41).

[80] L. A. Lubbers, Q. Xu, S. Wilken, W. W. Zhang, and H. M. Jaeger, "Dense suspension splat: Monolayer spreading and hole formation after impact," *Phys. Rev. Lett.*, vol. 113, p. 044 502, 4 2014 (cit. on p. 39).

[81] I. R. Peters, Q. Xu, and H. M. Jaeger, "Splashing onset in dense suspension droplets," *Phys. Rev. Lett.*, vol. 111, p. 028 301, 2 2013 (cit. on pp. 39–41).

[82] M. H. Klein Schaarsberg, I. R. Peters, M. Stern, K. Dodge, W. W. Zhang, and H. M. Jaeger, "From splashing to bouncing: The influence of viscosity on the impact of suspension droplets on a solid surface," *Phys. Rev. E*, vol. 93, p. 062 609, 6 2016 (cit. on p. 40).

[83] V. G. Grishaev, I. K. Bakulin, and I. S. Akhatov, "Large fragmentation under drop suspension splashing," *Journal of Fluids and Structures*, vol. 91, p. 102 718, 2019 (cit. on p. 41).

[84] J. Mewis and N. J. Wagner, *Colloidal suspension rheology*. Cambridge University Press, 2012 (cit. on pp. 43, 46).

[85] T. Osswald and N. Rudolph, "Polymer rheology," *Carl Hanser, München*, 2015 (cit. on p. 43).

[86] N. V. David, X.-L. Gao, and J. Q. Zheng, "Ballistic Resistant Body Armor: Contemporary and Prospective Materials and Related Protection Mechanisms," *Applied Mechanics Reviews*, vol. 62, no. 5, 2009, 050802 (cit. on p. 43).

[87] D. Rus and M. T. Tolley, "Design, fabrication and control of soft robots," *Nature*, vol. 521, no. 7553, pp. 467–475, 2015 (cit. on p. 43).

[88] X. Cheng, T.-P. Sun, and L. Gordillo, "Drop impact dynamics: Impact force and stress distributions," *Annual Review of Fluid Mechanics*, vol. 54, no. 1, pp. 57–81, 2022 (cit. on pp. 43, 58).

[89] V. Bergeron, D. Bonn, J. Y. Martin, and L. Vovelle, "Controlling droplet deposition with polymer additives," *Nature*, vol. 405, no. 6788, pp. 772–775, 2000 (cit. on pp. 44, 81).

[90] B. C. Blackwell, M. E. Deetjen, J. E. Gaudio, and R. H. Ewoldt, "Sticking and splashing in yield-stress fluid drop impacts on coated surfaces," *Physics of Fluids*, vol. 27, no. 4, p. 043 101, 2015 (cit. on p. 44).

[91] M.-J. Thoraval *et al.*, "Nanoscopic interactions of colloidal particles can suppress millimetre drop splashing," *Soft matter*, vol. 17, no. 20, pp. 5116–5121, 2021 (cit. on p. 44).

[92] G. Kim, W. Kim, S. Lee, and S. Jeon, "Impact dynamics of a polystyrene suspension droplet on nonwetting surfaces measured using a quartz crystal microresonator and a high-speed camera," *Sensors and Actuators B: Chemical*, vol. 288, pp. 716–720, 2019 (cit. on p. 44).

[93] W. Stöber, A. Fink, and E. Bohn, "Controlled growth of monodisperse silica spheres in the micron size range," *Journal of colloid and interface science*, vol. 26, no. 1, pp. 62–69, 1968 (cit. on pp. 44, 61, 85, 127).

[94] L. Zhang *et al.*, "Hollow silica spheres: Synthesis and mechanical properties," *Langmuir*, vol. 25, no. 5, pp. 2711–2717, 2009 (cit. on pp. 44, 61, 85, 128).

[95] J. K. Whitmer and E. Luijten, "Sedimentation of aggregating colloids," *The Journal of Chemical Physics*, vol. 134, no. 3, p. 034 510, 2011 (cit. on p. 44).

[96] T. Shajahan and W.-P. Breugem, "Influence of concentration on sedimentation of a dense suspension in a viscous fluid," *Flow, Turbulence and Combustion*, vol. 105, no. 2, pp. 537–554, 2020 (cit. on p. 44).

[97] Drop Impact Supplementary Material. (), [Online]. Available: https://figshare.com/articles/media/Colloidal_drop_impact_SI_videos/19608918 (visited on 2022) (cit. on pp. 47, 48, 50–52, 54–56, 63).

[98] E. Brown and H. M. Jaeger, "Shear thickening in concentrated suspensions: Phenomenology, mechanisms and relations to jamming," *Reports on Progress in Physics*, vol. 77, no. 4, p. 046 602, 2014 (cit. on p. 46).

[99] J. F. Morris, "Shear thickening of concentrated suspensions: Recent developments and relation to other phenomena," *Annual Review of Fluid Mechanics*, vol. 52, no. 1, pp. 121–144, 2020 (cit. on p. 46).

[100] D. Bi, J. Zhang, B. Chakraborty, and R. P. Behringer, "Jamming by shear," *Nature*, vol. 480, no. 7377, pp. 355–358, 2011 (cit. on p. 48).

[101] N. M. James, H. Xue, M. Goyal, and H. M. Jaeger, "Controlling shear jamming in dense suspensions via the particle aspect ratio," *Soft matter*, vol. 15, no. 18, pp. 3649–3654, 2019 (cit. on pp. 48, 75, 78, 91, 110).

[102] G. Lagubeau, M. A. Fontelos, C. Josserand, A. Maurel, V. Pagneux, and P. Petitjeans, "Spreading dynamics of drop impacts," *Journal of Fluid Mechanics*, vol. 713, 50–60, 2012 (cit. on p. 54).

[103] B. R. Mitchell, J. C. Klewicki, Y. P. Korkolis, and B. L. Kinsey, "The transient force profile of low-speed droplet impact: Measurements and model," *Journal of Fluid Mechanics*, vol. 867, 300–322, 2019 (cit. on p. 54).

[104] L. D. Landau, E. M. Lifshitz, A. M. Kosevich, and L. P. Pitaevskii, *Theory of elasticity: volume 7*. Elsevier, 1986, vol. 7 (cit. on pp. 56, 57, 70).

[105] V. Rathee, D. L. Blair, and J. S. Urbach, "Localized stress fluctuations drive shear thickening in dense suspensions," *Proceedings of the National Academy of Sciences of the United States of America*, vol. 114, no. 33, pp. 8740–8745, 2017 (cit. on p. 58).

[106] A. J. Liu and S. R. Nagel, "The jamming transition and the marginally jammed solid," *Annual Review of Condensed Matter Physics*, vol. 1, no. 1, pp. 347–369, 2010 (cit. on p. 60).

[107] Supplementary Material. (), [Online]. Available: https://figshare.com/articles/media/Phalguni_Shah_Thesis_videos/20362833 (visited on 2022) (cit. on pp. 75–77, 97, 98, 107).

[108] A. Kuijk, A. Van Blaaderen, and A. Imhof, "Synthesis of monodisperse, rodlike silica colloids with tunable aspect ratio," *Journal of the American Chemical Society*, vol. 133, no. 8, pp. 2346–2349, 2011 (cit. on pp. 76, 81, 132, 133).

[109] R. Crooks, J. Cooper-White, and D. V. Boger, "The role of dynamic surface tension and elasticity on the dynamics of drop impact," *Chemical Engineering Science*, vol. 56, no. 19, pp. 5575 –5592, 2001, Festschrift in honour of Dr. R.A. Mashelkar (cit. on p. 81).

[110] D. Bartolo, A. Boudaoud, G. Narcy, and D. Bonn, "Dynamics of non-newtonian droplets," *Phys. Rev. Lett.*, vol. 99, p. 174 502, 17 2007 (cit. on p. 81).

[111] M. I. Smith and V. Bertola, "Effect of polymer additives on the wetting of impacting droplets," *Phys. Rev. Lett.*, vol. 104, p. 154 502, 15 2010 (cit. on p. 81).

[112] D. Zang, X. Wang, X. Geng, Y. Zhang, and Y. Chen, "Impact dynamics of droplets with silica nanoparticles and polymer additives," *Soft Matter*, vol. 9, pp. 394–400, 2 2013 (cit. on p. 81).

[113] R. Crooks and D. V. Boger, "Influence of fluid elasticity on drops impacting on dry surfaces," *Journal of Rheology*, vol. 44, no. 4, pp. 973–996, 2000 (cit. on p. 81).

[114] V. Bertola, "Dynamic wetting of dilute polymer solutions: The case of impacting droplets," *Advances in Colloid and Interface Science*, vol. 193-194, pp. 1–11, 2013 (cit. on p. 81).

[115] S. Poulain and L. Bourouiba, "Biosurfactants change the thinning of contaminated bubbles at bacteria-laden water interfaces," *Phys. Rev. Lett.*, vol. 121, p. 204 502, 20 2018 (cit. on pp. 83, 85).

[116] K. J. Mysels, S. Frankel, and K. Shinoda, *Soap films: studies of their thinning and a bibliography*. Pergamon press, 1959 (cit. on pp. 83, 85, 101).

[117] W. R. McEntee and K. J. Mysels, "Bursting of soap films. i. an experimental study," *The Journal of Physical Chemistry*, vol. 73, no. 9, pp. 3018–3028, 1969 (cit. on pp. 83, 85).

[118] S. Frankel and K. J. Mysels, "Bursting of soap films. ii. theoretical considerations," *The Journal of Physical Chemistry*, vol. 73, no. 9, pp. 3028–3038, 1969 (cit. on p. 83).

[119] Y. Zhang and V. Sharma, "Domain expansion dynamics in stratifying foam films: Experiments," *Soft matter*, vol. 11, no. 22, pp. 4408–4417, 2015 (cit. on pp. 83, 102).

[120] C. Ochoa, S. Gao, S. Srivastava, and V. Sharma, "Foam film stratification studies probe intermicellar interactions," *Proceedings of the National Academy of Sciences*, vol. 118, no. 25, e2024805118, 2021 (cit. on pp. 83, 102).

[121] P. Petit, M. Le Merrer, and A.-L. Biance, "Holes and cracks in rigid foam films," *Journal of Fluid Mechanics*, vol. 774, 2015 (cit. on pp. 83, 102, 111).

[122] F. Müller, U. Kornek, and R. Stannarius, "Experimental study of the bursting of inviscid bubbles," *Physical Review E*, vol. 75, no. 6, p. 065 302, 2007 (cit. on p. 83).

[123] D. Tammaro *et al.*, "Flowering in bursting bubbles with viscoelastic interfaces," *Proceedings of the National Academy of Sciences*, vol. 118, no. 30, e2105058118, 2021 (cit. on pp. 83, 84).

[124] Y. Timounay, E. Lorenceau, and F. Rouyer, "Opening and retraction of particulate soap films," *EPL (Europhysics Letters)*, vol. 111, no. 2, p. 26 001, 2015 (cit. on pp. 83, 84, 102, 111).

[125] A. Missaoui, K. Harth, T. Trittel, C. Klopp, R. Stannarius, and E. Lacaze, "Shape instabilities of islands in smectic films under lateral compression," *Soft Matter*, vol. 18, pp. 3193–3205, 16 2022 (cit. on p. 83).

[126] L. J. Evers, S. Y. Shulepov, and G. Frens, "Bursting dynamics of thin free liquid films from newtonian and viscoelastic solutions," *Phys. Rev. Lett.*, vol. 79, pp. 4850–4853, 24 1997 (cit. on p. 84).

[127] A. Sokolov, M. M. Apodaca, B. A. Grzybowski, and I. S. Aranson, "Swimming bacteria power microscopic gears," *Proceedings of the National Academy of Sciences*, vol. 107, no. 3, pp. 969–974, 2010 (cit. on p. 85).

[128] A. Sokolov, M. M. Apodaca, B. A. Grzybowski, and I. S. Aranson, "Swimming bacteria power microscopic gears," *Proceedings of the National Academy of Sciences*, vol. 107, no. 3, pp. 969–974, 2010 (cit. on p. 86).

[129] C. Akcay, P. Parrein, and J. P. Rolland, "Estimation of longitudinal resolution in optical coherence imaging," *Appl. Opt.*, vol. 41, no. 25, pp. 5256–5262, 2002 (cit. on p. 94).

APPENDIX A
SYNTHESIS AND CHARACTERIZATION OF COLLOIDAL PARTICLES

For all the experiments described above, silica colloidal particles were synthesized and cleaned in the lab, in order to control the particle size and polydispersity. Additionally, preparing and cleaning the particles in the lab ensures that the particles are suspended in a surfactant-free medium, in contrast with commercially available particles. To maximize the quality and yield of the colloidal particles, all the glassware used for the synthesis procedure was cleaned with a base bath.

A.1 Base bath cleaning

To make a base bath solution, the following reagents are mixed in a 100 mL media bottle:

- 10 g anhydrous NaOH pellets,
- 40 mL ultrapure (miliQ) water (18.2 MΩ.cm),
- 60 mL cleaning-grade ethanol.

As NaOH pellets are hygroscopic, they were weighed quickly to minimize exposure to air. Additionally, since the dissolution of NaOH in water is exothermic, the reaction flask was run under cold water until all of the base was dissolved in water.

For every synthesis reaction, all the graduated cylinders and media bottles were cleaned with the base bath. Coating thoroughly with the base removes a majority of organic impurities. After coating, removing all the base is crucial. The glassware is therefore cleaned and coated in multiple steps:

1. Rinse glassware with Deionised water (tap water has too many impurities, and it should not be used for cleaning).
2. Coat and scrub glassware with a solution of dish soap.
3. Rinse again with DI until all the soap is removed.
4. Pour a few mL of base bath in the container, and coat thoroughly, for at least 2 minutes.
5. Pour out the base bath, and rinse with DI repeatedly, at least 2 minutes.
6. Coat with ultrapure water and rinse repeatedly, at least 2 minutes.
7. Dry the glassware in the oven, at about 70°C - 95°C.

At each step, gloves are washed with ultrapure water to remove traces of soap and the base bath.

A.2 Silica sphere synthesis

Silica spheres were made using the Stöber [93] synthesis method. The process involves the hydrolysis of a tetraalkyl silicates with ammonia acting as a catalyst. The chemical reaction proceeds via an intermediate step where a mixture of alkoxysilanols is produced. However, it can be conveniently summarized as:

$$\mathrm{Si(OR)_4} + 2\,\mathrm{H_2O} \xrightarrow{\mathrm{NH_3}} \mathrm{SiO_2} + 4\,\mathrm{ROH}$$

The choice of ester and alcohol changes the quantitative details of chemical amounts, reaction kinetics, and the size of particles obtained. For the syntheses performed in our

lab, the procedure by Zhang et al. [94] was followed; the reagents used were tetraethyl orthosilicate (TEOS) and ethanol. This reaction leads to a formation of a crosslinked network of silicon and oxygen atoms, leading to spherical particle growth. After the reaction initiation, silica particles grow as spherical shells around the seed particles formed. Therefore, the size of final particles can be increased by performing more and more reaction 'feeds'. As a result of separate synthesis batches prepared in our lab, 1 feed led to particles of diameter around 450 nm, 10 feeds led to 700 nm, and 14 feeds led to 830 nm [Figure A.1]. All the reactions were allowed to proceed in the fume hood at room temperature.

Age of the reagents or errors in the amounts of reactants added can cause the size and polydispersity of spheres to deviate from the values reported above. The yield of this reaction was 5-20 mL, depending on the number of feeds. One successful reaction run produced a sufficient amount of spheres for our experiments.

A.2.1 Synthesis procedure

- **Reaction initiation**

  Day 1:

  1. In a media bottle, add 67 mL reaction-grade Ethanol.
  2. Add 5 mL ammonia (25% ammonium hydroxide solution).
  3. Dropwise add 3 mL of TEOS.
  4. Add a clean magnetic stir bar to the reaction mixture, seal the bottle with Parafilm.
  5. Leave the media bottle on a stirring plate overnight at approx. 200 RPM. Visu-

ally verify that all the reaction mixture is getting mixed.

Day 2:

1. Measure 20 mL ultrapure water.
2. Measure 25 mL TEOS.
3. Simultaneously add both reagents to the reaction mixture.
4. Re-position the sealed media bottle on the stirring plate, increase the RPM so that all the fluid is being mixed.

- **Reaction feeds (Days 3 – n)** Note: For this protocol, the reaction for each feed takes about 14 to 18 hours to complete. Therefore, we perform one feed each day.

  1. Add 25 mL TEOS and 20 mL miliQ water, together.
  2. Add 1.55 mL ammonia.
  3. Re-position the sealed media bottle on the stirring plate, increase the stirring RPM accordingly, leave overnight.

A.2.2 Cleaning and separation

After completion, the fluid in the reaction flask is primarily ethanol with small amounts of other reagents. The purpose of cleaning is to remove these chemicals and replace them with the suspending fluid desired for experiments, in our case, water. Furthermore, in addition to spheres of the desirable size, silica structures much larger than the desire spheres (millimeters in size), as well as spheres smaller than the desired size are present in the reaction mixture. The purpose of separation is to remove these structures to obtain a monodisperse sample.

Cleaning of silica spheres

1. Transfer contents of the reaction flask to 50 mL centrifuge tubes. Rinse the reaction flask with ethanol to remove residue from the flask, transfer it to centrifuge tubes as well.

2. Seal the centrifuge tubes with Parafilm, mass-balance them, and centrifuge at 1000× g for 35 minutes (This speed may need to be increased or decreased by $\sim 200\times g$, according to the size of spheres).

3. Gently remove the tubes from the centrifuge, remove and discard the supernatant fluid (clear).

4. Fill the tubes with water (if samples will be stored long-term, Ethanol), seal with Parafilm, sonicate in the ultrasonic bath for 20 minutes.

5. Mix the samples well with a vortex mixer.

6. Repeat steps 2-5 two more times.

Separation of silica spheres

This reaction generates a significant amount of large millimetric structures of silica, as the reaction builds a network of Silicon and Oxygen atoms. As silica is much denser than the reaction fluid, these large particles can be separated using gravity.

For gravity separation of large structures, we:

1. Mix the sonicated sample in 50mL centrifuge tubes with a vortex mixture.

2. Leave the sample undisturbed for 15 minutes, to separate under gravity.

3. Gently transfer the supernatant to another tube with a pipette, leaving behind the sediment.

4. Check both the supernantant and sediment under the microscope to check that the supernatant mostly consists of microscopic spheres, and sediment mostly contains millimetric junk.

5. Mix the sample with a vortex mixer again, and leave it undisturbed overnight for separation.

6. After overnight separation, repeat steps 3-4.

7. Depending on the quality of samples obtained, repeat the above steps as needed. Discard the millimetric junk.

For separation of smaller spheres, we:

1. Mix the sonicated sample in 50mL centrifuge tubes with a vortex mixture.

2. Parafilm and mass-balance the centrifuge tubes, centrifuge at 300g for 15 minutes.

3. Gently remove the tubes from the centrifuge, remove the supernatant fluid (milky).

4. Check both the supernatant and sediment under the microscope to verify that the sediment has spheres of the desirable size, while the supernatant has smaller particles.

5. Parafilm and sonicate the sample for 10 minutes.

6. repeat steps 1-5 two more times.

A.3 Silica rod synthesis

Silica rods of varying aspect ratios were prepared by following the synthesis method outlined by Kuijk et al. [108]. Rodlike structures form due to differential attachment of silica onto an emulsion water drop suspended in a medium of pentanol and Polyvinylpyrrolidone (PVP). The width of the rods is determined by the emulsion droplet size (around 200nm), and the aspect ratio (the ratio of length and diameter of the rods) is varied by tuning the length of rods. Unlike the Stöber process, the desired particle size is independent of the reaction time. Instead, the length (and in turn aspect ratio) is most conveniently controlled by varying the reaction temperature. Temperature ranging from 4°C to 31°C result in rods of aspect ratios 1 to 20. Unlike the sphere synthesis, the yield for this reaction is very low ($\sim$ 400 µL for the reaction in a 1 L flask), requiring us to perform multiple rounds of synthesis to produce enough high-quality rods.

A.3.1 Synthesis procedure

As with the sphere synthesis, the quality and age of ammonia used was crucial in the rod synthesis. Additionally, the age of Tetraethyl orthosilicate (TEOS) was also key to producing rods of consistently high quality and aspect ratios. We exclusively used small bottles of TEOS (25mL) for rod syntheses in order to minimize the age of TEOS used. To make silica rods in a 1 L media bottle, we:

1. Mix 0.529 g Sodium citrate dihydrate in 10 mL ultrapure water.
2. Add 600 mL Pentanol and 60g PVP in a 1L media bottle.
3. Seal the bottle with parafilm and use the shaker to mix pentanol and PVP: approx. 4 hours at 300 RPM.

4. Add 60 mL of reaction-grade ethanol.
5. Add 16.8 mL MiliQ water.
6. Add 4 ml sodium citrate dihydrate solution (from step 1) in one shot.
7. Add 13.5 mL ammonia.
8. Add 6ml TEOS.
9. Seal the bottle with Parafilm, leave overnight in the Incufridge set at a suitable temperature for rods of a desired aspect ratio.

AR 4.7 rods were made at 21° C, AR 6 rods at 27° C, and AR 12 rods were made at 31° C [Figure A.2]. Reaction was allowed to proceed overnight in 1L media bottles, and during each session 4-6 flasks were prepared simultaneously to increase yield. As mentioned before, the rod aspect ratio and polydispersity are very sensitive to the quality of reactants and any errors in measuring reactants. Therefore, particles from each flask were imaged separately via SEM after cleaning, and only after analyzing each sample for aspect ratio any consolidation was done.

A.3.2 Cleaning and separation

For both cleaning and separation, we followed Kuijk et al. [108]. Cleaning of silica rods is similar to that of spheres, as the density of particles is the same, and the two reactions share many reactants:

1. Transfer contents of the reaction flask to 50 mL centrifuge tubes. Rinse the reaction flask with water to remove residue from the flask, transfer it to centrifuge tubes.

2. Seal the centrifuge tubes with Parafilm, balance them, and centrifuge at 1500 × g for 1 hour.

3. Gently remove the tubes from the centrifuge, remove and discard the supernatant fluid (milky), after checking that it does not contain a significant amount of rods.

4. Fill the tubes with water (if samples will be stored long-term, ethanol), seal with Parafilm, sonicate in the ultrasonic bath for 20 minutes.

5. Mix the samples well with a vortex mixer.

6. Seal the centrifuge tubes with Parafilm, mass-balance them, and centrifuge at 1500 × g for 15 minutes.

7. Repeat steps 3-6 two more times.

The reaction mixture for the rods is milky in color. This fact added with the very low yield calls for repeated checking under the microscope before discarding any fluid, so as to not lose good rods.

Unlike the spheres, this reaction does not lead to a significant amount of millimetric junk. However, the sample is checked under the microscope and gravity separation is performed as needed. Separation of smaller rods is more challenging than the spheres, due to the added parameter of aspect ratio. Separation under gravity or centrifuging relies on the mass distribution of particles. The mass of spherical particles scales as the cube of particle diameter. However, for rod-shaped particles, as the diameter of the rods is more or less the same, the mass of the rods scales linearly with their AR. Moreover, there is a distribution in both the diameter and length, and two rods of similar mass can have very different aspect ratios. This effect is amplified at higher temperature reactions

for high-AR rods, where many small rods are present. For separating the short rods and improving the monodispersity, the below procedure is followed:

1. Mix the sonicated sample in 50 mL centrifuge tubes with a vortex mixture.
2. Parafilm and balance the centrifuge tubes, centrifuge at 700 g for 15 minutes.
3. Gently remove the tubes from the centrifuge, remove the supernatant fluid (milky).
4. Check both the supernantant and sediment under the tabletop microscope to estimate the rod size, and verify that the sediment has rods of the desirable AR, while the supernatant has shorter rods.
5. Parafilm and sonicate the sample for 20 minutes.
6. Repeat steps 1-5 two more times.

A.4 Particle characterization via SEM and analysis

The particles were imaged using the Hitachi S4800 Scanning Electron Microscope located in the NUANCE facility [Figures A.1, A.2]. As silica is non-conductive, the samples required a conductive coating to be imaged. A coating of Au-Pd, around 7 nm in thickness, worked well for imaging a large number of particles for size characterization. However, in cases where high-resolution details samples were coated with Osmium vapor.

SEM images were analyzed using ImageJ. For all the particle size statistics reported here, a representative sample of 50 or more particles was measured, and the standard deviation was reported as the size uncertainty [Figures A.1d, A.2d]. For characterizing the rods, the AR of each individual rod was calculated and statistics were performed on the ensemble of AR values.

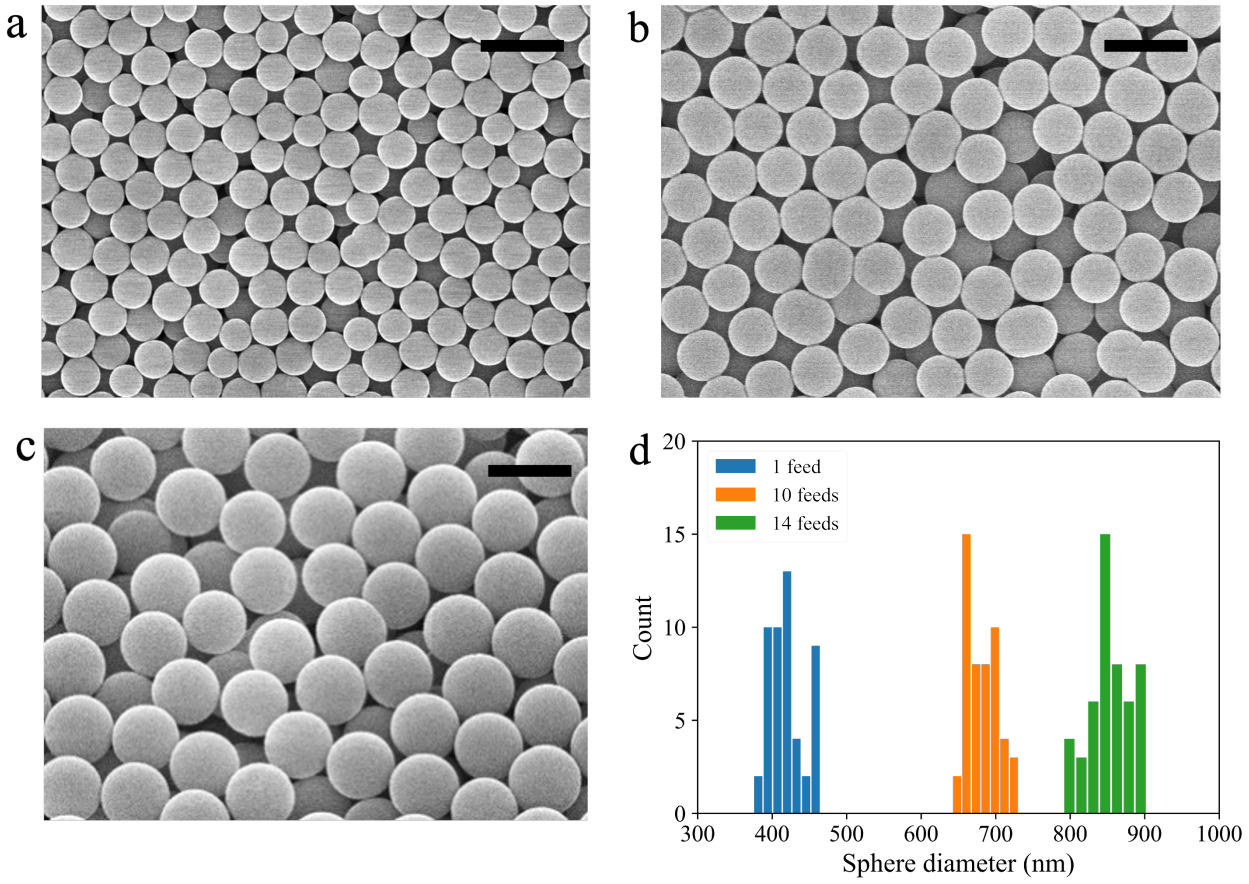

Figure A.1: **Silica spheres of increasing size, as a result of more reaction feeds.** (a) One reaction feed leads to spheres of about 450 ± 40 nm, (b) 10 reaction feeds give 680 ± 20nm spheres, and (c) 14 reaction feeds lead to spheres of 830 ± 20 nm diameter. Scale bars are 1 μm for (a) – (c). SEM images are courtesy of Dr. Srishti Arora. (d) Statistical distribution of 50 sphere diameters show that the spheres are highly monodisperse.

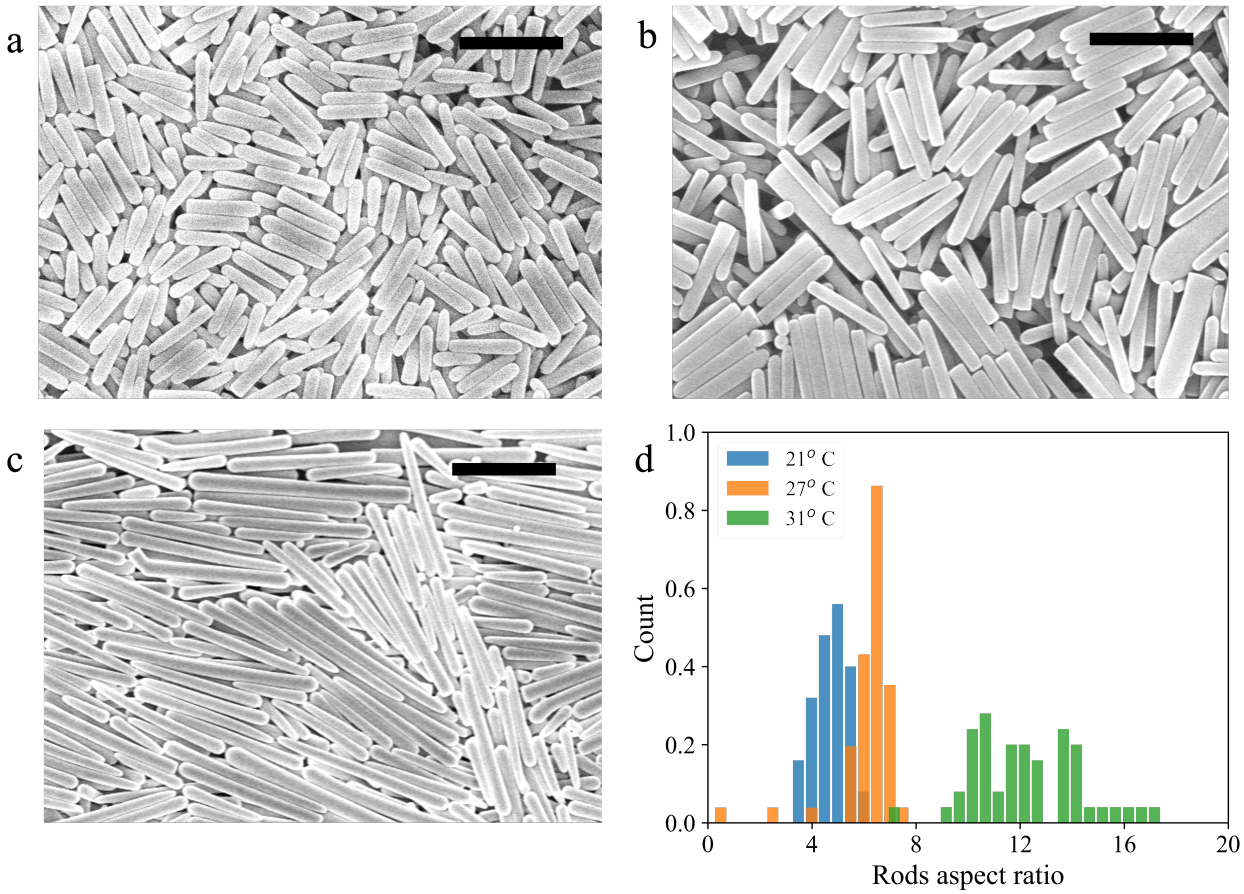

Figure A.2: **Silica rods of increasing aspect ratio, as a result of increasing reaction temperature.** Reaction at (a) 21^o C leads to rods of aspect ratio 4.7 ± 0.6, (b) 27^o C leads to rods of aspect ratio 6.1 ± 1.1, and (c) 31^o C leads to rods of aspect ratio 12.2 ± 2.1. Scale bars are 2 µm for (a) – (c). (d) Statistical distribution of 50 rod aspect ratios. Higher aspect ratio rods tend to be more polydisperse, and more challenging to separate in order to increase monodispersity.

APPENDIX B

MAXIMUM SPREAD OF IMPACTING COLLOIDAL DROPS: ROBUSTNESS AGAINST EFFECTIVE VISCOSITY MODELS

In section 4.2, we reported the scaling of the maximum drop spread for $\phi \leq 0.47$ colloidal drops with respect to $ReWe^{1/2}$[Figure 4.4b]. This scaling was reported by Scheller et al. [19] for experimental data of impacting glycerol-water drops of varying viscosity. Both the collapse of our data and the power-law exponent are in surprising agreement with the Newtonian scaling, given the highly shear-thinning behavior at high volume fractions apparent from the bulk rheology data [Figure 4.1]. More recently, further modifications to this scaling models have been reported for Newtonian fluids [11, 14, 15]. The dependence on the Reynolds number in both the viscous and the inertial regimes has been explored, and a universal scaling in terms of We and Re, that interpolates between these two regimes, has been proposed [14]. The effects of substrate wettability have additionally been incorporated in a modified scaling [15].

A detailed comparison of the various models for maximum spreading of impacting Newtonian fluids has been made by Josserand and Thoroddsen [11]. Here, we plot of our colloidal data separately with We and Re, and additionally compare how our data scales with respect to the various scaling models for Newtonian drops.

Figure B.1 shows our data for β plotted against $We^{1/2}, Re_{rheo}$, and Re_{KD}. The fact that β does not collapse when plotted against $We^{1/2}$ alone is expected [Figure B.1a], as the effective viscosity of the suspension changes significantly with ϕ. When plotted against the Reynolds numbers alone, on the other hand, the data collapse is impressive for both

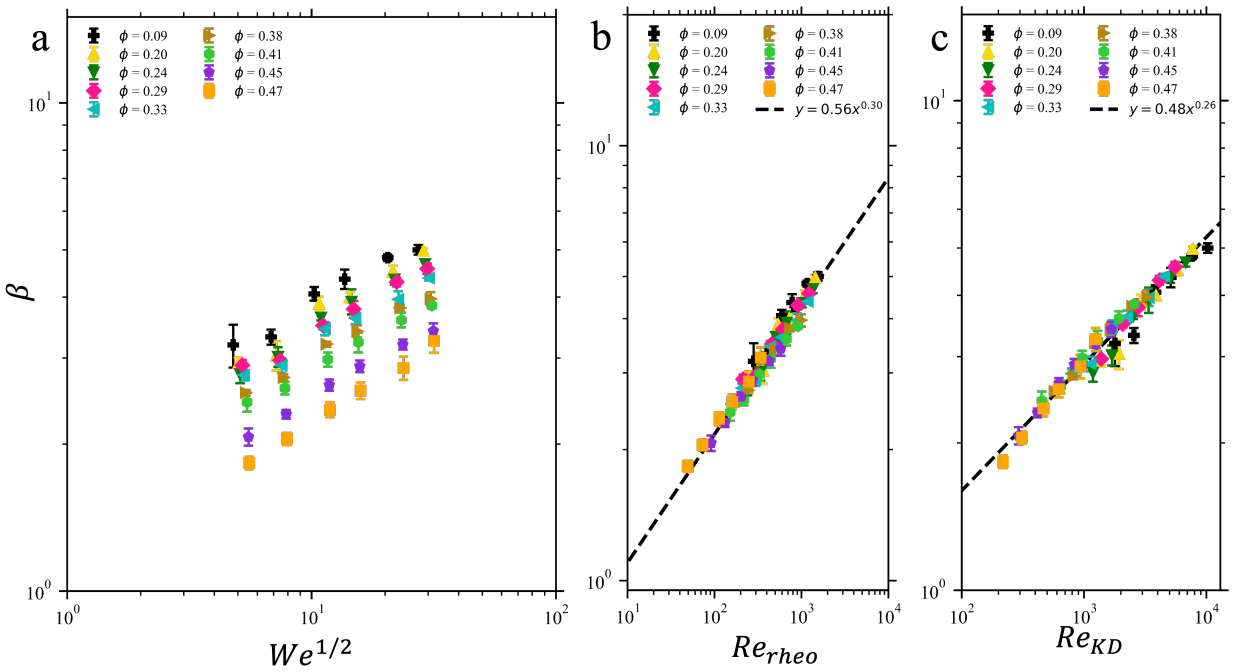

Figure B.1: **Maximum drop spread after impact vs. dimensionless numbers a** β vs. Weber number, We. The data does not collapse indicating a dependence on viscosity via the Reynolds number. **b** β vs. Re_{rheo}, the Reynolds number calculated from the effective viscosity taken from rheological data. The dotted line is a power-law fit with an exponent of 0.30, as compared to the exponent 0.20 reported for impacting Newtonian drops. **c** β vs. Re_{KD}, the Reynolds number calculated from the Krieger-Dougherty effective viscosity. The dotted line is a power-law fit with an exponent of 0.26, as compared to the exponent 0.20 reported for impacting Newtonian drops.

Re_{rheo} [Figure B.1b] and Re_{KD} [[Figure B.1c]]. This indicates that although the role of inertia is important, the contribution of fluid viscosity is very significant in determining the maximum spread of colloidal drops. The exponents of the power-law fit is 0.30 in terms of Re_{rheo} and 0.26 in terms of Re_{KD}. These exponents deviate the exponent of 0.20 expected from theoretical models (cite things). Experiments with Newtonian drop impact have also reported deviation from this value (cite things).

Figure B.2 shows β plotted against $ReWe^{1/2}$ for both Re_{rheo} and Re_{KD}. Once again,

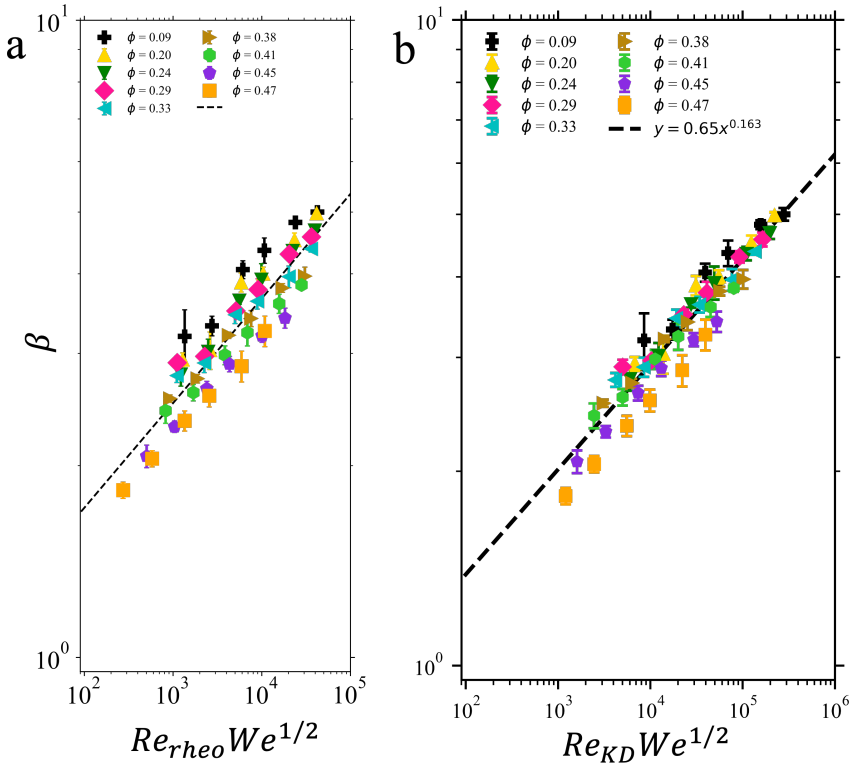

Figure B.2: **Scaling of maximum drop spread after impact: plotted against$ReWe^{1/2}$. a** β plotted against $Re_{rheo}We^{1/2}$. The data collapses well, and the dotted line is a power-law fit with the exponent 0.164, which agrees well with the scaling reported by Scheller et al. [19]. **b** β plotted against $Re_{KD}We^{1/2}$ also collapses well, and the dotted line is a power-law fit with the exponent 0.163, nearly identical to that of (a) and in great agreement with Scheller et al. [19].

both scalings show a good collapse, and the power-law exponents are nearly identical. The K-D effective viscosity model is designed for predicting the suspension viscosity at low shear rate. As the fluid spreading after impact experiences high and variable shear rate, we believe that Re_{rheo} is a more physical choice. We elaborate on this at the end of this appendix.

Equations for Scheller scaling and the other more contrived scaling.

As mentioned before, theoretical models suggest a $Re^{0.20}$ scaling for β. In Figure B.3,

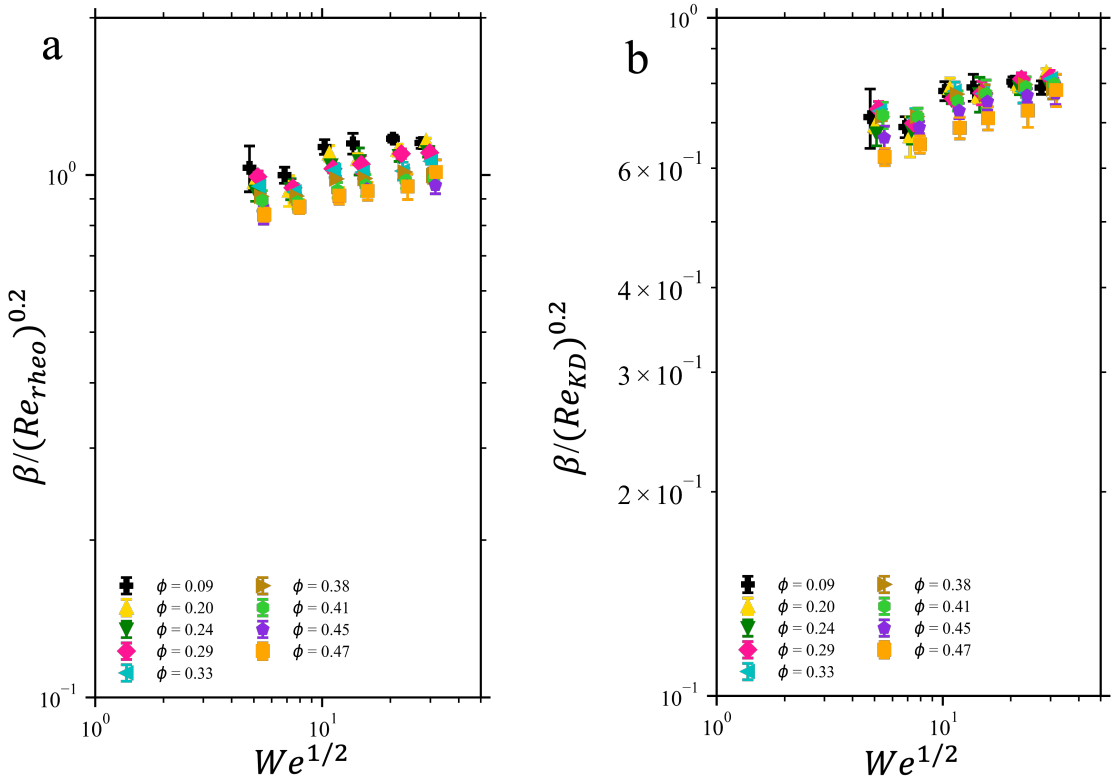

Figure B.3: $Re^{1/5}$ **Scaling of maximum drop spread after impact. a** $\beta/(Re_{rheo})^{0.2}$ plotted against We, on similar lines as Lee et al. [15]. **b** $\beta/(Re_{KD})^{0.25}$ plotted against We, on similar lines as Lee et al. [15]. The data shows an imperfect collapse, where datasets for different values of ϕ are distinctly visible.

we plot β normalized with $Re_{rheo}^{0.20}$ and $Re_{KD}^{0.20}$ respectively, against $We^{1/2}$. The data shows an imperfect collapse, especially in Figure B.3a. As we observed the data to scale with different exponents of the Reynolds numbers in Figure B.1b and c, we plot β normalized with those $Re_{rheo}^{0.30}$ and $Re_{rheo}^{0.26}$ against $We^{1/2}$ in Figure B.4. The collapse with these experimentally determined exponents is much improved.

In Figure B.5, $\beta/Re^{1/5}$ is plotted against $WeRe^{-2/5}$, similarly as Laan et al. [14]. The data shows a better collapse for Re_{KD} than for Re_{rheo}. We also note that the collapsed

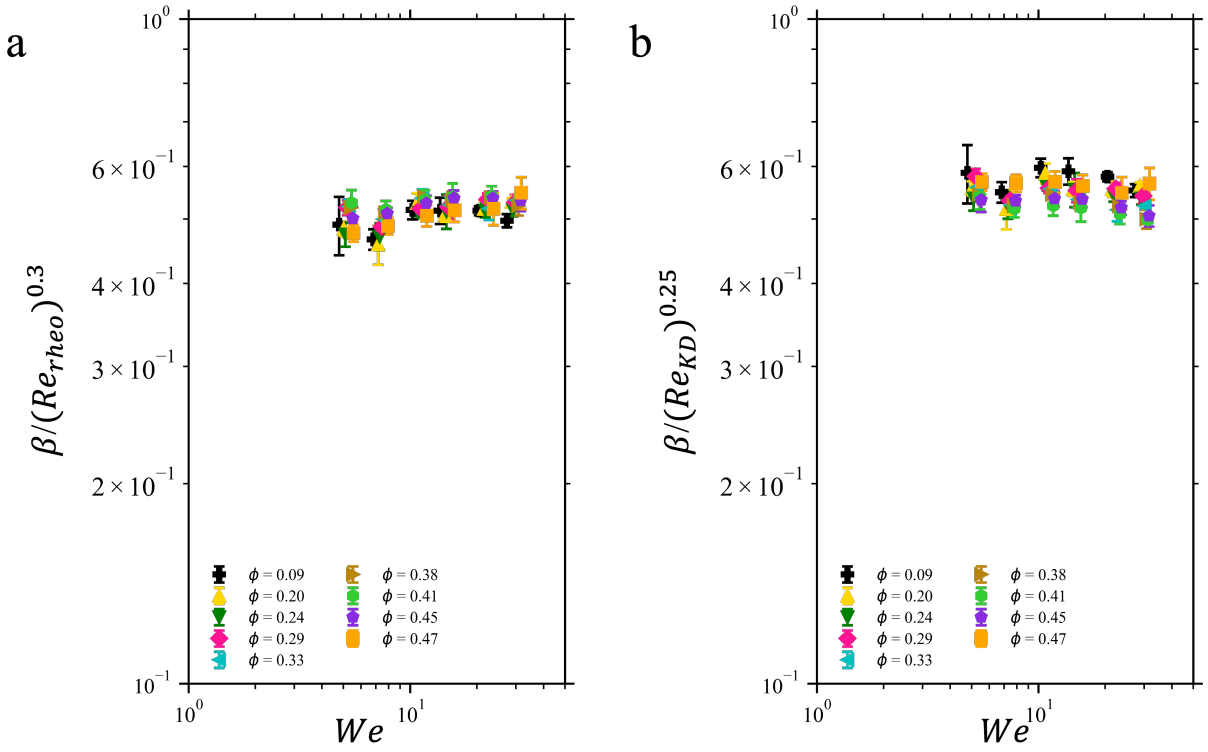

Figure B.4: **Modified scaling of maximum drop spread after impact. a** $\beta/(Re_{rheo})^{0.3}$ plotted against We, on similar lines as Lee et al. [15], and with the exponent from Fig. B.1b. The data collapses well onto a practically constant value, despite the relatively low We values. **b** $\beta/(Re_{KD})^{0.25}$ plotted against We, on similar lines as Lee et al. [15], and with the exponent from Fig. B.1c. The data collapses well onto a practically constant value, despite the relatively low We values.

data stays practically constant as a function of $WeRe^{-2/5}$, not consistent with the Padé approximant found by fitting Newtonian data in past studies [14, 15].

Recently, the effects of substrate wettability have been incorporated in the maximum drop spread scaling [15]. Lee et al. obtained $\beta_{v\to 0}$, the maximum spread in the limit of zero impact velocity, by considering a Padé approximation,

$$\beta = \beta_{v\to 0} + \frac{av^c}{b + v^c}, \tag{B.1}$$

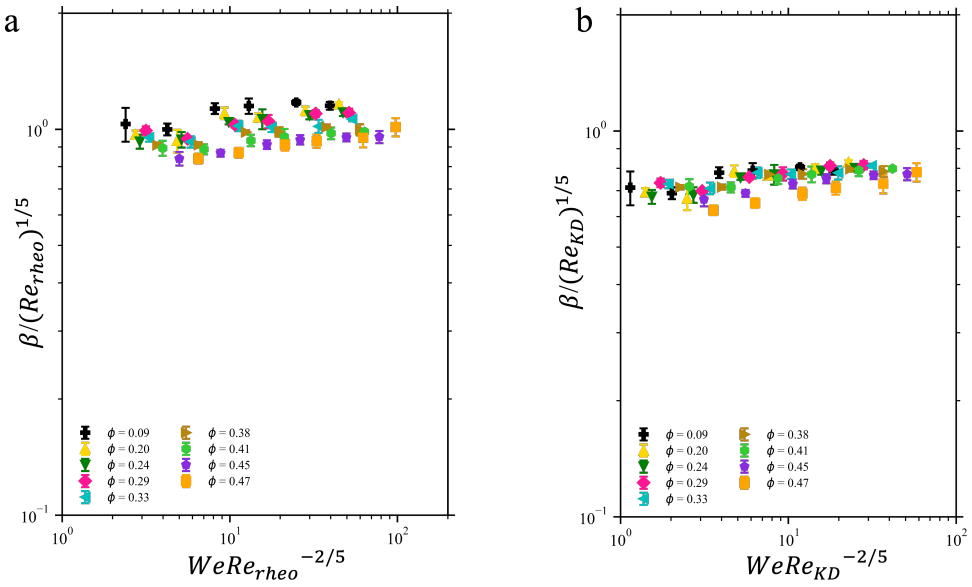

Figure B.5: **Modified scaling of maximum drop spread after impact, plotted against $WeRe^{-2/5}$. a** $\beta/(Re_{rheo})^{1/5}$ plotted against $WeRe^{-2/5}$, on similar lines as Laan et al. [14], The data shows an imperfect collpase. **b** $\beta/(Re_{KD})^{1/5}$ plotted against $WeRe^{-2/5}$, on similar lines as Laan et al. [14]. The data shows a better collapse relative to panel (a).

where $\beta_{v\to 0}, a, b$, and c are fitting parameters. So that β increases linearly with v for small v, and is independent of v at large v. This assumption is reasonable since we expect substrate wettability to have a negligible effect in the high-inertia regime. In Figure B.6, we show the estimate of $\beta_{v\to 0}$ for a first-order Padé approximation over ϕ, where we set $c = 1$:

$$\beta = \beta_{v\to 0} + \frac{av}{b+v}. \tag{B.2}$$

The inset shows an example fit for $\phi =$. The value of $\beta_{v\to 0}$ seems to remain more or less constant over ϕ. The average of these values is 1.62, indicated by the dashed black line. We use this average value as $\beta_{v\to 0}$ for all ϕ values. We use this value to compute a

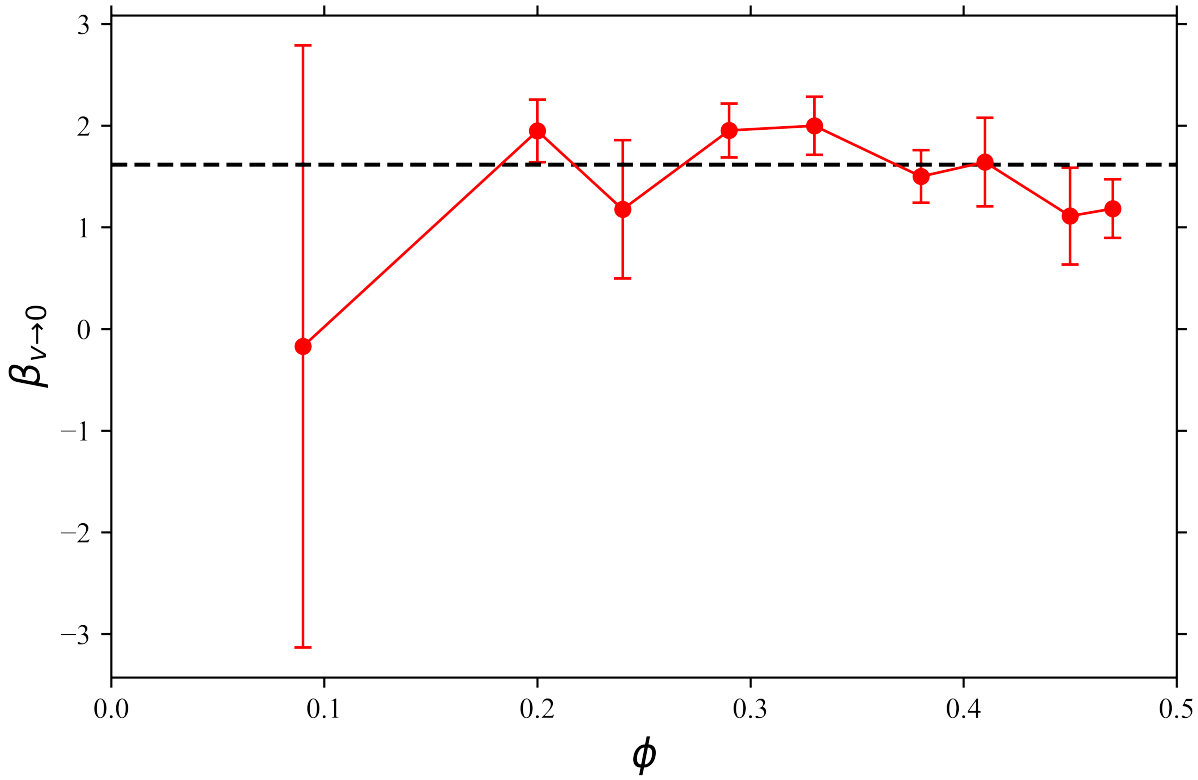

Figure B.6: **Prediction of the maximum spread at zero impact velocity using the first order Padé approximation.** $\beta_{v\to 0}$ obtained by fitting $\beta = \beta_{v\to 0} + \frac{av}{b+v}$, as used in Lee et al. [15], for the whole range of volume fractions. As seen from the plot, the average value is fairly constant over volume fractions. For the wettability-corrected scaling, we use the average value of $\beta_{v\to 0} = 1.62$, denoted by the dashed black line.

modified spreading factor, $\sqrt{\beta^2 - {\beta_{v\to 0}}^2}$ [15]. Instead of linear subtraction, the difference of squares is used, as the effect of surface wettability is expected to scale as the surface area, that goes quadratically as the linear drop spread.

In Figure B.7, we plot this modified spreading factor against $ReWe^{1/2}$. The data collapses imperfectly for both Re_{rheo} and Re_{KD}, especially where the drops spread less. This is to be expected, as the effect of any uncertainty in $\beta_{v\to 0}$ is expected to be higher for

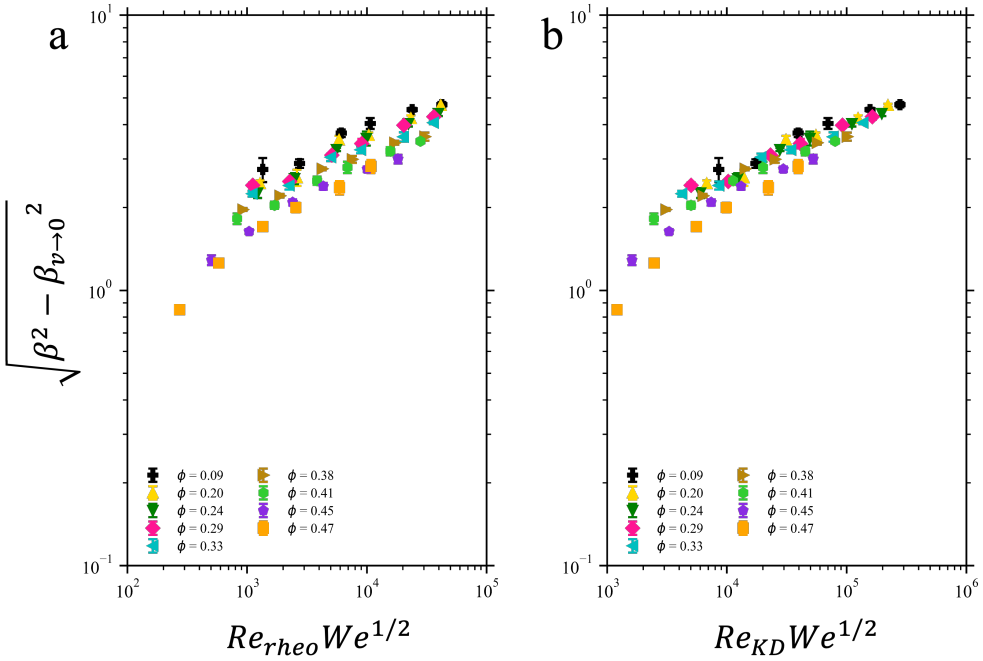

Figure B.7: **Modified scaling of maximum drop spread after impact, plotted against $ReWe^{1/2}$. a** $\sqrt{\beta^2 - \beta_{v\to 0}{}^2}$ plotted against $Re_{rheo}We^{1/2}$. **b** $\sqrt{\beta^2 - \beta_{v\to 0}{}^2}$ plotted against $Re_{KD}We^{1/2}$, as in Scheller et al. [19]. The data shows an imperfect collapse.

lower β values. In Figure B.8 where we plot $\sqrt{\beta^2 - \beta_{v\to 0}^2}$ against Re_{rheo} and Re_{KD}, although we observe a much better collapse of data, the collapse is again imperfect especially for $\phi = 0.47$ where the drop spread is smaller. The relatively better quality of collapse once again indicates that the Reynolds number has a very significant role in governing the maximum drop spread. The exponents of the power-law fits, 0.42 for Re_{rheo} and 0.37 for Re_{KD}, deviate even more from the expected value of 0.20. We now use normalize the spreading factor by these powers of Re, and plot it against the Weber number in Figure B.10. The data points do not perfectly collapse on to pf each other. However, considering the very small range on the y-Axis, the data seems to be a practically constant function of We (similar to Figure B.4).

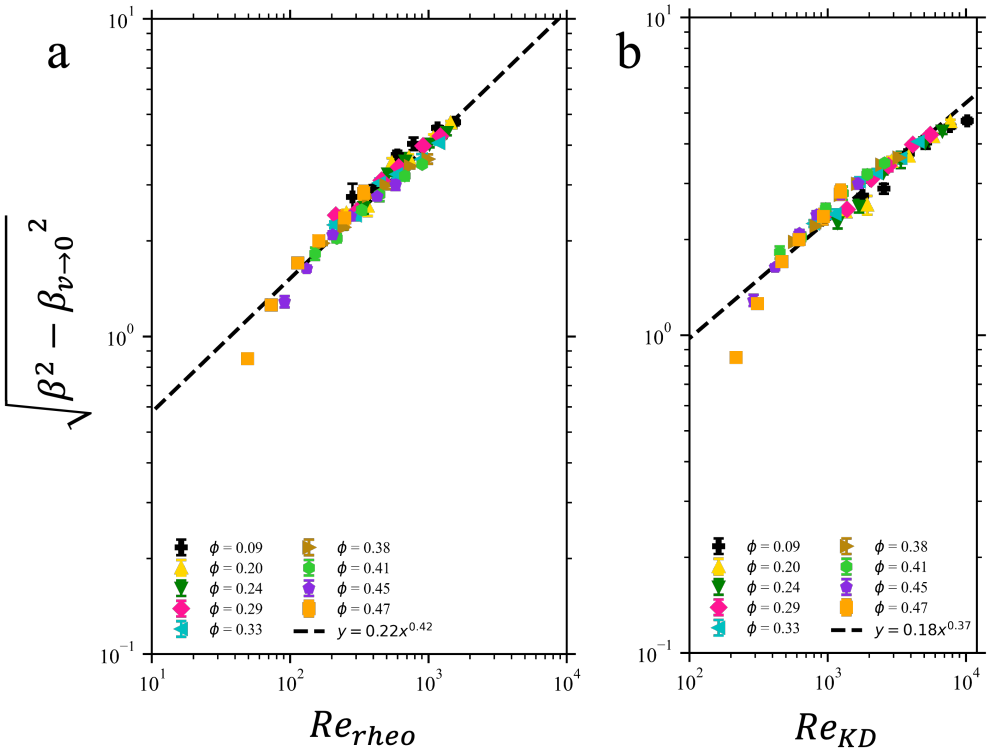

Figure B.8: **Modified scaling of maximum drop spread after impact.** $\sqrt{\beta^2 - \beta_{v\to 0}{}^2}$ plotted against **a** Re_{rheo} and **b** Re_{KD}
. Dotted lines show the power-law fit exponents that are much larger than the usual $Re^{1/5}$ scaling reported for Newtonian drop impact.

Although correcting for surface wettability probably takes us closer to a realistic model of drop spreading after impact, in case of our colloidal suspension data we did not see much improvement in the quality of the collapse when β was corrected for surface wettability. We used first-order version [Equation B.2] of the correction reported by Lee et al. [15], where $\beta_{v\to 0}$ is obtained as a fitting parameter to the β vs. impact velocity data by assuming a Padé approximant [Equation B.1]. This function is a reasonable choice as it interpolates smoothly between the two expected spreading regimes, however, the large number of fitting parameters indicate there is much unknown about the intermediate

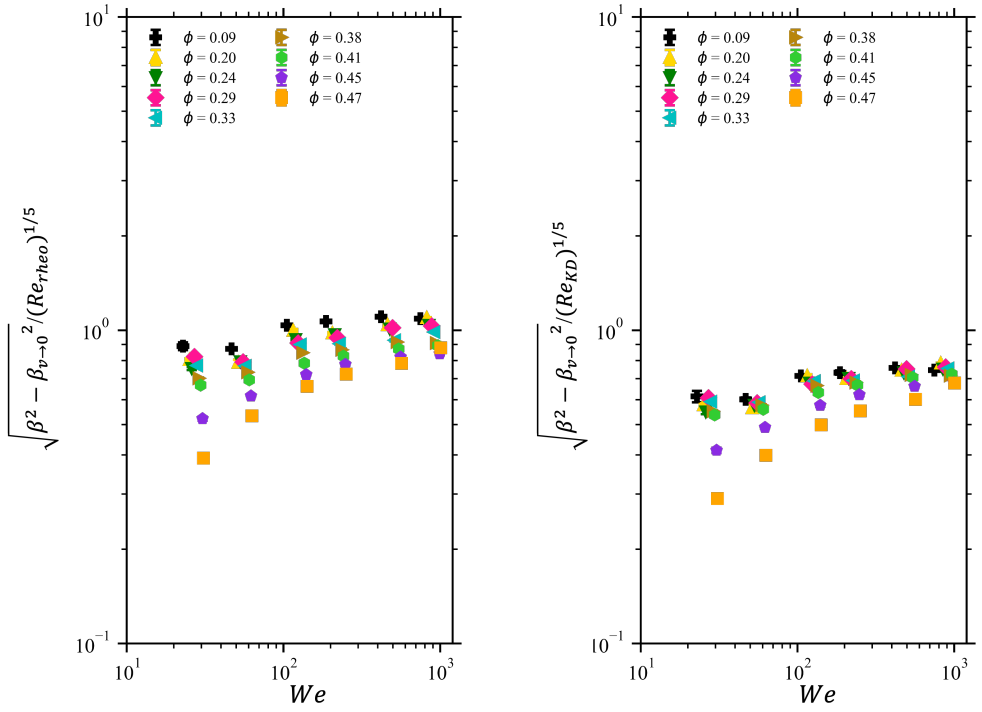

Figure B.9: **Scaling of maximum drop spread after impact: corrected for surface wettability and normalized with $Re^{1/5}$, plotted against We, as reported by Lee et al. [15]. a** $\sqrt{\beta^2 - \beta_{v\to 0}{}^2}/(Re_{rheo})^{1/5}$ plotted against We, on similar lines as Lee et al. [15], **b** $\sqrt{\beta^2 - \beta_{v\to 0}{}^2}/(Re_{KD})^{1/5}$ plotted against We, on similar lines as Lee et al. [15] In both cases, the data collapses imperfectly, especially for high ϕ.

regime.

The high quality of the collapse in terms of both Re_{rheo} and Re_{KD} leaves the question of a more appropriate viscosity model unanswered. We still believe that Re_{rheo} is the more suitable choice for the following reasons: The K-D effective viscosity model is not an ideal choice, as it relies on a jamming volume fraction for the specific colloidal suspension, and it is designed for systems experiencing low shear. Moreover, given that the shear rates within the drop change dynamically during spreading, any choice of an effective viscosity

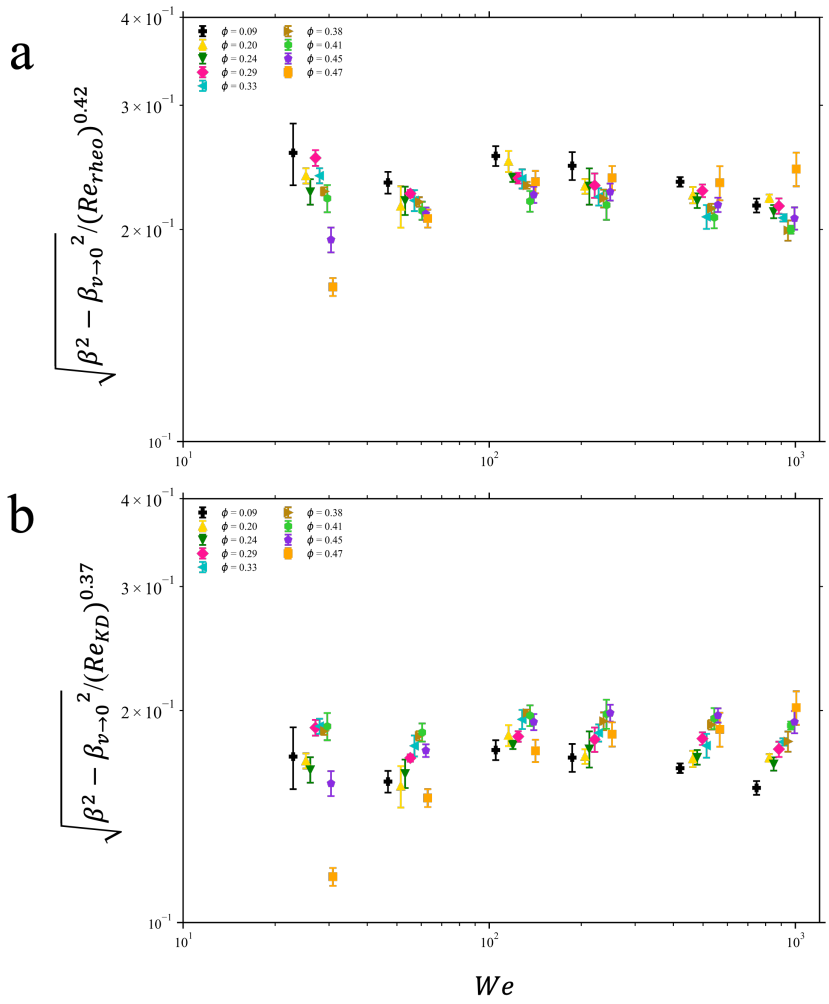

Figure B.10: **Modified scaling of maximum drop spread after impact, plotted against We.** **a** $\sqrt{\beta^2 - \beta_{v\to 0}{}^2}/(Re_{rheo})^{0.42}$ plotted against We, on similar lines as Lee et al. [15], and with the exponent from Fig. B.8a. **b** $\sqrt{\beta^2 - \beta_{v\to 0}{}^2}/(Re_{KD})^{0.37}$ plotted against We, on similar lines as Lee et al. [15], and with the exponent from Fig. B.8b. In both cases, the data collapses onto a practically constant value, despite the relatively low We values.

model from the literature is expected to prove inadequate without some estimate of an 'effective' shear rate. The simple estimate of an effective shear rate we provide in chapter 4 accounts for the variation of shear, both over impact velocities, and over the spreading time. As we have also collected rheology data specific to our colloidal suspension, pairing the estimated shear rate with a viscosity value is straightforward. We believe that this method captures the flow properties specific to our suspension in the most realistic way.

Our data shows an impressive collapse when plotted in terms of the Reynolds numbers alone, for both Re_{rheo} and Re_{KD}. The exponents, however, deviate significantly from the expected 1/5. Other studies of Newtonian and shear thinning drop impact have also reported scaling exponents that deviate from 1/5 (cite things). Forensic sciences, for example, traditionally use a $Re^{1/4}$ to study the spreading of blood droplets. Given the small dynamic range in β (less than an order of magnitude), it is unclear if this deviation is significant. In case of the colloidal droplet data we report here, the deviation might also result from the choices we make to compute the effective fluid viscosity. Finally, we have disregarded any effects of shear thinning on the maximum drop spread. Shear thinning must play a role in the spreading dynamics, as the shear rates inside the drop are dynamically changing as the drop spreads.

To summarize, we report how the maximum spreading of colloidal suspension drops, for $0 \leq \phi \leq 0.47$, behaves when the suspensions are treated as Newtonian fluids with an effective viscosity. We compare how the data scales in terms of a number of spreading models present in the literature, and in terms of two choices of calculating the effective viscosity: one using the Krieger-Dougherty effective viscosity model, and the other informed directly from the bulk rheology data we collected. Our data shows a surprisingly good collapse in terms of these models. As we have compared Newtonian fluid models

here, effects of shear thinning are not directly incorporated. We believe that this is the biggest factor contributing to the imperfect data scaling, as opposed to the choice of a specific scaling. Incorporating the effects of surface wettability does not seem to improve the data collapse either. There are many unknowns in the surface wettability correction for Newtonian fluids. In addition, the presence of colloidal particles can be expected to alter substrate interactions. Finally, for both Newtonian fluids, the dynamic range of the experimental data for β is smaller than an order of magnitude, therefore comparing the exact values of the scaling exponents with theoretical predictions may not be meaningful. Nevertheless, the surprisingly good data collapse for our colloidal drop spreading data makes us confident that effective viscosity is one of the key parameters governing drop spreading in the range of Re and We investigated here.

APPENDIX C

SUPPLEMENTARY INFORMATION: COEXISTENCE OF SOLID AND LIQUID PHASES IN SHEAR JAMMED COLLOIDAL DROPS

Note: The contents of this appendix are identical to the Supplementary Information of my publication in Communications Physics: https://doi.org/10.1038/s42005-022-00998-w

C.1 Contact angle of the colloidal suspensions

As the contact angle of our suspensions is very small, it is challenging to measure it via imaging data taken from the side. Therefore, we gently place a 5 µL drop on a hydrophilic glass plate (prepared in a manner identical to the slides used for our experiments), and measure its spreading size. We use the spherical cap approximation to estimate the contact angle from the spreading size. [Inset in Figure C.1] 5 µL drops at $\phi = 0.01$, $\phi = 0.15$, and $\phi = 0.35$ (left to right) are placed on a hydrophilic glass slide. All the drops spread to the same extent (average 9.0 mm), shown quantitatively in the plot [Figure C.1]. Using the spherical cap approximation, we can solve for the drop height h:

$$V_{cap} = \frac{1}{6}\pi(3a^2 + h^2), \tag{C.1}$$

where $V_{cap} = 5$ µL is the volume of the spherical cap, and $a = 4.5$ mm is the radius of the spherical cap.. The contact angle can then be estimated as:

$$\theta = \sin^{-1}\left(\frac{2ah}{a^2 + h^2}\right). \tag{C.2}$$

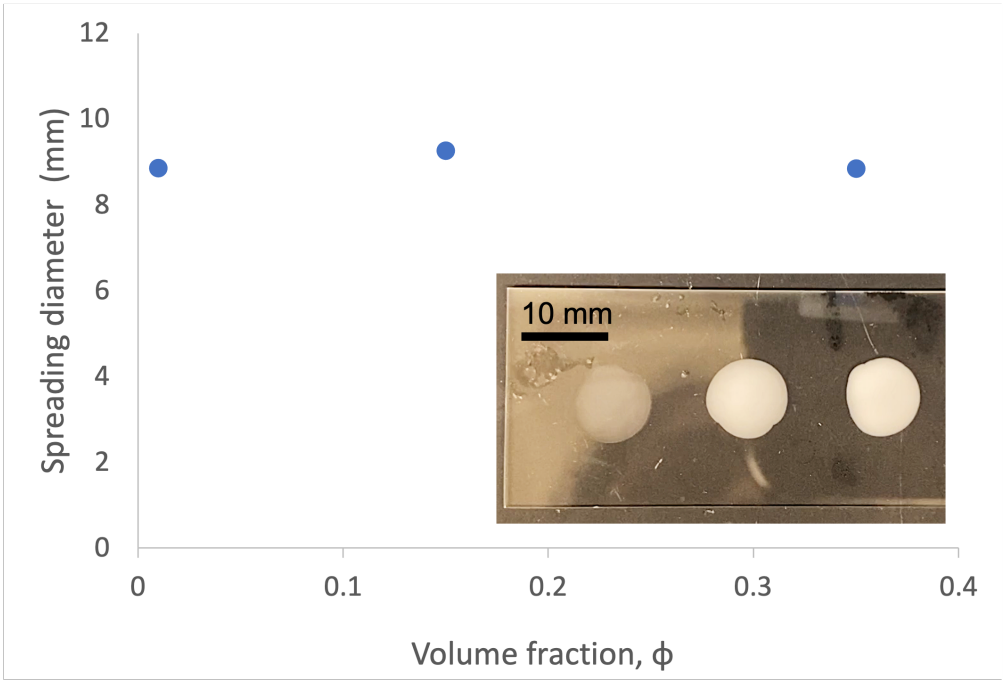

Figure C.1: **Contact angle estimation for colloidal suspensions. Inset:** Gently placed drops of volume 5 µL of silica colloidal suspensions of $\phi = 0.01$, $\phi = 0.15$, and $\phi = 0.35$ respectively, on a hydrophilic glass slide. All three drops spread to the same extent. **Main plot:** The spreading diameter of the colloidal suspensions remains constant with increasing ϕ, and using the spherical cap approximation the contact angle can be estimated as $\theta = 3.8°$.

The above equations give the contact angle of $\theta = 3.8°$. Therefore, the contact angle is constant over ϕ, and it is very low, as expected on hydrophilic substrates.

C.2 Viscosity vs. shear rate for colloidal suspensions

Figure C.2 shows viscosity of our colloidal suspensions plotted against shear rate (the same data is plotted against shear stress in Fig. 1b). We use the viscosity at the highest shear rate as the effective suspension viscosity in the spreading phase.

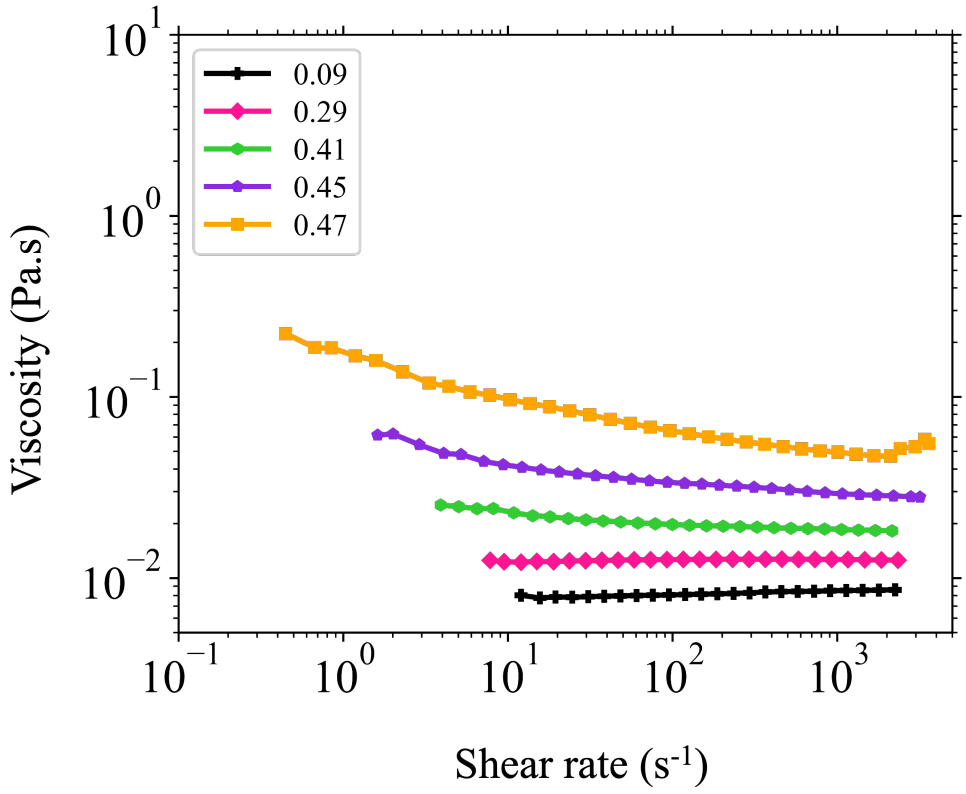

Figure C.2: Rheology data for colloidal suspensions, $\phi \leq 0.47$ (from the same dataset as Fig. 1b), plotted against shear rate.

C.3 Scaling laws for maximum spreading after impact

Scheller et al.[19] reported a $ReWe^{1/2}$ empirical scaling for spreading viscous fluids. Figure C.3a shows this scaling fit to our data (dashed black line). The exponent of our fit (0.165 ± 0.002) shows an impressive agreement with that by Scheller et al. (0.166) More recently, scalings based on models that consider the balance between inertial, viscous, and capillary effects have been reported. Laan et al.[14] considered the relation

$$\beta = Re^{1/5} f(WeRe^{-2/5}) \tag{C.3}$$

and used the first-order Padé approximation to fit experimental data of $\beta/Re^{1/5}$ vs. $WeRe^{-2/5}$:

$$\frac{\beta}{Re^{1/5}} = \frac{(WeRe^{-2/5})^{1/2}}{A + (WeRe^{-2/5})^{1/2}}. \tag{C.4}$$

This equation interpolates between the viscous regime (linear in $WeRe^{-2/5}$) and the inertial regime (constant with $WeRe^{-2/5}$), and consists of a fitting parameter. As discussed by Josserand and Thorodssen [12], the Scheller et al. scaling has the same functional form as Equation C.3, where

$$\beta = (ReWe^{1/2})^{1/6} = Re^{1/5}(WeRe^{-2/5})^{1/12}. \tag{C.5}$$

where $f(WeRe^{-2/5})$ takes the form of a single power law, instead of interpolating between two regimes via a Padé approximant. Thus, although the Scheller et al. model was an empirical fit, it is consistent with the functional dependence of Equation C.3 reported more recently. Figure C.3b shows both the Padé approximation (black dashed line) and a power law fit (red dashed line) to our spreading data of $\beta/Re_{eff}^{1/5}$ vs. $WeRe_{eff}^{-2/5}$. The Padé approximation fit gives $A = 0.09 \pm 0.01$, and the power-law fit gives the exponent of $n = 0.050 \pm 0.02$. This exponent deviates from the value 0.083 (1/12) in order for Equation C.5 to be satisfied. However, we note that the dynamic range of our data is limited, and both curves describe our data well. As discussed by Josserand and Thoroddsen [12] in detail, the number of different scaling models reported in the literature are hard to differentiate. This also holds true for our experimental data of colloidal suspension drops in the spreading regime, as evident from Figure C.3b.

Lee et al.[20] have recently reported a data scaling with a wettability correction, where they calculate the spreading at zero impact velocity, $\beta_{v\to 0}$ using a Padé approximant with

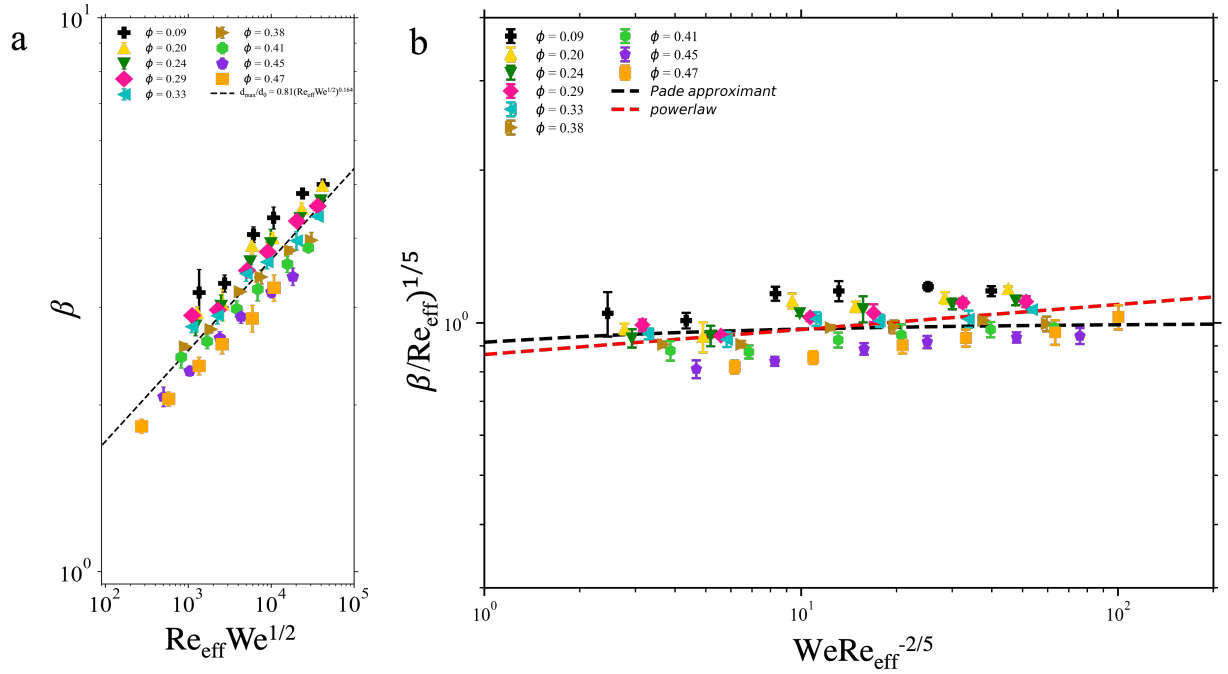

Figure C.3: **Comparison of maximum spread scalings for impacting colloidal drops. a** β vs. $Re_{eff}We^{1/2}$ for spreading colloidal drops. The dashed black line is the power law fit, $\beta = (0.79 \pm 0.02)(Re_{eff}We^{1/2})^{0.165\pm0.002}$. The power law exponent shows a very good agreement with the exponent reported by Scheller et al. for Newtonian fluids. **b** $\beta/Re_{eff}^{1/5}$ vs. $WeRe_{eff}^{-2/5}$ for colloidal suspensions of $\phi \leq 0.47$. The data shows a good collapse. The black dashed line indicates the first-order Padé approximation reported by Laan et al. fit to our data, Equation C.4. The red line indicates a single power law fit. In both panels, error bars indicate one standard deviation over multiple trials.
For the parameter range concerned, both equations describe our data well.

four fitting parameters. Corrected this way, they plot $\sqrt{\beta^2 - \beta_{v\to 0}^2}/Re^{1/5}$ against We, and show good collapse for several fluids. Although correcting for wettability is important while comparing fluids with different surface tensions, in this case the contact angle stays constant over ϕ [Figure C.1]. Therefore, we did not apply these wetting corrections.